UCLA
UCLA Electronic Theses and Dissertations

Title

Design and Analysis of Novel Limb and End-effector Mechanisms for a Highly Capable Quadruped Robot

Permalink

https://escholarship.org/uc/item/61p8p4jd

Author

Rafeedi, Fadi

Publication Date

2024

Peer reviewed|Thesis/dissertation

eScholarship.org Powered by the California Digital Library
University of California

UNIVERSITY OF CALIFORNIA

Los Angeles

Design and Analysis of Novel Limb and End-effector Mechanisms for a Highly Capable Quadruped Robot

A dissertation submitted in partial satisfaction
of the requirements for the degree
Doctor of Philosophy in Mechanical Engineering

by

Fadi Rafeedi

2024

© Copyright by
Fadi Rafeedi
2024

ABSTRACT OF THE DISSERTATION

Design and Analysis of Novel Limb and End-effector Mechanisms for a Highly Capable Quadruped Robot

by

Fadi Rafeedi
Doctor of Philosophy in Mechanical Engineering
University of California, Los Angeles, 2024
Professor Dennis W. Hong, Chair

Quadruped robots are versatile locomotion platforms capable of a variety of manipulation tasks. For each operating environment, the quadruped's choice of kinematic design, actuators, and end-effectors requires tuning and optimization. This research introduces geometrically enhanced designs for limb mechanisms and magnetic variable stiffness end-effectors for a ship-board quadruped platform, SORREL.

The choice of kinematics in quadrupeds is highly dependent on the gait and certain leg designs might be more prone to waste power. Traditional robots, design their kinematics based on the actuator being a single unit consisting of a motor and a gearbox, overlooking the effects of their relative positions on the limb kinematics. A new method was developed for designing the leg kinematics by decoupling the design of the gearbox and the motor. This method gives more freedom in the design of the kinematics and allows for a wider range of configurations best fit for the required task. The quadruped leg design presented in this work has both actuators collocated at the hip in a parallel configuration; however, the gearbox of the knee motor is relocated from the hip to the knee joint. This seemingly simple modification significantly reduces the mechanical antagonism and motor losses and increases the stiffness of the leg.

Quadrupeds perform manipulation and grasping through task-specific actuators. These actuators need to interact with the environment safely while maintaining accurate force control capabilities. More specifically, SORELL needs to be equipped with gripper modules to deal with varying tasks such as typing on keyboards, precision manipulation of electronics, and general pick and place. Most grippers used in manipulators are based on stiff positioned-controlled actuators which provide accuracy but require bulky and expensive Force/Torque (FT) sensors for force control. Additionally, traditional grippers struggle with delicate handling tasks and pose safety risks due to their inherent high stiffness. By employing compliant actuators, namely nonlinear series elastic and variable stiffness actuators, robotic platforms can circumvent such limitations while maintaining the accuracy and stability of the end-effector.

As such, a family of actuators based on magnetic and electromagnetic forces was developed and tested to improve the safety of manipulation and grant accurate force control. The actuators presented use series elastic (SEA) and variable stiffness (VSA) concepts. Two actuators use passive nonlinear springs with constant stiffness profiles based on permanent magnet arrangements. These passive nonlinear SEAs, designed for lightweight and low-cost grippers, can achieve both stiff and soft behavior and have a higher capacity for energy storage than linear springs. With accurate spring modeling, these nonlinear SEAs can change the force control problem into a position control problem avoiding the use of FT sensors. Since passive SEAs use springs with fixed stiffness curves, their stiffness cannot be controlled independently. Moreover, changing the stiffness online is desirable in some grasping tasks that require adjustment in grip strength and compliance. Hence, two actuators that have active stiffness variation (VSA) capabilities through mechanical and electromagnetic means were developed. These actuators, while more complex and costly, give a wider range of stiffness and the ability to tune their stiffness curves. These actuators are studied and categorized

for the intended manipulation tasks encompassing those required on the SORELL platform. Through these designs, multiple unique features were studied and observed such as water-cooled electromagnetic coils, eddy current damping for shock absorption, and the use of negative stiffness for fast explosive motion of gripper fingers.

The dissertation of Fadi Rafeedi is approved.

Jonathan Hopkins

Robert Thomas M'Closkey

Veronica Santos

Dennis W. Hong, Committee Chair

University of California, Los Angeles

2024

To my family and friends.

TABLE OF CONTENT

1 Introduction **1**

1.1 Motivation 1

1.2 Research Objective 2

1.3 Background 3

1.3.1 Quadruped Robots 3

1.3.2 Mechanical Antagonism 12

1.3.3 Actuators 20

1.4 Organization 26

2 Sorell Platform **28**

2.1 Introduction 28

2.2 SORELL and ALPHRED-2 29

2.2.1 ALPHRED-2 Platform 29

2.2.2 SORELL Platform 32

2.2.3 SORELL Body 33

2.2.4 SORELL Leg Design 35

2.3 SORREL Manufacturing 41

2.4 SORELL Attachments 42

3 Sorell Leg **44**

3.1 Introduction 44

3.2 Theoretical Modeling 45

3.2.1 Leg Kinematics 45

3.2.2 Leg Dynamics . . . 51
3.3 Mechanical Antagonism . . . 53
3.4 Gear Train Stiffness . . . 59
3.5 Results . . . 61
3.5.1 Simulation Results . . . 61
3.5.2 Experimental Results . . . 67
3.6 Discussion . . . 70

4 Passive Spring Grippers . . . 71
4.1 Introduction . . . 71
4.1.1 Gripper-Level Compliance . . . 72
4.1.2 Non-linear Springs . . . 72
4.1.3 Grippers with Magnetic Compliance . . . 73
4.2 Passive Magnetic SEAs . . . 74
4.2.1 Stiffness through Magnet Arrangement . . . 75
4.3 MSEA . . . 75
4.3.1 MSEA Design . . . 75
4.3.2 MSEA Modeling . . . 77
4.3.3 Controller . . . 83
4.3.4 Results . . . 85
4.3.5 Applications . . . 89
4.4 PMSEA . . . 90
4.4.1 PMSEA Design . . . 91
4.4.2 PMSEA Spring Modeling . . . 91
4.4.3 PMSEA Gripper Modeling . . . 93

4.5 Discussion 99

5 Active Spring Grippers 100

5.1 Introduction 100

5.2 Coil Induced Variable Stiffness 100

5.2.1 EMVSA 102

5.2.2 EMVSA Design 102

5.2.3 Spring Modeling 103

5.2.4 Results 114

5.2.5 Application 121

5.3 Mechanically Induced Variable Stiffness 121

5.3.1 AMVSA 122

5.3.2 Mechanical Design 123

5.3.3 Simulation 124

5.3.4 Application 127

5.4 Discussion 128

6 Conslusions and Future Work 130

6.1 SORELL Platform 131

6.2 Magnetic SEA and VSA 131

References 134

LIST OF FIGURES

1.1 Quadruped Robot platforms popularized in recent years 4

1.2 Different configurations of a two DoF planar manipulator 4

1.3 General two Dof leg diagram 7

1.4 Traditional quadruped robot leg configurations 8

1.5 Coupled movement between hip and knee in the parallel case . . . 11

1.6 SLIP Model for a robotic leg 16

1.7 SLIP Model including an added DoF in leg length direction 18

1.8 Quadruped Robot platforms popularized in recent years 20

1.9 Different robotic actuator diagrams 21

1.10 Different VSA mechanism design diagrams 25

2.1 ALPHRED-2 as presented in [1] 29

2.2 ALPHRED-2 Configurations: 2.2a Symmetric stable mode, 2.2b Tripod single manipulation mode, 2.2c Dynamic mode, 2.2d Caster wheeled mode, 2.2e Jumping/ pronking mode, 2.2f Biped dual manipulation mode [1] 30

2.3 Early design adaptation of SORELL standing up 33

2.4 Modes of operation for early adaptation of SORREL 34

2.5 Modes of operation for SORREL 35

2.6 External and internal body structures 36

2.7 Top view of SORELL 37

2.8 SORELL leg 38

2.9 SORELL hip joint assembly 39

2.10 SORELL femur assembly 40
2.11 SORELL knee assembly 41
2.12 SORELL tibia assembly 42
2.13 Manufactured knee gearbox 42
2.14 Manufactured femur link with Knee joint gear box 43
2.15 Manufactured and assembled SORELL 43

3.1 The three different configurations considered for this analysis . . . 45
3.2 Two-DoF leg represented as a SLIP 56
3.3 The two gear-trains configurations considered for this study . . . 59
3.4 stiffness ratio between the motor-belt-gear and motor-gear-belt configurations 60
3.5 Static hip motor torque comparison 61
3.6 static knee motor torque comparison 62
3.7 Advantage of relocating the knee motor to the knee joint 63
3.8 Foot location and associated hip torque for each case 64
3.9 Static Hip and Knee motors torque for three cases needed to support robot weight 65
3.10 Actuator torque/ velocity direction in stance phase 66
3.11 Dynamic Torques during walking gait 67
3.12 Leg powers Power in the three systems analyzed 68
3.13 Experimental Setup for Knee GB experiment 69
3.14 Static hip and knee motors torque for three cases considered over gait 70

4.1 Gripper family tree 74

4.2 MSEA nonlinear rotary magnetic spring design © 2021 IEEE . . 77
4.3 Virtual springs formed by input and output arrays of magnets © 2021 IEEE 78
4.4 Parallel Vs. angled configuration 79
4.5 Parallel vs. angled configuration force simulation © 2021 IEEE . 80
4.6 MSEA magnetic spring design © 2021 IEEE 80
4.7 A single pair of MSEA magnets in EMS 81
4.8 MSEA theoretical vs. simulated vs. experimental torque profile © 2021 IEEE 82
4.9 MSEA stiffness profile as a function of angular separation © 2021 IEEE 83
4.10 Gain-scheduled force controller © 2021 IEEE 86
4.11 MSEA high impedance test setting © 2021 IEEE 86
4.12 MSEA sinusoidal (top) and step response (bottom) force tracking 87
4.13 Bandwidth of MSEA 87
4.14 MSEA impact test set-up © 2021 IEEE 88
4.15 MSEA free response and impact response tests 89
4.16 Prototype of MSEA underactuated gripper © 2021 IEEE 90
4.17 PMSEA magnetic spring diagram 92
4.18 PMSEA magnetic spring 92
4.19 PMSEA: theoretical vs. simulated vs. experimental torque profile 93
4.20 Stiffness profile of PMSEA 94
4.21 PMSEA gripper prototype design 95
4.22 Mechanism manifold with projected stiffness profiles for different finger equilibrium positions 98

5.1 EMVSA with Gripper Hand 101
5.2 Cross-section CAD model of EMVSA spring 103
5.3 EMVSA coil and cooling chamber 104
5.4 EMVSA coil and permanent magnet Arrangement 106
5.5 Active magnet and stationary magnet Pair 108
5.6 Simulation sample results for EMVSA spring in EMS for maximum PM_A deflection 110
5.7 EMVSA high impedance test setup 110
5.8 EMVSA Experimental Model Results 111
5.9 3D surface for curve fit of the force-displacement-current 112
5.10 EMVSA Diagram 113
5.11 EMVSA Block Diagram 113
5.12 EMS simulation of EMVSA core tempreture 115
5.13 Step and sine response of EMVSA force tracking for a 10N amplitude by spring positioning 116
5.14 Sample current values through the coil for sine tracking experiment 116
5.15 Step and sine response of EMVSA current tracking 117
5.16 EMVSA force tracking bandwidth for zero current 118
5.17 EMVSA free response plots 119
5.18 EMVSA eddy current simulation in EMS. 119
5.19 Exploiting instability region for fast explosive motion 120
5.20 EMVSA Gripper 121
5.21 Antagonistic configuration on a single finger gripper 123
5.22 Schematic of proposed antagonistic magnetic VSA 124

5.23 AMVSA CAD model 125
5.24 AMVSA assembled prototype 126
5.25 Single spring force-displacement curves 127
5.26 AMVSA three-finger under-actuated hand 128
5.27 A single motor connected to three driving magnets through bevel gears 129
6.1 132
6.2 133

LIST OF TABLES

2.1 Joint ranges for SORELL vs ALPHRED-2 34

2.2 Actuator properties used on SORELL 39

4.1 Assembly magnetic spring characteristics © 2021 IEEE 76

4.2 Single magnet parameters © 2021 IEEE 76

4.3 MSEA polynomial coefficients © 2021 IEEE 83

4.4 PMSEA polynomial coefficients 94

4.5 PMSEA gripper parameters 96

5.1 Magnetic spring parameters 105

ACKNOWLEDGMENTS

First and foremost, I would like to express my deepest gratitude to my advisor, Dr. Dennis Hong, for his support and encouragement throughout my years at RoMeLa, UCLA. His enthusiasm and expertise in the field of robotics have been instrumental to the completion of this work. I am especially grateful to him for providing me with the creative space and resources to complete my work.

I would like to also thank my committee, Dr. Robert M'Closkey, Dr. Jonathan Hopkins, and Dr. Veronica Santos for their valuable guidance and feedback on this work. I have learned a lot from being a student in their classes as well as working closely with them at UCLA.

I am also very grateful for the support of my immediate and extended family. My mother Samia and father Azeez, instilled in me the passion to pursue knowledge and supported me in my lifelong dream to become a scientist. Their endless sacrifices throughout my life in Palestine have been the cornerstone of my success.

To my wife, Maha, for her love, and support throughout this journey. Her patience during the most stressful times has been instrumental to the completion of this work. And to my brother Tarek, for his direct help in critiquing and editing this dissertation and for his valuable scientific knowledge that always challenged my work. I would also like to acknowledge my cousins and extended family for their continued support, especially my uncles Kamil and Majed and my Aunts, Abeer and Maha.

Finally to my friends and colleagues at RoMeLa for the great knowledge, and mentorship that I received from them and the for great and fun memories at the lab. I would like to especially thank Jeong H. Yoon, Donghun Noh, Cameron Zamora, and Salim Essaid for their direct contribution to this research.

CURRICULUM VITAE

2014-2017	B.S. in Mechanical and Aerospace Engineering Department, University of California, Los Angeles (UCLA).
2017-2018	M.S. in Mechanical Engineering and Aerospace Department, University of California, Los Angeles (UCLA).
2018-2024	Ph.D. candidate in Mechanical and Aerospace Engineering Department, University of California, Los Angeles (UCLA).

PUBLICATIONS

F. A. Rafeedi, J. H. Yoon and D. Hong, 2021, Oct. Design and Control of a Novel Compact Nonlinear Rotary Magnetic SEA (MSEA) for Practical Robotic Gripper Implementation. In *IEEE Robotics and Automation Letters, vol. 6, no. 4, pp. 7643-7650, Oct. 2021,*

B. G. Zastrow et al., 2021, November. Investigation of electrical chatter in bifurcated contact receptacles. In *2021 IEEE 66th Holm Conference on Electrical Contacts (HLM), San Antonio, TX, USA, 2021, pp. 16-23*

D. Noh et al., 2020. Minimal Degree of Freedom Dual-Arm Manipulation Platform with Coupling Body Joint for Diverse Cooking Tasks. In *2020 17th International Conference on Ubiquitous Robots (UR), Kyoto, Japan, 2020*, pp. 225-232

CHAPTER 1

Introduction

1.1 Motivation

Robotic platforms have long seen incredible success in different areas such as manufacturing and assembly lines. The reliance on robots and robotic manipulators is evident in many industries. Despite these advances in factory and lab-controlled settings, robotic platforms have had a large burden to overcome to migrate from these controlled environments to broader applications. For instance, for assembly-line robots precise manipulation is a necessity to ensure the repeatability of certain tasks. However, once the robot is set to interact in an alternate or foreign environment, many challenges arise due to the variability and uncertainty of that environment. These challenges are especially prevalent in legged robots such as quadrupeds and bipedal robots. For a legged robot to work in such environments it should be able to manage various impacts as well as interact with objects with various mechanical properties. Hence, creating robotic mechanisms and designs that adapt to these complexities is a step in achieving overall robotic versatility.

Legged robots are developed to mimic the form and function of biological beings. The limbs lend them the ability to interact with human-oriented environments where other mechanisms, such as wheels, are not ideal. Such an ability, demonstrated by bipedal platforms, for instance, has gained them an increased interest in the field. The bipedal nature of these robots makes them highly versatile by allocating upper limbs for task manipulation and reserving the lower limbs for locomotion. However, due to their geometric complexity and weight distribution, they demand intricate control strategies.

Quadruped robotic platforms, on the other hand, offer higher intrinsic stability with versatility in both human-designed and foreign environments. Examples of these platforms include SPOT, ALPHRED, and Cheetah [2] [1] [3]. Most of these platforms focus on the locomotion part of the robot leveraging the inherent static stability of quadruped robots. Despite this success, few of these platforms were designed to be effective in locomotion and manipulation tasks alike. Even for the few quadrupeds that can perform manipulation tasks, they use basic grippers for pick and place operations and these grippers are not optimized for the tasks they are performing.

1.2 Research Objective

The objective of this research focuses on the development of mechanisms that will enable a quadruped robot to perform locomotion tasks with high mechanical efficiency as well as interact safely during manipulation tasks. To that effect, this work presents a deep study of robot leg mechanisms and designs coupled with actuators that achieve desirable and safe manipulation.

This research leverages the successes in quadruped robotic platforms, especially ALPHRED-2, to design a new generation quadruped SORELL. As part of the design process for SORELL, this work investigates methods to optimize the form and weight of the robot. It also delves deep into the possible choices of the kinematic configuration of the articulated legs and its role in minimizing power consumption when the robot is standing and during examined gaits. Subsequently, a new kinematic leg configuration design is introduced and studied theoretically, experimentally, and through simulation.

In tandem, this work also evaluates the use of nonlinear magnetic series and variable stiffness actuators for manipulation tasks done on quadruped robots. It introduces a library of compliant actuators that utilize magnetic forces. This

family of grippers examines and implements unique mechanisms and geometries to generate standalone grippers and actuators. This library is envisioned to be both an independent platform for further development and a versatile toolkit for SORELL's future applications.

1.3 Background

1.3.1 Quadruped Robots

Many quadruped robotic platforms have surfaced in recent years owing to their versatility and inherent stability [4] [5] [2] [1] [3] [6]. These "four-legged" robots utilize different kinds of actuators as well as different leg kinematic modes depending on their intended tasks. Some of these quadrupeds, like Cheetah, Spot, and ANYmal [5] [2] [3], use the traditional biomimetic leg kinematics with the abduction/adduction degree of freedom (DoF) achieved through a hip-roll joint. In this configuration, the quadruped closely resembles biological quadrupeds (e.g. Spot and ANYmal). On the other hand, some quadrupeds, most notably ALPHRED and ALPHRED-2 [1] [7], swap the abduction/adduction DoF with a hip yaw joint, sacrificing some of the dynamic benefits for a larger workspace on the leg. Hence, robots such as ALPHRED, can exploit the expanded motion envelope of the leg to perform simple manipulation tasks with one limb while maintaining a statically stable pose in the tripod configuration. The joint DoF's that follow the first hip joint, are similar across most platforms and they consist of two or three pitch joints.

As quadrupeds vary by kinematic design, they also use different actuators to achieve their dynamic motion. Early concept quadrupeds usually use traditional servomotors with a high gear ratio making them ideal for position control. Even though these actuators have high position control accuracy they have poor impact mitigation and force control. Some quadrupeds, including ANYmal, use

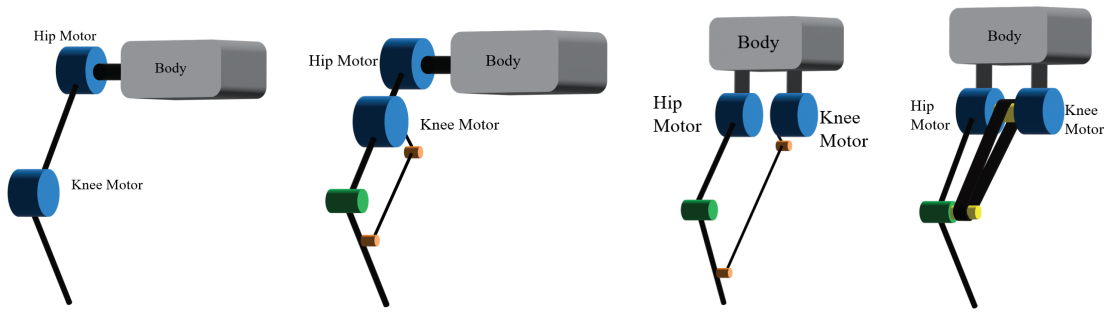


(a) Cheetah [3] (b) Spot [2] (c) ANYmal [5]

Figure 1.1: Quadruped Robot platforms popularized in recent years

series elastic actuators (SEA) which use a high gear ratio motor in series with a spring. SEAs increase the impact mitigation and enable the joint to store energy that is recycled at a later phase of the gait. SEAs, however, reduce the bandwidth of the actuator and require extensive optimization for the choice of spring stiffness. Other quadruped robots such as MIT Cheetah and ALPHRED-2 use proprioceptive quasi-direct drive actuators [6]. These actuators sacrifice some of the force control accuracy for higher bandwidth and proprioception achieved by directly driving a brushless DC motor. BigDog [8] and HYQ2Max [9] on the other hand use hydraulic actuators that have high power density and force output; however, these actuators suffer from fluid leaks and increased complexity.

1.3.1.1 Quadruped Leg configurations



(a) Serial (b) Collocated serial with linkage (c) Parallel linkage (d) Parallel belt

Figure 1.2: Different configurations of a two DoF planar manipulator

The kinematics of a robotic manipulator, or how the motion on the actuator space translates to motion in the operational space, varies between platforms. The choice of leg kinematic configurations depends on the potential use cases and target terrains. Many leg designs try to reduce the flung mass of the leg by placing all or most actuators of the leg on the hip closer to the body [10] [11]. In that case, the hip pitch and knee pitch actuators are either in a serial configuration, where the hip joint drives the knee motor and the linkages, or through a parallel configuration, where both actuators act on the hip joint and the knee through either a linkage [12] or a belt [1]. The parallel configuration reduces the flung mass and restricts the motion of the actuator chassis with respect to the body. Reducing the flung mass, and hence the inertia of the driven limb makes the control of the limbs smoother and enables the limb faster acceleration and deceleration. Other robots have a joint actuator on each respective joint (knee and hip) such as in the case of ANYmal. The configuration on ANYmal removes any coupling between the actuators and simplifies the control of the leg. Each of these designs gives unique advantages and disadvantages based on the position and gait of the robot.

Shown in Fig. 1.8 are commonly used variations of the serial and parallel driving paradigms for the last two DoF's in a robotic leg. The serial configuration, Fig.1.2a places the actuator at its corresponding joint. In this case, the hip actuator has to drive the linkage connecting the knee and hip. While the mechanism decouples the motion and torques of both actuators, it increases the flung mass of the leg since the hip actuator will have to drive the knee motor's inertia, which in this case increases with the inter-joint distance. Another potential disadvantage of this mechanism is that the large or bulky knee actuator may interfere with the reach, carrying capacity, or pose of the whole limb. An alternative to the serial configuration is the collocated serial shown in Fig. 1.2b, where the hip motor is still driving the chassis of the knee motor, but the knee motor is placed closer to

the hip. This placement reduces the moment of inertia hence limiting the flung mass. The knee motor drives the knee joint through a linkage that crosses the hip and the knee. In both of the described cases, the chassis of the knee motor is to rotate with the hip joint which can cause some difficulty with electrical interfacing as well as the range of the hip joint. The collocated serial mechanism was used in ARTEMIS humanoid robot [13].

In the second set of configurations, shown in Fig. 1.2d and Fig. 1.2c, the actuators are collocated at the hip and both knee and the hip motors are fixed with respect to the robot body. In both cases, one of the motors is connected to the knee joint through a biarticular mechanism, that acts on more than one joint. These examples consider two kinds of biarticular joints, one through a linkage and another through a belt. In the case of a linkage, the mechanism offers a rigid connection but can suffer from buckling due to repeated impacts at the foot. The linkage also does not allow a 360° rotation of the knee joint due to linkage collision and singularity. In the case where manipulation is done through one of the legs, a linkage can limit the range of motion of the end-effector. The belt in the parallel case, on the other hand, allows for a 360° rotation. Although the belt itself, being less rigid than the knee motor gear, will present potential errors when measuring the true position of the knee, it offers better shock absorption capability. Besides these effects, a noteworthy feature of the parallel configuration is the coupled kinematics between the knee and hip joints. Meaning that a displacement or a torque on either motor could affect both the knee and the hip joints.

1.3.1.2 Leg Kinematics and Dynamics

When considering two DoF legs with two identical actuators, the kinematics, and dynamics depend on the geometry of the mechanism and the location of the actuators as derived by multiple previous works i.e. [14] [15] [16]. In Fig. 1.8 the kinematics of both parallel cases are identical and the kinematics of both serial

cases are identical as well.

In the case of a generalized two DoF leg shown in Fig. 1.3 the torques and angles of the joints do not depend on the kinematic configuration. The torques of joints 1 and 2 (τ_{j1} and τ_{j2}) in the static case solely depend on the torques needed to hold the joints (counter the torque due to a force at the foot in this case f). On the other hand, the angles of joints 1 and 2 (q_{j1} and q_{j2}) depend on the foot placement with respect to the body which is noted as P_x and P_y. Hence the torques and angles of the joints, i.e. the joint space, are said to be configuration-independent.

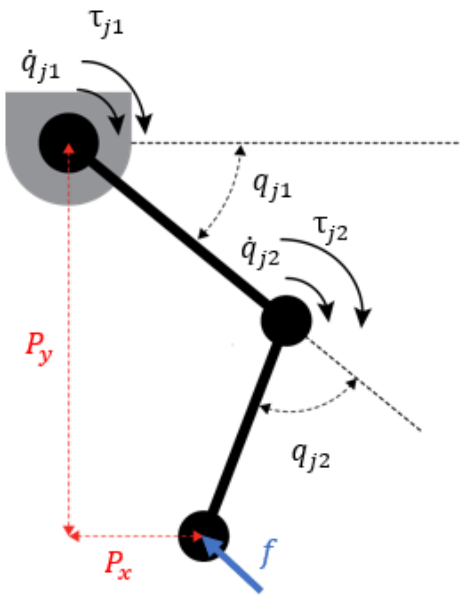
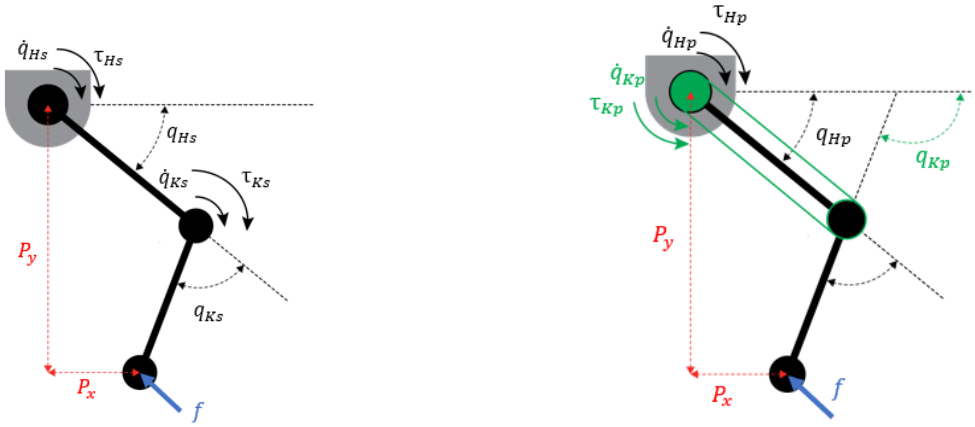


Figure 1.3: General two Dof leg diagram

Given the fact that the joint space is configuration-independent, it would then depend on the placement of the actuators to satisfy the joint angle and torque requirements for a certain pose. In other words, the actuator space depends on the chosen configuration. To characterize the relationship between the joint and actuator space we need to take a closer look at the two configurations shown in Fig. 1.4.

Fig. 1.4 shows the two configurations that appear in most quadruped robot



(a) Serial (b) Parralel

Figure 1.4: Traditional quadruped robot leg configurations

legs. As compared to the different configurations presented in Fig. 1.8, the two serial configurations were grouped and the same was done for the two parallel cases. This is because the two serial configurations and the two parallel configurations have identical kinematics.

Fig. 1.4 shows the simplified models of a serial (Fig. 1.4a) and a parallel (Fig. 1.4b). In the serial case, the actuators are placed at the joints, while in the parallel case, they are both placed at the hip. In the parallel case, the knee motor then acts through the femur linkage on the knee joint with a 1:1 gearing ratio pulley system.

Using $L1$ and $L2$ as the lengths of the femur and tibia respectively, the 2D kinematics can be written as:

$$P_x = L_1 cos(q_{Hs}) + L_2 cos(q_{Hs} + q_{Ks}) \tag{1.1}$$

$$P_y = -L_1 sin(q_{Hs}) - L_2 sin(q_{Hs} + q_{Ks}) \tag{1.2}$$

Where q_{Hs} and q_{Ks} are the actuator angles in the serial configuration for the Hip and knee actuators respectively. Partial differentiation gives the following for a serial configuration.

$$\begin{bmatrix} \dot{P}_x \\ \dot{P}_y \end{bmatrix} = \begin{bmatrix} -L_1 sin(q_{Hs}) - L_2 sin(q_{Hs} + q_{Ks}) & -L_2 sin(q_{Hs} + q_{Ks}) \\ -L_1 cos(q_{Hs}) - L_2 cos(q_{Hs} + q_{Ks}) & -L_2 cos(q_{Hs} + q_{Ks}) \end{bmatrix} \begin{bmatrix} \dot{q_{H_s}} \\ \dot{q_{K_s}} \end{bmatrix} \tag{1.3}$$

For the parallel mechanism case, the location of the foot with respect to the body can be written as follows.

$$P_x = L_1 cos(q_{Hp}) + L_2 cos(q_{Kp}) \tag{1.4}$$

$$P_y = -L_1 sin(q_{Hp}) - L_2 sin(q_{Kp}) \tag{1.5}$$

In this case, the angles of the actuators are q_{Hp} and q_{Kp} for the hip and knee motors respectively. Where q_{Kp} is the biarticular angle as presented in [14]. Taking the partial derivative of Eq. 3.7 and Eq. 3.5 yields the following.

$$\begin{bmatrix} \dot{P}_x \\ \dot{P}_y \end{bmatrix} = \begin{bmatrix} -L_1 sin(q_{Hp}) & -L_2 sin(q_{Kp}) \\ -L_1 cos(q_{Hp}) & -L_2 cos(q_{Kp}) \end{bmatrix} \begin{bmatrix} \dot{q_{H_p}} \\ \dot{q_{K_p}} \end{bmatrix} \tag{1.6}$$

The jacobian of both configurations from Eq. 3.6 and 3.9 can then be written as.

$$J_s = \begin{bmatrix} -L_1 sin(q_{Hs}) - L_2 sin(q_{Hs} + q_{Ks}) & -L_2 sin(q_{Hs} + q_{Ks}) \\ -L_1 cos(q_{Hs}) - L_2 cos(q_{Hs} + q_{Ks}) & -L_2 cos(q_{Hs} + q_{Ks}) \end{bmatrix} \tag{1.7}$$

$$J_p = \begin{bmatrix} -L_1 sin(q_{Hp}) & -L_2 sin(q_{Kp}) \\ -L_1 cos(q_{Hp}) & -L_2 cos(q_{Kp}) \end{bmatrix} \tag{1.8}$$

The main difference between the two configurations is how the torque and angles of the motors affect the absolute angles of the joints. Here we present the configuration matrix that relates the actuator space to the joint space for each of the serial and parallel cases.

$$\begin{bmatrix} \tau_{j1} \\ \tau_{j2} \end{bmatrix} = \begin{bmatrix} 1 & 0 \\ 0 & 1 \end{bmatrix} J_s^T \begin{bmatrix} f_x \\ f_y \end{bmatrix} = \underbrace{\begin{bmatrix} 1 & 0 \\ 0 & 1 \end{bmatrix}}_{\text{Config. Matrix } G_s} \begin{bmatrix} \tau_{Hs} \\ \tau_{Ks} \end{bmatrix} \tag{1.9}$$

$$\begin{bmatrix} q_{j1} \\ q_{j2} \end{bmatrix} = \begin{bmatrix} 1 & 0 \\ 0 & 1 \end{bmatrix} J_s^{-1} \begin{bmatrix} P_x \\ P_y \end{bmatrix} = \underbrace{\begin{bmatrix} 1 & 0 \\ 0 & 1 \end{bmatrix}}_{\text{Config. Matrix } G_s^{-T}} \begin{bmatrix} q_{Hs} \\ q_{Ks} \end{bmatrix} \tag{1.10}$$

For the parallel case

$$\begin{bmatrix} \tau_{j1} \\ \tau_{j2} \end{bmatrix} = \begin{bmatrix} 1 & 1 \\ 0 & 1 \end{bmatrix} J_p^T \begin{bmatrix} f_x \\ f_y \end{bmatrix} = \underbrace{\begin{bmatrix} 1 & 1 \\ 0 & 1 \end{bmatrix}}_{\text{Config. Matrix } G_P} \begin{bmatrix} \tau_{Hp} \\ \tau_{Kp} \end{bmatrix} \tag{1.11}$$

$$\begin{bmatrix} q_{j1} \\ q_{j2} \end{bmatrix} = \begin{bmatrix} 1 & 0 \\ -1 & 1 \end{bmatrix} J_p^{-1} \begin{bmatrix} P_x \\ P_y \end{bmatrix} = \underbrace{\begin{bmatrix} 1 & 0 \\ -1 & 1 \end{bmatrix}}_{\text{Config. Matrix } G_P^{-T}} \begin{bmatrix} q_{Hp} \\ q_{Kp} \end{bmatrix} \tag{1.12}$$

Equations 1.9 and 1.11 show how the torques of the actuators contribute to the torques at the joints. While equations 1.10 and 1.12 reflect the relationship between the angles of the actuators and their respective joints.

In the serial case, the joint torque and the actuator torque are equivalent, that is due to the fact that there is no coupling between the actuators. However, in the parallel configuration case, the torques of the actuators add up at the joint meaning that to satisfy a hip joint torque of τ_{j1} both torques of the hip and knee actuators need to add up to that value. As for the joint angles, the angle of the knee joint is the sum of the negative angle of the hip motor added to the positive angle of the knee motor. This is a clear case of coupled motion between the two actuators. For instance, if the knee motor is fixed and the hip motor is moving, then the knee joint will move with the same angle value but in the opposite direction.

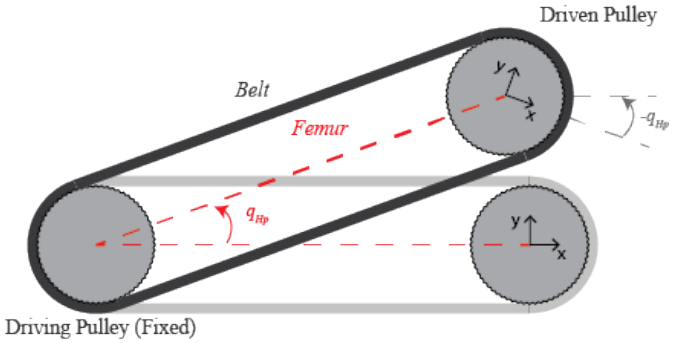


Figure 1.5: Coupled movement between hip and knee in the parallel case

To get a better idea of why that happens Fig. 1.5 shows the coupling between the hip joint motion and the knee joint motion. The red line shows the femur

link which connects the two axis of rotation for the pulleys. In the case when the driving pulley is fixed, the driven pulley can rotate only with the axis connecting the two pulleys. In the case the femur rotates, the driven pulley will rotate in the opposite direction. The rate of rotation would depend on the gearing ratio between the two pulleys. If the driven pulley has a different size, then the rate of change will be multiplied by the gearing ratio between the two. This relationship is shown mathematically in Eq. 1.12.

1.3.2 Mechanical Antagonism

The design of a robotic limb has many constraints, but one of the most important ones is the power aspects of the mechanism. It is very crucial to consider the power requirements of tasks associated with the gait. Preferred designs have lower power consumption over the span of tasks and configurations. Robotic designs tend to focus on lowering the TCoT (Total Cost of Transport) as well as the MCoT (Mechanical Cost of Transport). It is also important to consider, when designing robotic legs, the distribution of work across actuators. Meaning that all actuators share a similar contribution to the total power delivered to a task. This will avoid a small number of actuators doing most of the work which could result in these actuators operating near their limit in inefficient conditions. Another aspect to be avoided is geometric work and antagonistic power which will be discussed in length in the next section.

1.3.2.1 Geometric Work in Legged Robots

Mechanical antagonism in legged robotics arises in cases where the power delivered to the environment is not necessarily the power generated by the actuators. Certain mechanisms are more prone to this effect under certain circumstances. For example, two actuators acting on the same link one with positive power and

the other with negative power will cause some of the power to cancel out limiting the amount of torque transmitted to the task [17]. This observed effect gave rise to the study of geometric work.

The idea of geometric work has been known in manipulators and robotic legs since the introduction of multi-actuator robotic systems. The idea of geometric work can be synonymous with the idea of fighting internal forces where if multiple forces are acting on the same body, opposite forces cancel [18]. The geometric work can be defined as the energy lost due to an internal power loop when two or more actuators are included. Geometric work arises when at least one actuator is doing positive work while the other is doing negative work. This effect can be amplified by the kinematics of the robotic leg over the specified gait [16].

In earlier robotic designs, roboticists were trying to minimize the negative work in a system that would result from back-driving actuators. In the case of back-driving actuators, the actuator is outputting negative power or in other words absorbing power. If such energy is not recaptured or regenerated then it is lost. Hence, earlier designs treated all negative powers as undesirable. Multiple researchers tried to minimize this negative work through physical designs such as the pantograph design presented in [19] or through path planning [20].

In later iterations of robotic legs, it became apparent that certain tasks require the total power to be negative such as walking downhill [16]. Such cases would require the power output of a leg to be negative. Song and LEE defined geometric work as the difference between input and output energies to a system as referred to in Eq. 1.13. This definition takes into account that the mechanical power delivered by the leg can be negative. In that case, positive powers will be undesirable.

$$W_g = \sum_{i=1}^{p} |E_i| - |E_m| \tag{1.13}$$

Where E_m is the total output mechanical power of the leg and can be written as,

$$E_m = |\sum_{i=1}^{p} E_i| \tag{1.14}$$

Hence the difference between the sum of the absolute value and the absolute value of the sum of the actuator energies is the geometric work. Similarly [17] defines the geometric work in the construct of actuator powers. Where the antagonistic power is the P_{ant} is defined as the difference between the net power P_{net} and the total power P_{tot}. Here the antagonistic power is defined as the difference between the total power used by the actuators and the net power delivered to the task. The net power definition is coordinate invariant, meaning it does not depend on the kinematics of the system. However, the total power is the sum of the powers flowing through the actuators. For this study, we have slightly changed the notation to reflect this, as the net power reflects the dot product of the torque and velocity vectors in the joint space, while the total power is the sum of the absolute values of the individual actuator powers as shown in Eq 1.15 and 1.16.

$$P_{net} = \sum_{i=1}^{p} P_{joint,i} = \tau_j.\dot{\theta}_j \tag{1.15}$$

$$P_{total} = \sum_{i=1}^{p} |P_{motor,i}| = \sum_{i=1}^{p} |\tau_{M,i}\dot{\theta}_{M,i}| \tag{1.16}$$

$$P_{ant} = \frac{1}{2}(\sum_{i=1}^{p} P_{motor,i} - |\sum_{i=1}^{p} P_{joint,i}|) \tag{1.17}$$

The earlier definition of geometric work results in stronger penalties on negative powers, hence [16] reformulated the geometric work formula to set negative

works to zero.

$$W_g = \sum_{i=1}^{p} \bar{E}_i - |E_m| \tag{1.18}$$

Where $\bar{E}_i$ takes the following values

$$\bar{E}_i = \begin{cases} E_i & E_i \geq 0 \\ 0 & E_i < 0 \end{cases} \tag{1.19}$$

1.3.2.2 SLIP Model for Design of Robotic Legs

The spring-loaded inverted pendulum (SLIP) [21] is a very popular model to describe the modes of locomotion for legged robots including running and walking. Even though the SLIP model might not capture all the dynamics of a leg; it does capture the essential ones. Hence the SLIP is very popular for modeling robotic legs [22] [23] [24] [25]. In the case of designing robotic legs, [16] has used the SLIP model as a template to design robotic legs that best match the dynamics of the SLIP model.

The method that [16] introduced starts by considering the SLIP model, shown in 1.7 which is an energy-conservative model. The SLIP model has one original degree of freedom which is the angle that it makes with the ground ϕ and no actuators but rather energy recycled from the spring cycle. The template-based method is then concerned with adding degrees of freedom to the original model as well as an actuator. The design process determines based on the concept of minimizing geometric work, where to place these actuators.

Note that for the design considered in this thesis, physical springs are not

used for energy storage and recycling. However, the SLIP model is still valid if the virtual impedance is rendered to reflect spring-mass dynamics in a high transparency actuator [26].

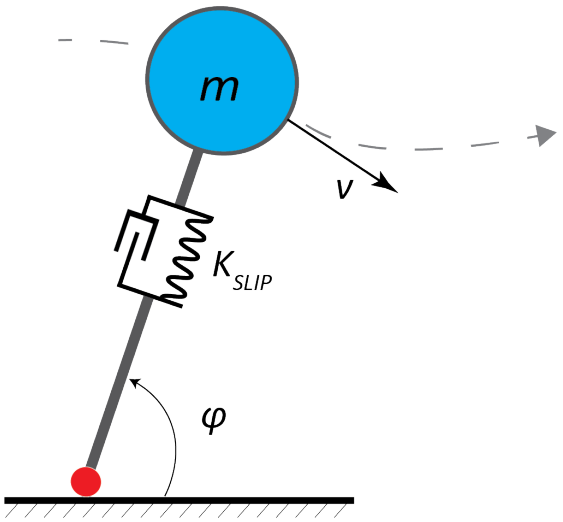


Figure 1.6: SLIP Model for a robotic leg

The formulation of the theorem divides the actuated space of a mechanism into two parts, the first is the original degrees of freedom of the SLIP model, ϕ, and the rest are added degrees of freedom denoted as released constraints. The relationship between the joint space, denoted as θ, and the actuated space, q, can be written as follows.

$$\begin{bmatrix} \theta_1 \\ \theta_2 \end{bmatrix} = \underbrace{\begin{bmatrix} a_1 & a_2 \\ a_3 & a_4 \end{bmatrix}}_{\text{A}} \begin{bmatrix} q_r \\ q_b \end{bmatrix} \tag{1.20}$$

Even though this methodology was proposed for any leg mechanism with any number of DoF, this study will limit the discussion to two DoF systems that are relevant to robot legs similar to ones on ALPHRED-2 for simplicity. Hence, the Jacobian matrix A is a 2×2 full rank matrix. This relationship is extended to the generalized forces and torques shown in Eq. 1.21, where the generalized forces

are denoted by Q and the actuator torques and forces as τ

$$\begin{bmatrix} \tau_1 \\ \tau_2 \end{bmatrix} = \underbrace{\begin{bmatrix} b_1 & b_2 \\ b_3 & b_4 \end{bmatrix}}_{\mathrm{B}} \begin{bmatrix} Q_r \\ Q_b \end{bmatrix} \tag{1.21}$$

It is worth noting that the A and B matrices are both full-rank matrices and satisfy the following relationship for any kinematic configuration.

$$B = A^{-T} \tag{1.22}$$

This study considers two DoF legs and will follow the process shown in [16], by adding an extra released constraint in the direction of leg length. So the total degrees of freedom include the angle the leg makes with the ground ϕ and the leg length denoted as l_m. Two actuators are then added to the model one acting in the length length direction and another acting in the leg angle direction. These generalized forces can be shown as Q_l and Q_ϕ respectively.

Now using these DoF and actuator forces, Eq. 1.20 can be rewritten as.

$$\begin{bmatrix} \theta_1 \\ \theta_2 \end{bmatrix} = \underbrace{\begin{bmatrix} a_{11} & a_{12} \\ a_{21} & a_{22} \end{bmatrix}}_{\mathrm{A}} \begin{bmatrix} \dot{l}_m \\ \dot{\phi} \end{bmatrix} \tag{1.23}$$

The power in the joint space, which can be obtained by a dot multiplication between the joint forces and the joint angles can be written in terms of the generalized forces and angles as follows.

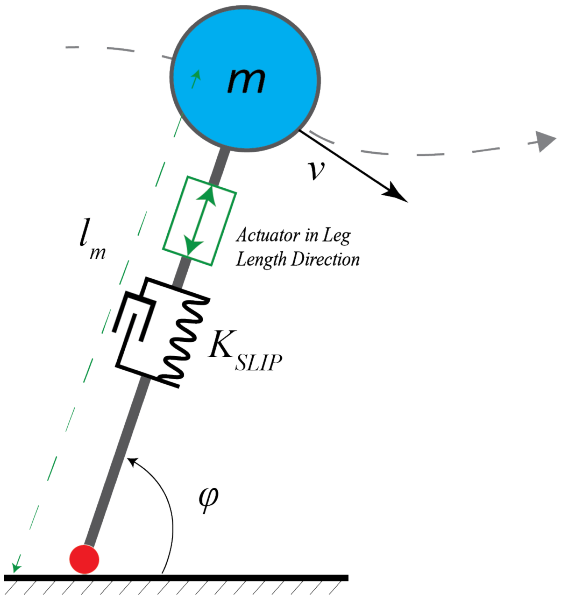


Figure 1.7: SLIP Model including an added DoF in leg length direction

$$P_1 = \frac{a_{11}\dot{l}_m + a_{12}\dot{\phi}}{a_{11}a_{22} - a_{21}a_{21}}(a_{22}Q_l - a_{21}Q_\phi) \tag{1.24}$$

$$P_2 = \frac{a_{21}\dot{l}_m + a_{22}\dot{\phi}}{a_{11}a_{22} - a_{21}a_{21}}(-a_{12}Q_l + a_{11}Q_\phi) \tag{1.25}$$

It is then formulated for the ideal operation of the mechanism and for it to match the dynamics of the SLIP mode.

$$\dot{l}_m = 0 \qquad\qquad Q_\phi = 0 \tag{1.26}$$

This means that no torque is exerted in the direction of the angle of the leg, and the only force is exerted in the leg length direction which is used to hold

the leg length constant. The velocity of the system comes from it being an ideal system and recycling energy in the spring with close to ideal efficiency. In that case, the power in Eqs. 1.24 and 1.25. The powers that remain are the geometric work powers, which in the case of robotic legs are to be minimized.

$$P_1 = \frac{a_{12}a_{22}}{a_{11}a_{22} - a_{21}a_{21}} Q_l \dot{\phi} \tag{1.27}$$

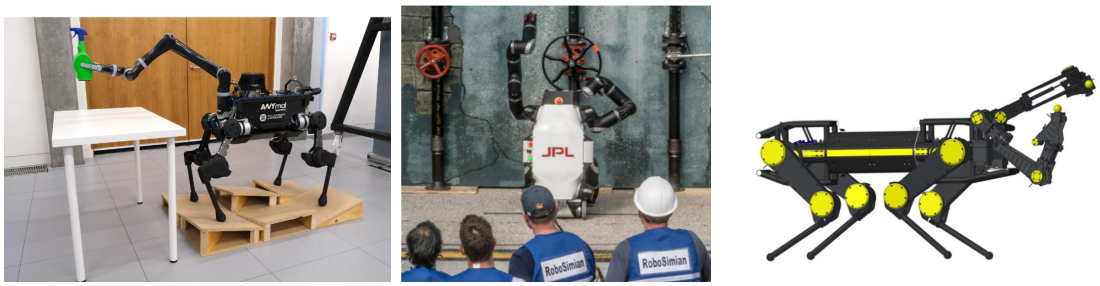
$$P_2 = \frac{-a_{12}a_{22}}{a_{11}a_{22} - a_{21}a_{21}} Q_l \dot{\phi} \tag{1.28}$$

For the geometric power to be zero, a single actuator has to solely act in the leg length direction meaning that the value of meaning that either a_{12} or a_{22} has to be zero.

1.3.2.3 Quadruped Robots Manipulation

Quadruped robots are available either as commercial platforms SPOT and ANYmal or other research platforms focusing on the locomotion part. This means that a limited number of quadrupeds include a manipulation component that enables them to interact effectively with their surroundings. Both ANYmal and Spot have optional neck gripper modules for pick and place operations. ANYmal is also proposed to be able to use its actual limbs to do simple manipulation such as opening doors or pushing objects.

This notion of a mobility platform with arms for mobility has been explored in the past with wheeled systems such as NASA Centaur [28] and Momaro [29], as well as with legged systems like Centaro [30] and RoboSimian [27]. Even though some quadruped robots are equipped with grippers they are not designed



(a) ANYmal [5] (b) RoboSimian [27] (c) HyQ2Max [9]

Figure 1.8: Quadruped Robot platforms popularized in recent years

to effectively manipulate the environment and perform delicate and precise tasks.

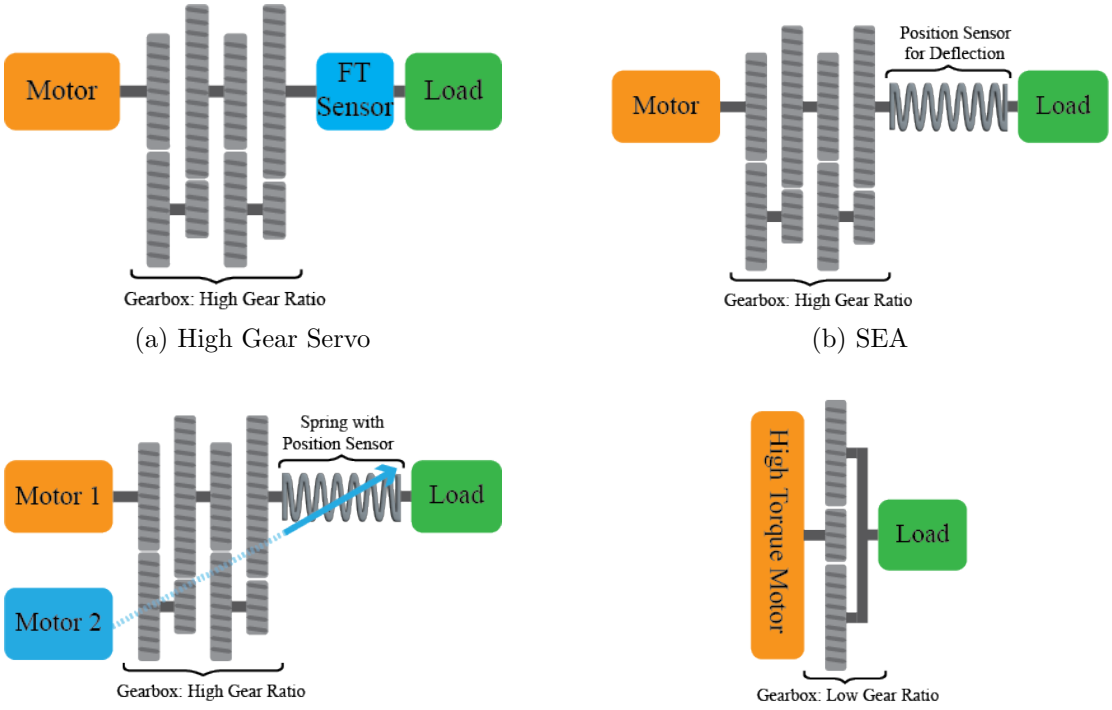
1.3.3 Actuators

Robotic actuators are at the core of any robotic system design, this research focuses on the types of actuators typically used and developed for legged robotics and grippers. The majority of robotic platforms that use electro-mechanical actuators employ one of these paradigms or a combination of them. Each type of actuator does have its advantages and disadvantages when used with robotic systems.

1.3.3.1 Position Controlled Servo Motors

Position-controlled actuators are a family of actuators that achieve high positional accuracy. The two most popular position-controlled actuators are servo motors and stepper motors. For this discussion, the focus will be on servo motors as stepper motors are rarely used in robotic joints.

Servo motors are motor modules that achieve high positional accuracy using a position control loop. Servo motors use a high-speed DC motor in series with a high reduction gear ratio. Through an internal loop, the position is measured and compared to a desired position, where the measurement of the position is achieved



(a) High Gear Servo

(b) SEA

(c) VSA

(d) QDD

Figure 1.9: Different robotic actuator diagrams

through encoders. Servo motors are very popular in the robotics industry as they are easy to control. Servo motors also provide high positional accuracy and can amplify motor torques on the gear ratio. Despite their benefits, servo motors suffer from a variety of problems when they are used in robotic systems.

Servomotors usually have a high gear ratio as can be seen in 1.9a, which means that even though the torque of the motor is amplified, the speed is sacrificed. This means that they are not ideal for highly dynamic systems. Moreover, the increased gear ratio introduces a large amount of non-linearity decreasing the open-loop torque transparency. This means that in applications where torque control is required, a Force/Torque sensor is needed to get accurate force readings and feedback. Servomotors are also vulnerable to impacts due to their high gear ratio. A high gear ratio results in a large reflected inertia making servos non-backdrivable. Since the reflected inertia is very high, any impact on the output of

the servomotor will feel like an impact on a rigid body. This might cause damage to the servo and anything that interacts with it. Some robots, however, still use Servo motors, especially for small robot applications [31].

1.3.3.2 Quasi-Direct Drive Actuators

Even though servo motors are the most popular in commercial robotics, the research community, alongside some commercial platforms, is migrating to more impact-resistant and high-bandwidth actuators. One of those actuators that recently gained popularity is the Quasi-direct drive actuator (QDD) [3] [32]. Quasi-direct drive actuators use a motor in series with a low gear ratio. However, to compensate for the reduced torque from the gearing, a large diameter, high torque motor is used as seen in 1.9d. The low gear ratio reduces the reflected inertia of the actuator and increases the torque transparency. The high transparency puts these actuators in the category of proprioceptive actuators. In a low-gearing scenario, the forward-driving torque can be closely similar to the back-driving torque. Hence, quasi-direct actuators can use internal sensors at the input to measure the current and translate that through the gear ratio into a torque measurement. This circumvents the need to measure the output torque of the actuator through an FT sensor.QDD actuators are ideal for dynamic locomotion as they have a high bandwidth and force control capability that is accurate enough for dynamic locomotion. However, if accurate force control is desired through only a proprioceptive actuator, then the gear ratio used should be minimized [33]. QQD are not limited to use in legged locomotion as they have also been used in gripper applications such as in DAnTe [34]. The downside of QDDs is their inability to store mechanical energy to be recycled unless a regenerative electrical system is used.

1.3.3.3 Compliant Actuators

Series elastic actuators [35] [36] (SEAs), shown in 1.9b are a family of actuators that intentionally introduce a compliant element between the motor gearbox output and the environment. SEA designs can vary between applications where the compliant element could be classified as linear, or non-linear. Another family of compliant actuators is variable stiffness actuators [37] (VSA), in Fig. 1.9c, where the stiffness of the compliant element is actively changed. For purposes of simplicity of presenting this work, VSA background is presented in this section. Including a compliant element between the gearbox output and the environment has multiple advantages that are not present in other actuators. The spring acts as a low-pass filter for high-frequency impacts as well as reduces the reflected inertia making the actuator more back-drivable. Also transforms the force control problem into a position control problem. With a very well-modeled and stable spring accurate force control is possible. This forgoes the need of using bulky and expensive FT sensors. These advantages come at the cost of decreasing the force bandwidth of the actuator. Of course, as with every actuator presented, there is an engineering trade-off that the choice of the stiffness element is very crucial.

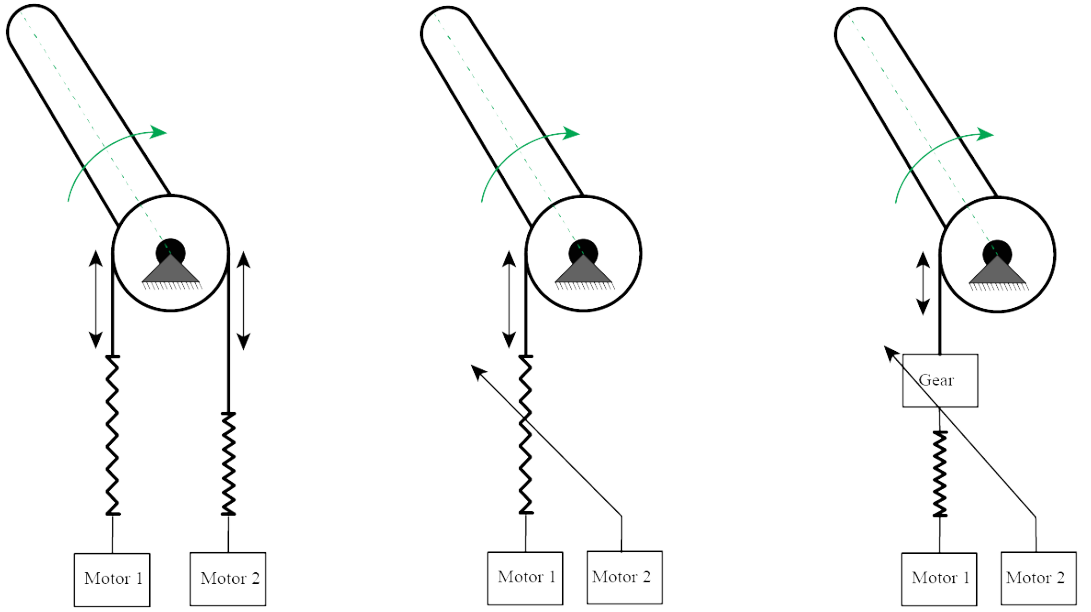
SEA: Linear Springs Most of the traditional SEAs use a linear compliant element that choice is made in order to simplify the design process as well as the control. Having a linear spring means that the force in the spring is proportional to the deflection meaning the force control is a straightforward problem [38]. This also reduces the complexity of the force control. However, having a spring with a fixed linear stiffness means that the stiffness has to be optimized for the intended task as a too-low stiffness reduces the bandwidth of the actuator and the capacity of the spring, while a very high stiffness gives an increased bandwidth but less impact mitigation [39] [40] [41]. Many robotic applications use series elastic actuators for dynamic robotic systems as well as simpler mechanisms such

as grippers and fingers [5] [10]. To mitigate the problems presented by linear SEA, researchers have developed alternatives to avoid this engineering trade some of these solutions include nonlinear springs and variable stiffness actuators.

SEA: Nonlinear Springs In order to overcome the issues with using a linear spring, researchers have adopted nonlinear springs with an optimized torque profile [42] in applications ranging from dynamic jumping motions of a robot [43] to prosthetic devices [44]. Presented nonlinear springs range from using magnets [45] [46], rubber [47], or even linear springs that are stretched in a nonlinear fashion [48].

Nonlinear springs exhibit a wider range of force/torque profiles than those expressed by linear springs, hence, compliant and stiff behaviors can be generated with a single nonlinear spring. The use of a nonlinear spring sacrifices the versatility of a SEA for a simpler design, making it especially beneficial for robotic grippers since the required force/torque range is small compared to other joints. Thus, a small variation in force/torque profile is enough to exploit the accurate force control in a compliant range and the high bandwidth in a stiffer range without increasing its size and weight. Even though nonlinear springs combine the best of the two worlds, they still suffer from a lack of versatility as the spring profile is still constant and the profile has to be optimized. Also, the modeling of the spring has to be accurate should the spring be used as a force sensor.

Variable Stiffness Actuators Online stiffness modulation could be a more versatile option than using SEAs. Impedance and compliance control afforded by online VSAs allow the robot to interact closely with it a broad array of environment. Some robotic joints use pure control methods to change the stiffness of the system by simulating the working of a spring's force response to deflection [49] [50]. However, using such a method does not allow for physical energy storage, inherent



(a) Antagonistic VSA

(b) Independent motor VSA

(c) Transmission variation VSA

Figure 1.10: Different VSA mechanism design diagrams

shock absorption, and explosive movement for fast response [51] [52] [53].

As suggested by the name, VSAs use a secondary input to actively alter the physical stiffness of the spring. This attribute resolves the stiff and soft spring trade-off seen in SEAs. The need for the secondary input, adds to the design and fabrication complexity of a VSA, as well as, it energy consumption. Hence, choosing between an SEA or a VSA highly depends on the constraints and requirements of the system and the task. Reviews such [37] [54] provide a comprehensive overview of variable stiffness actuators and their subcategories. Methods of stiffness variation employed in robotic joints can be categorized as follows:

- Changing the physical properties of a spring in series: This VSA design shown in 1.10b has a single motor in series with a variable stiffness spring. The spring material and stiffness variation (secondary input) is summarized below:

  - Stimuli-responsive polymers and nanomaterials: which use secondary input to change the mechanical properties of the material [55] [56].
  - Pneumatics: which use air pressure variation to change the stiffness of an artificial muscle [57] [58]
  - Electromagnetic: which uses coils and/or other electromechanical effect to change the stiffness of a magnetic spring [59]

- Spring pretension variation: this is most commonly used through an agonist-antagonistic configuration shown in 1.10a. In this configuration, two motors each with progressive springs tug on a single joint similar to biological joints [60] [61]. In an antagonistic design, the stiffness can be changed by pretensioning both sides of the joint concurrently. Positioning of the joint can then be achieved through pretensioning one side over the other to shift the equilibrium point. Antagonistic configuration requires the use of nonlinear progressive springs since using linear springs will not change the stiffness of the joint when pretension.

- Transmission ratio modulation: This is done by changing the rate at which a spring is engaged with respect to the same output deflection as shown in 1.10c. The most common design using this method is through using a pivoted mechanism and then changing the location of the pivot as presented in [62] [63] [64].

1.4 Organization

This dissertation introduces the SORELL robotic platform, its design philosophy, and its proposed uses. Chapter 2 will introduce the SORELL robot design and its unique body shape which provides a large workspace area and enables it to perform in upright or flipped positions. The leg design, complementary to this body, is also introduced and its sub-assemblies include the hip, femur, and knee

assemblies. Chapter 3 focuses on the improved design features of the knee joint and its broader implications on parallel actuator design. The knee design's role in reducing mechanical antagonism in the robotic and increasing leg gear train stiffness is demonstrated.

Chapters 5 and 4 introduce a library of series elastic and variable stiffness actuators for gripper applications. Chapter 4 encompasses the design and testing of two passive nonlinear magnetic SEAs, MSEA and PMSEA, which rely on permanent magnet arrangements to generate unique stiffness profiles. In Chapter 5 two magnetic VSAs are presented: (1) EMVSA, which uses a coil to change the stiffness of the magnetic spring. (2) AMVSA, a variable stiffness finger that uses mechanical input to change the orientation of magnets to alter the stiffness as well as the position. Finally, chapter 6 discusses the future potential of this work and evaluates the prospective application of the actuator library to SORELL for manipulation tasks.

CHAPTER 2

Sorell Platform

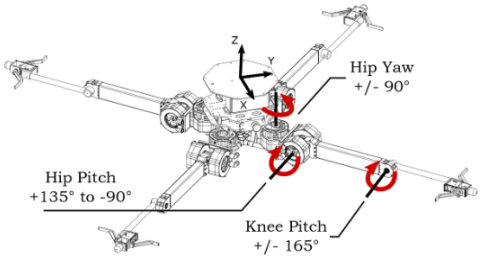
2.1 Introduction

The Shipboard Operations Robot with Enhanced Legged Locomotion (SORELL) is the next-generation quadruped robotic developed at RoMeLa. SORELL is designed to be effective in a shipboard environment navigating narrow corridors, knee-knockers, unstable ground, and stairs. SORELL platform shares the core design philosophy of ALPHRED-2 also developed by RoMeLa [1]. Even though SORELL shares the mobility features of ALPHRED-2, it has been designed for a different environment requiring various major upgrades in features and capabilities. Unlike ALPHRED-2, which is primarily a locomotion platform, SORELL is designed to be a locomotion as well as a manipulation platform. This means that SORREL will feature a number of peripheral units such as gripper modules, tools, cameras, and sensors. To that end, SORELL will be equipped with novel designs of these modules to meet the task requirements. The components of SORELL feature rational designs that have been optimized using simulation methods such as topology optimization and FEM analysis. This chapter presents the design methodology of SORELL and the mechanisms that enable this highly capable robot. It will also highlight the advancements made to the platform, compared to ALPHRED-2, and focus on the novel designs featured on SORELL.

2.2 SORELL and ALPHRED-2

2.2.1 ALPHRED-2 Platform

The successes of the ALPHRED-2 platform inspired the creation of SORELL, a more versatile successor. SORELL features many design improvements over its predecessor. To understand the scope of these improvements and the research done to achieve them, it is imperative to first evaluate the design of ALPHRED-2 and discuss its advantages and shortcomings.



(a) ALPHRED-2 kinematic configuration



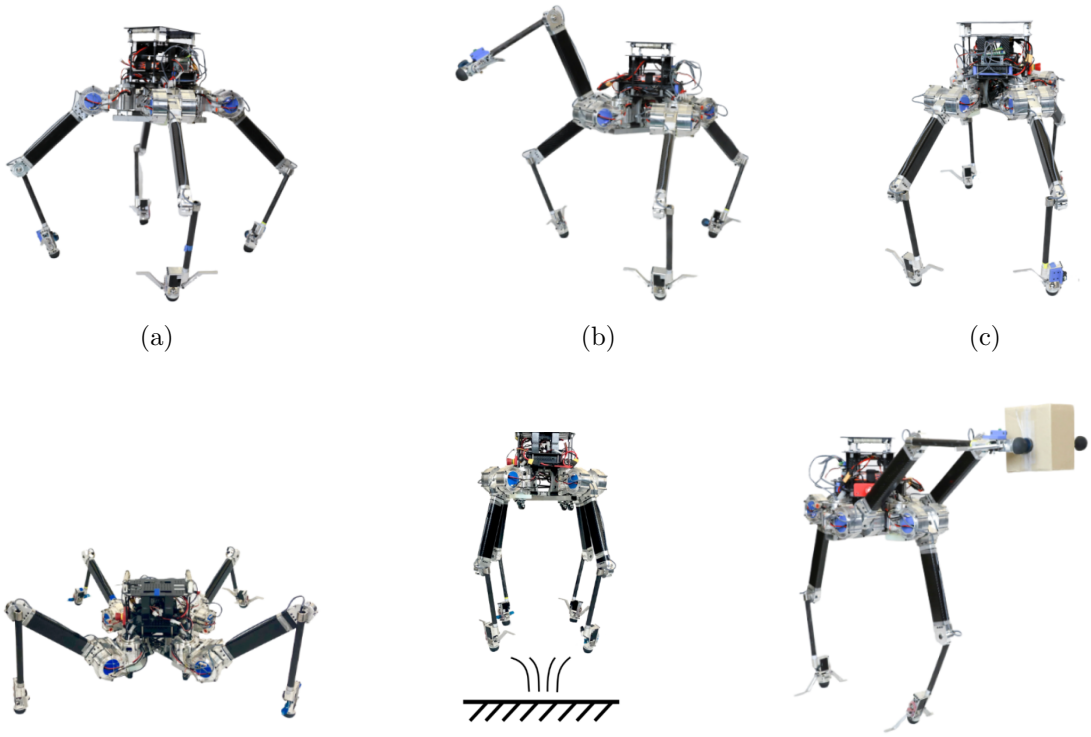
(b) ALPHRED-2 crossing street

Figure 2.1: ALPHRED-2 as presented in [1]

ALPHRED-2 is a quadruped robot that was developed as a mobility platform with a unique joint configuration. As opposed to traditional biologically inspired quadruped robots, where the hip joint has an abduction/adduction (hip roll) joint, ALPHRED-2 has a yaw joint. This configuration sacrifices some of the dynamic benefits of the joint in exchange for a larger workspace on the individual leg. This alteration enables the robot to equip itself with simple end-effectors at the leg to perform simple manipulation tasks with extended reach. Fig. 2.1 shows ALPHRED-2 robot in operation as well as its kinematic configuration.

The unique kinematic configuration of ALPHRED-2 enables the robot to operate in different modes as shown in Fig. 2.2. ALPHRED-2 is able to stand in

a stable way on four or three legs. While standing on three legs, the fourth limb can be freed to perform manipulation tasks. ALPHRED-2 is also able to stand on two legs, with the help of stabilizing mechanisms located at the feet, to perform dual arm manipulation. The robot is also capable of multiple locomotion configurations such as walking, trotting, caster wheel rowing, and jumping.



(a) (b) (c)

(d) (e) (f)

Figure 2.2: ALPHRED-2 Configurations: 2.2a Symmetric stable mode, 2.2b Tripod single manipulation mode, 2.2c Dynamic mode, 2.2d Caster wheeled mode, 2.2e Jumping/ pronking mode, 2.2f Biped dual manipulation mode [1]

Despite the large success of ALPHRED-2 as a platform, it suffers from a variety of shortcomings that need to be addressed for future applications. This research focuses on addressing the following:

- ALPHRED-2 has limited manipulation capability, hence certain tasks are not ideally suited for this robot. although simple manipulation tasks are

achievable through the tripod or biped modes, they remain limited. The robot for example is not able to grasp or manipulate precise objects.

- ALPHRED-2 uses the same BEAR actuator module for all joints to simplify the design of the robot, while the specific joint torque requirements are not considered over the whole design. Better performance can be achieved by catering the actuators based on the torque requirement of each joint. For instance, the hip yaw and knee joints do not require as much torque as the hip pitch for the intended gait. These factors affect the performance and weight of the robot and limit its battery life.

- The body of the robot is not designed to protect the mounted electronics and does not act as a structural unit of the robot, rather it primarily serves to connect the four hip joints. This has previously caused the robot's body to crack and the electronics to occasionally suffer damage from impacts during normal operation.

- The body design of the robot is not amenable to the addition of modular attachments, while the lack of body symmetry means that the robot can only operate in an upright position.

- The hip pitch and knee pitch motors of ALPHRED-2 are in a parallel configuration. As both actuators act on the hip joint a certain amount of antagonism arises. This means that for some stance configurations, both motors will be fighting each other. Coincidentally, ALPHRED-2 most used configuration 2.2a and 2.2c are operating with a high amount of antagonism between the two motors causing the hip motor to overheat and rapidly deplete the robot's battery power.

- The bi-articular knee joint uses a belt and pulley transmission to the knee joint. This configuration reduces the amount of flung mass by placing the

knee motor at the hip joint, but it also causes the belt to experience a high amount of torque. Due to the order of the transmission, the stiffness of the tibia is reduced. Subsequently, the belt teeth may deform causing a discrepancy between the knee joint output and the desired position.

These critical design shortcomings greatly hinder the versatility and precision of ALPHRED-2. SORELL's design and research target these limitations and implement adequate enhancements in the quadruped's design.

2.2.2 SORELL Platform

Apart from mitigating the shortcomings of ALPHRED-2, SORELL is designed to be a locomotion and manipulation platform. It is purposed for shipboard operations, hence it will inherit the locomotion and kinematics of ALPHRED-2. However, the design incorporates a symmetrical concave body design that is machined in one piece and optimized for structural stability and durability. It also incorporates a novel leg design to circumvent the problems caused by motor torque antagonism and belt stiffness. A new design of the hip joint also tailors more closely to the joint torque requirements as well as the ability to attach an assortment of modules for sensing and manipulation.

The early design concept of SORELL is shown in Fig. 2.3. This design incorporates higher torque motors, and a symmetrical body with ample area on the top and bottom to enable modular attachments. The planar symmetry of the body also allows the robot to operate on its top or bottom planes and perform manipulation tasks with body-attached grippers in either position as well. Fig. 2.4 also shows early concept tools and end-effectors intended to be used on SORELL's limbs.

These early adaptations have been updated with a more optimized design as shown in Fig. 2.5. Fig. 2.5a and Fig. 2.5b show the stable standing mode

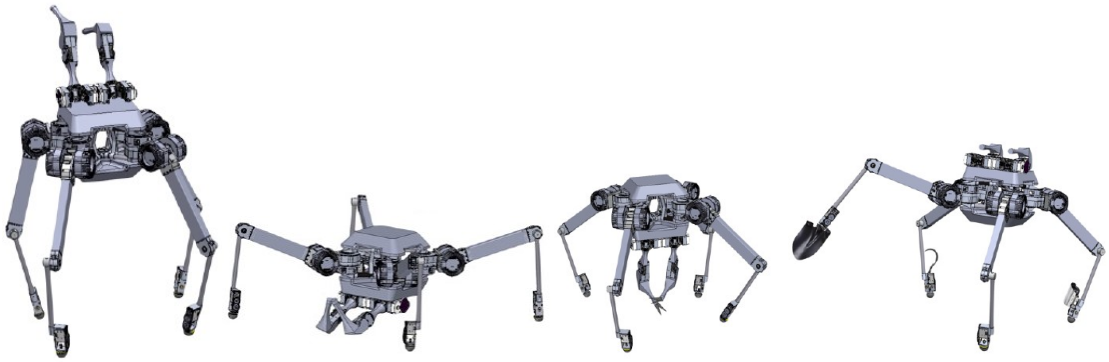


Figure 2.3: Early design adaptation of SORELL standing up

of SORELL as well as the dynamic mode for walking respectively. Fig. 2.5c shows the robot in tripod mode using a gripper attached to one of the legs for manipulation while Fig. 2.5d shows SORELL performing precise manipulation using small finger grippers attached to its belly in a squatting configuration.

2.2.3 SORELL Body

The SORELL body is designed and optimized to satisfy the design requirements discussed earlier. The body consists of an inner lightweight structure made primarily of carbon fiber sheets to contain the electronics and an outer body made of aluminum. The geometry of the outer aluminum body has been optimized to withstand high stresses to protect and hold the electronics securely in place. The shape of the body is made symmetrical to enable the robot to operate while flipped over. The shape is also designed to maximize the outer surface area to facilitate the attachment of modular equipment, see Fig. 2.6b. The connection between the outer body and the internal body is made through soft rubber connectors, which



(a) (b) (c) (d)

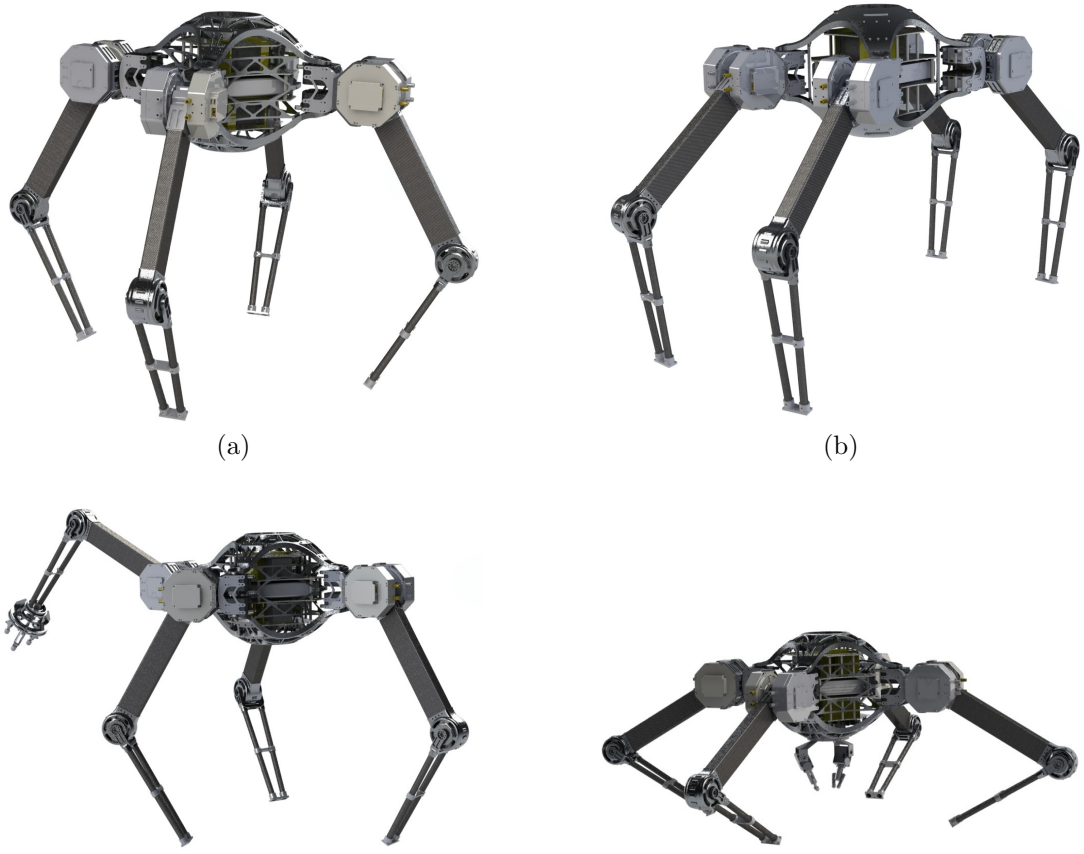
Figure 2.4: Modes of operation for early adaptation of SORREL

absorb shocks incurred during constant robot motion and impacts as shown in Fig. 2.6b.

The body of SORELL not only provides protection of the internal parts and enables symmetrical operation of the robot, but it also increases the workspace of the robot legs, this gives SORELL a large advantage over APHRED-2. Table 2.1 summarizes the range of motion of both robots. The curvature of the body frame and the fact that the entire electronics are inside the aluminum structure improve the hip pitch and yaw joint motions. Also, the body curves on the side of the frame give the hip joint the ability to get as close to the body as possible, as demonstrated in Fig. 2.7.

Table 2.1: Joint ranges for SORELL vs ALPHRED-2

Joint	ALPHRED-2	SORELL
$Hipyaw$	$[-90^\circ\ 90^\circ]$	$[-98^\circ\ 98^\circ]$
$Hip\ Pitch$	$[-90^\circ\ 135^\circ]$	$[-135^\circ\ 135^\circ]$
$Knee$	$[-165^\circ\ 165^\circ]$	$[-165^\circ\ 165^\circ]$



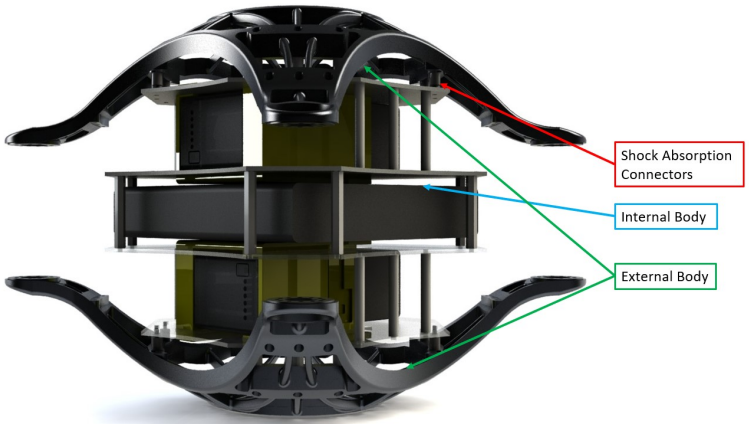
(a) (b)

(c) (d)

Figure 2.5: Modes of operation for SORREL

2.2.4 SORELL Leg Design

The most common designs for quadrupeds aim to minimize the flung mass of the limb by collocating the actuators as close to the body as possible as seen in ALPHRED-2. However, some quadrupeds maintain the serial configuration. Fig. 1.8 showed some of the common configurations of two DoF legs adopted by quadruped robots. As discussed earlier, parallel configurations restrict the motion of the actuators with respect to the body. This results in a reduced flung mass as the hip pitch motor will not be required to drive the knee motor in series. It also has the advantage of granting the hip joint more freedom of motion when performing manipulation tasks with one of the legs.



(a) Full body assembly



(b) External body frame

Figure 2.6: External and internal body structures

To incorporate all these features in one design that is optimized for SORELL's task a new leg design with a unique kinematic configuration is introduced. This design, shown in Fig. 2.8, also mitigates the shortcomings seen in ALPHRED-2's leg including mechanical antagonism and reduced mechanism stiffness.

The SORELL leg design consists of four sub-assemblies that are designed to optimize the size, torque capability, and kinematics of the joints. In this section, the leg design will be introduced but a deeper modeling of the leg's unique configuration will be discussed Ch. 3.

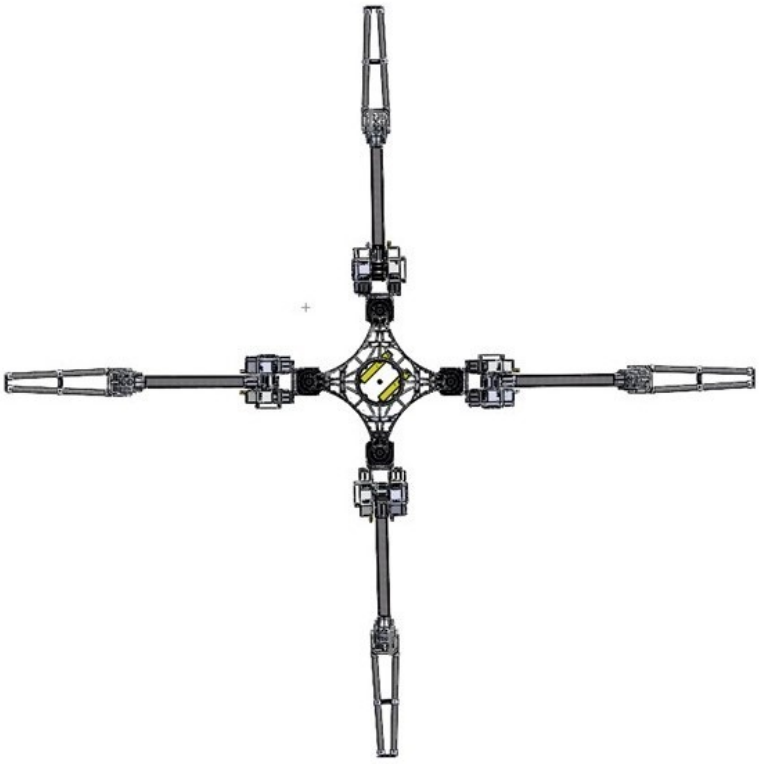


Figure 2.7: Top view of SORELL

2.2.4.1 Hip Joint

The hip design of SORELL is based on real and simulation data for the torque requirements of each DoF. As is the case with most quadruped robots, using the same actuator for all DoF's makes the design, assembly, and control simpler. For example, [1] uses the same size BEAR actuator for all three Dof's at the hip. However, using the same actuator poses the risk of over-designing the robotic joint for the intended gait and tasks. Some joints require more or less torque than what the same actuator can provide. Such a case is more clearly shown in the kinematic configuration adopted by SORELL, where the hip yaw joint does not need to support the weight of the robot. That means that if the robot is in the upright position, which is the most common configuration, the hip yaw joint only needs significant torque when swinging the leg or when twisting the body itself. This allows the hip yaw joint actuator to be scaled down.



(a) Side view (b) Isometric view

Figure 2.8: SORELL leg

For this joint two Koala BEAR actuators [65] were used in tandem. The two actuators are mounted on a bracket, Hip Yaw Bracket in Fig. 2.9, that aligns these actuators with the body and holds the connection to the next joint. Using two smaller actuators not only reduces the mass of the hip but also reduces the area needed for the joint to turn, giving it a larger range of motion as shown in Fig. 2.7 and detailed in Table 2.1. For the two pitch motors for the hip and knee, multiple factors affect the sizing of the actuators (see chapter 3 for a more comprehensive study). However, based on simulation results and the analyzed gait of SORELL significant mechanical antagonism occurs at some configurations of the leg, increasing the torque requirement for that joint. As will be shown in the following chapter, ALPHRED-2 suffered from mechanical antagonism on the hip pitch motor causing it to overheat. Added to that, the walking and trotting gaits of ALPHRED-2 have an increased hip motor requirement due to the placement of the foot during these instances. This can also be extended to SORELL since it has the same morphology as ALPHRED-2. SORELL's design also mitigates antagonism compared to ALPHRED-2, but, the flung mass of the

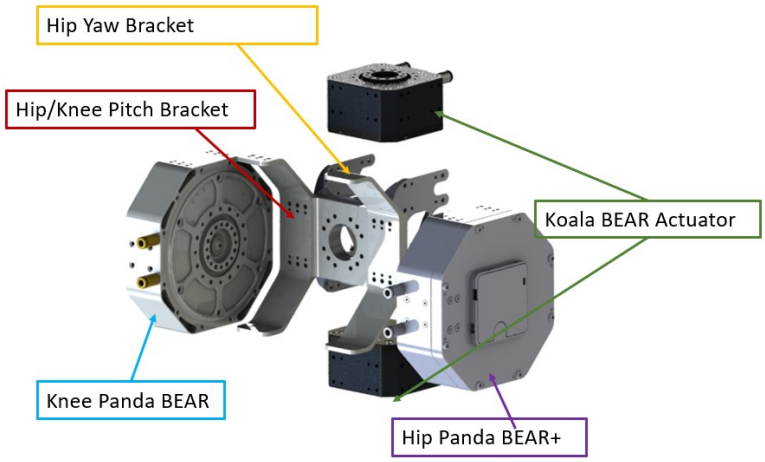


Figure 2.9: SORELL hip joint assembly

knee joint requires a larger hip motor size for smother operation. For the hip pitch motor, the larger Panda BEAR+ actuator was used, while a regular BEAR motor for the knee joint. The components of the hip are shown in Fig. 2.9. The attributes of the actuators used on the SORELL hip are detailed in Table 2.2.

Table 2.2: Actuator properties used on SORELL

Joint	Actuator	Peak torque (15s)	Peak torque (1.5s)	Gear ratio
Hip yaw	2 *KB*	8.2Nm	28Nm	9
Hip Pitch	*PB+*	33Nm	67Nm	6
Knee Pitch	*PB*	16.8Nm	33.5Nm	6

The brackets used in the hip design are optimized to minimize the weight of the robot while maintaining sufficient rigidity of the joint. This is done by minimizing the weight of the brackets as well as coupling the actuators with the bracket in such a way that the actuators themselves provide added structural support and stability. As shown in Fig. 2.9 the Koala BEAR actuators support the joint laterally while the Panda and Panda+ actuators support the hip/knee pitch bracket in the vertical direction.

2.2.4.2 Knee and Femur

The placement of the actuators for SORELL is identical to that of ALPHRED-2 and so is the basic design of the femur. The hip pitch motor directly drives the femur linkage while the knee pitch motor acts on the knee joint through a belt internally connecting the master and slave pulleys inside the femur 2.10. However, the main difference between the knee and femur design for SORELL is the relocation of the knee motor gearbox from inside the knee motor to the knee joint. This design is also a parallel configuration, but the relocation of the gearbox has implications on the kinematics of the leg and the relationship between the joint and actuator space.

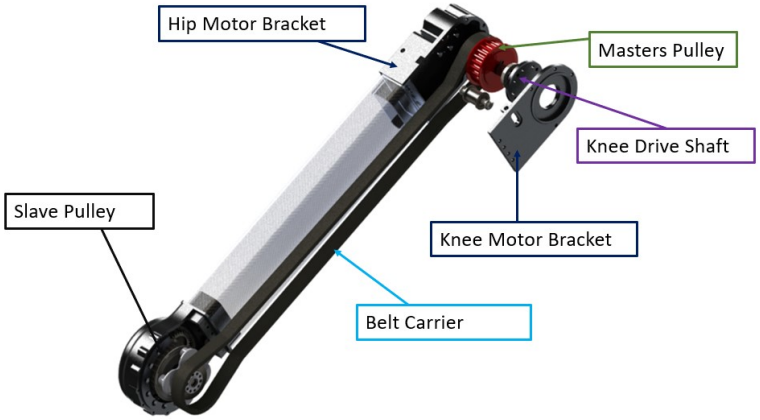


Figure 2.10: SORELL femur assembly

The knee design, shown in Fig. 2.11, consists of a central slave pulley sandwiched between two planetary gearboxes that each have a gearing ratio of 1:5. Each set of planetary gearboxes resides in a separate bracket. The slave pulley rotates on a shaft that runs through both sides of the assembly and is hinged on the inner part of each gearbox's carrier. The carriers of both planetary gearboxes are then combined at the output to the next link.

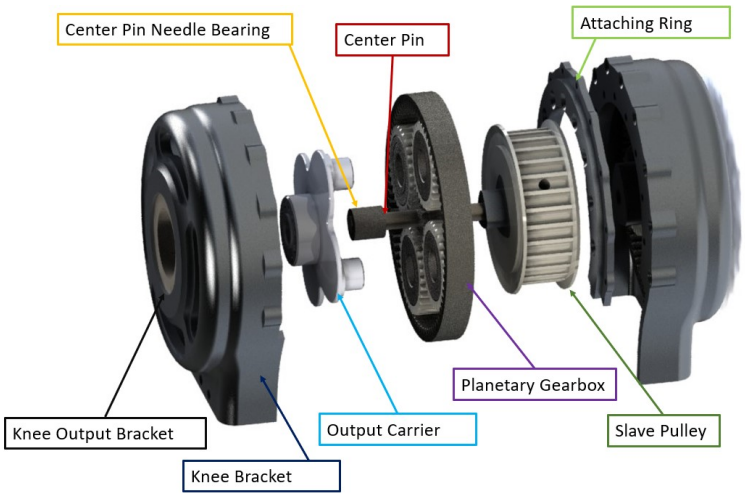


Figure 2.11: SORELL knee assembly

2.2.4.3 Tibia

The tibia, shown in Fig. 2.12, is the last actuated limb in the design assembly. The tibia knee bracket connects both outputs from the knee gearboxes. Similar to the femur, the tibia consists of two carbon fiber rods connected together through three aluminum brackets. The angled nature of the tubes reduces the size of the foot and decreases the radial forces on the knee gearbox output. A hard stop is also incorporated in the tibia design such that the robot can rest on it when performing manipulation tasks in a squatting position. The hard stop will reduce the torque needed to support the weight of the robot at a position where the torque on the knee will be at its maximum.

2.3 SORREL Manufacturing

SORELL was fully manufactured in-house through 5-axis CNC machining. The knee gearbox parts shown in Fig. 2.13, were customized by machining standard gears and pulleys into the desired geometries. Fig. 2.13b shows the sandwich gearbox configuration, which consisted of the slave pulley situated between two planetary gearboxes. Fig. 2.13a shows the manufactured knee joint with the knee-

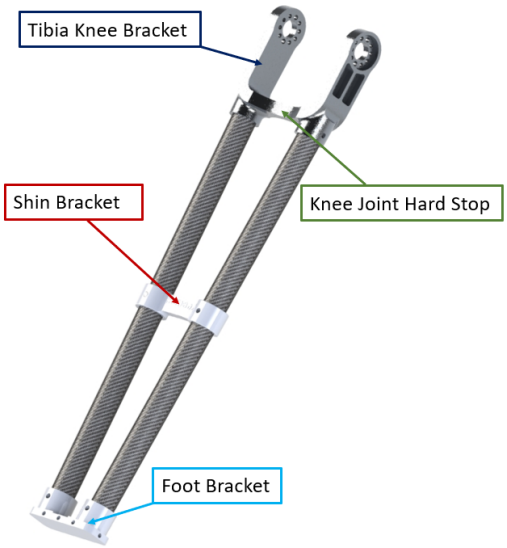
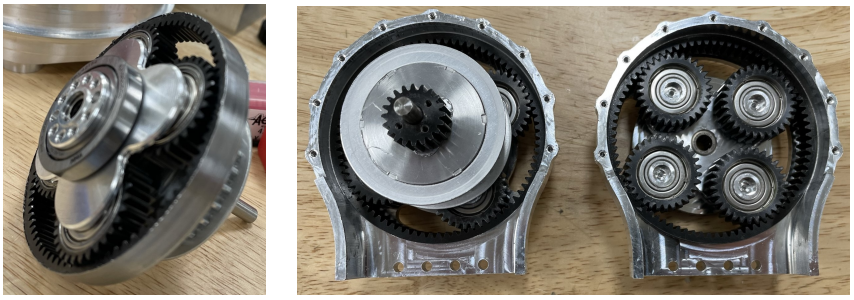


Figure 2.12: SORELL tibia assembly

located gearbox. As can be seen, the knee gearbox consists of two sandwiched gearboxes with the driven knee pulley in the middle. Fig. 2.14, shows one assembled femur linkage with the knee gearbox attached, and Fig. 2.15 shows the completed and assembled robot SORELL.



(a) Knee gearbox (b) Knee joint

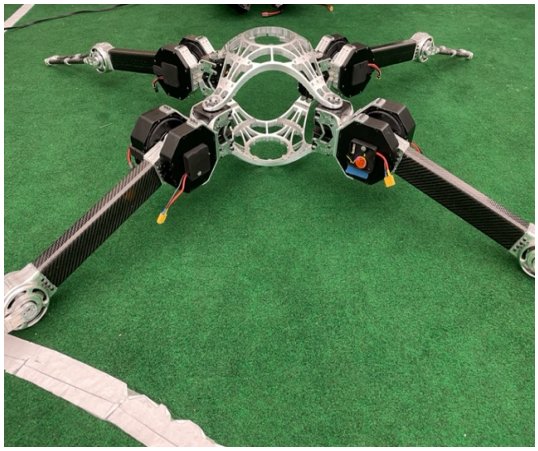
Figure 2.13: Manufactured knee gearbox

2.4 SORELL Attachments

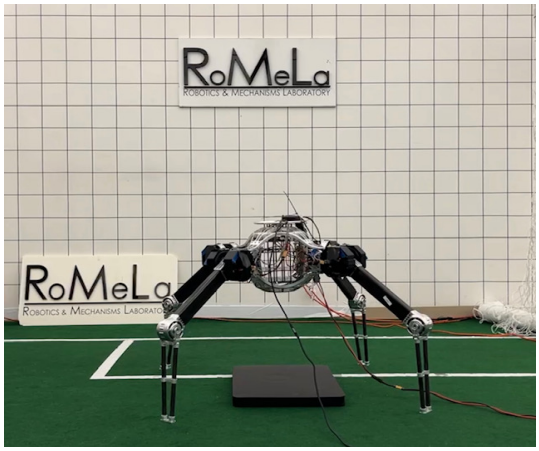
SORELL is developed to be both a manipulation and a locomotion platform. This section discussed the design and application of SORELL. In the following



Figure 2.14: Manufactured femur link with Knee joint gear box



(a) Lying flat



(b) Standing up

Figure 2.15: Manufactured and assembled SORELL

chapter, a deeper dive into the unique design of SORELL's leg will be presented, its advantages, and the implications of the design for the quadruped robot.

Besides the design of the leg, SORELL is designed to enable the attachment of variable grippers and utility gadgets to enable the robot to traverse complex environments and manipulate them in a precise and safe way. These attachments include but are not limited to grippers, sensory attachments, and caster wheels for the robot to roll on. To enable such manipulation capability, a family of grippers was developed to assist future deployment of SORELL.

CHAPTER 3

Sorell Leg

3.1 Introduction

The kinematic design of a quadruped leg is crucial to the behavior and performance of the robot. As discussed in previous chapters, in the case of a quadruped robot with similar leg designs to ALPHRED-2, the amount of antagonism during the stance phase of the gait is high.

Traditionally, robotic actuators were thought of as a single black box unit that includes the motor windings and the gearbox. Hence, the focus was on the placement of the actuators in a kinematic mechanism. The design of SORELL's leg shifts the thinking of the motor-gearbox being a single unit. This method introduces an added degree of freedom to the design of robotic legs based not just on the placement of the actuator but also on their respective gearboxes. This will open the door for future optimization of leg designs and the placement of gearboxes throughout the mechanism.

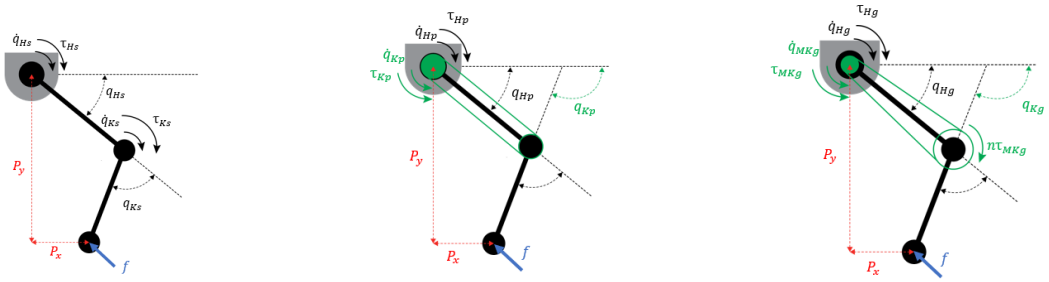
This chapter presents a detailed overview of the design of the SORELL leg, a justification for the presented design as well as theoretical, simulation, and experimental studies to compare the performance of the leg to common leg designs based on the expected gait of SORELL. This chapter also studies the expected antagonism in the designed leg as well as other advantages and shortcomings.

3.2 Theoretical Modeling

3.2.1 Leg Kinematics

Shifting the gearbox from the motor to the knee joint has implications on the kinematics of the leg. Compared to the parallel case present in ALPHRED-2, SORELL's leg is also considered a parallel mechanism. Since there is a degree of coupling between the hip and the knee joint a new kinematic model needs to be developed for this unique mechanism. The design of the leg follows a biarticular design meaning that both actuators are located at the hip, however, one of the actuators acts on two linkages instead of one. Hence, revisiting the modeling kinematics of the parallel and serial cases presented in Ch. 1 will be crucial to developing the new kinematic model.

Fig. 3.1 shows the diagrams of the three cases analyzed in this section. As previously discussed the knee and hip joint torques and angles, denoted by (tau_{j1}, tau_{j2}) and (q_{j1} and q_{j2}) respectively, are coordinate-invariant. The location of the contact point of the foot away from the body in the x- and y-directions is P_x and P_y and the contact force acting on the foot is f. On the other hand, the actuator space is dependent on the kinematics and will be affected in each of the cases. For the following analysis, only the static case is considered.



(a) Serial (b) Parallel (c) Parallel Knee GB

Figure 3.1: The three different configurations considered for this analysis

The serial configuration Fig. 3.1a considers the case where the actuators are

placed at the joints. the hip and knee motor torques and angles are denoted by (τ_{Hs}, τ_{Ks}) and (q_{Hs} and q_{Ks}) respectively.

For the parallel configuration in Fig. 3.1b, the knee joint is driven through a bi-articular mechanism, a belt in this case. The hip and knee motor torques and angles by (τ_{Hp}, τ_{Kp}) and (q_{Hp} and q_{Kp}) respectively.

For the last configuration shown in Fig. 3.1c, both motors are located at the hip; however, the knee motor gearbox is removed from the knee actuator and a new knee gearbox is designed and relocated to the knee joint. Hence, the knee motor also acts on the knee joint through a biarticular mechanism. The hip and knee motor torques and angles are denoted by (τ_{Hg}, τ_{Kg}) and (q_{Hg} and q_{Kg}) respectively and n denotes the knee gear transmission gear ratio. From here onwards, the new gearbox configuration will be referred to as (knee GB) for simplicity.

To compare the cases, the relationship between the actuator and joint torques is first presented in the static case. These relations depict the actuator torques required in each configuration in Fig. 3.1 needed to satisfy the joint torques in Fig. 1.3

$$\tau_{j1} = \tau_{Hs} \qquad \tau_{j2} = \tau_{Ks} \tag{3.1}$$

$$\tau_{j1} = \tau_{Hp} + \tau_{Kp} \qquad \tau_{j2} = \tau_{Kp} \tag{3.2}$$

$$\tau_{j1} = \tau_{Hg} + \tau_{MKg} \qquad \tau_{j2} = n\tau_{MKg} \tag{3.3}$$

Equation 3.1 shows that the torque on the joint in the serial configuration is equal to the actuator torques, that's due to the placement of the actuators on the joints. For the parallel configuration, 3.2 shows that the torque acting on the hip joint is the sum of both actuator torques. This is due to the coupling between

the two actuators, as the belt running around the two pulleys also results in a reaction torque around the axis connecting the two pulleys. That means that when the torques are of opposite signs the actuators fight each other to satisfy the joint torque needed. However, when the toque signs are the same the actuators cooperate to achieve the required joint torque. As for the knee joint, the torque will be equal to the torque of the knee actuator as the pulley stage has a 1:1 gearing ratio.

On the other hand, Equation 3.3 shows that the torque at the hip joint when the knee gearbox is relocated to the knee joint is still the sum of torques of both actuators. However, in this case, the knee motor torque acting on the hip τ_{MKg} is the pre-geared torque which when compared to the parallel case, τ_{Kp}, is lower by a factor of n which is the gearing ratio. It is important to note that for all cases the torque on the joint will be the same as that is only dependent on the linkage angles and the contact force which is the same for all cases.

The kinematics of each case are derived here:

For the serial mechanism,

$$P_x = L_1 cos(q_{Hs}) + L_2 cos(q_{Hs} + q_{Ks}) \tag{3.4}$$

$$P_y = -L_1 sin(q_{Hs}) - L_2 sin(q_{Hs} + q_{Ks}) \tag{3.5}$$

Partial differentiation of Eqs. 3.4 and 3.5 gives the following:

$$\begin{bmatrix} \dot{P}_x \\ \dot{P}_y \end{bmatrix} = \begin{bmatrix} -L_1 sin(q_{Hs}) - L_2 sin(q_{Hs} + q_{Ks}) & -L_2 sin(q_{Hs} + q_{Ks}) \\ -L_1 cos(q_{Hs}) - L_2 cos(q_{Hs} + q_{Ks}) & -L_2 cos(q_{Hs} + q_{Ks}) \end{bmatrix} \begin{bmatrix} \dot{q_{H_s}} \\ \dot{q_{K_s}} \end{bmatrix} \tag{3.6}$$

For the parallel mechanism,

$$P_x = -L_1 cos(q_{Hp}) - L_2 cos(q_{Kp}) \tag{3.7}$$

$$P_y = -L_1 sin(q_{Hp}) - L_2 sin(q_{Kp}) \tag{3.8}$$

$$\begin{bmatrix} \dot{P}_x \\ \dot{P}_y \end{bmatrix} = \begin{bmatrix} -L_1 sin(q_{Hp}) & -L_2 sin(q_{Kp}) \\ -L_1 cos(q_{Hp}) & -L_2 cos(q_{Kp}) \end{bmatrix} \begin{bmatrix} \dot{q_{H_p}} \\ \dot{q_{K_p}} \end{bmatrix} \tag{3.9}$$

Hence, it can be shown that the transpose of the jacobian, relating the forces at the foot to the actuator torques in the static case can be written for both cases as:

$$J_s^T = \begin{bmatrix} -L_1 sin(q_{Hs}) - L_2 sin(q_{Hs} + q_{Ks}) & -L_1 cos(q_{Hs}) - L_2 cos(q_{Hs} + q_{Ks}) \\ -L_2 sin(q_{Hs} + q_{Ks}) & -L_2 cos(q_{Hs} + q_{Ks}) \end{bmatrix} \tag{3.10}$$

$$J_p^T = \begin{bmatrix} -L_1 sin(q_{Hp}) & -L_1 cos(q_{Hp}) \\ -L_2 sin(q_{Kp}) & -L_2 cos(q_{Kp}) \end{bmatrix} \tag{3.11}$$

Where J_s^T and J_s^T are the transpose of the jacobians for the serial and parallel cases respectively.

The relationship between the actuator torques and the contact force f for the serial and parallel cases can then be written as,

$$\begin{bmatrix} \tau_{Hs} \\ \tau_{Ks} \end{bmatrix} = J_s^T \begin{bmatrix} f_x \\ f_y \end{bmatrix} \tag{3.12}$$

and for the parallel case

$$\begin{bmatrix} \tau_{Hp} \\ \tau_{Kp} \end{bmatrix} = J_p^T \begin{bmatrix} f_x \\ f_y \end{bmatrix} \tag{3.13}$$

By combining equations 3.1, 3.2 with 3.12 and 3.13 the torque at the joint for serial and parallel cases can be written as:

$$\begin{bmatrix} \tau_{j1} \\ \tau_{j2} \end{bmatrix} = \begin{bmatrix} 1 & 0 \\ 0 & 1 \end{bmatrix} J_s^T \begin{bmatrix} f_x \\ f_y \end{bmatrix} = \underbrace{\begin{bmatrix} 1 & 0 \\ 0 & 1 \end{bmatrix}}_{\text{Config. Matrix } G_s} \begin{bmatrix} \tau_{Hs} \\ \tau_{Ks} \end{bmatrix} \tag{3.14}$$

For the parallel case

$$\begin{bmatrix} \tau_{j1} \\ \tau_{j2} \end{bmatrix} = \begin{bmatrix} 1 & 1 \\ 0 & 1 \end{bmatrix} J_p^T \begin{bmatrix} f_x \\ f_y \end{bmatrix} = \underbrace{\begin{bmatrix} 1 & 1 \\ 0 & 1 \end{bmatrix}}_{\text{Config. Matrix } G_P} \begin{bmatrix} \tau_{Hp} \\ \tau_{Kp} \end{bmatrix} \tag{3.15}$$

Using 3.14, 3.15, 3.1 and 3.2, the relationship between the contact force and the actuator torques in the knee GB case follows as,

$$\begin{bmatrix} \tau_{j1} \\ \tau_{j2} \end{bmatrix} = \begin{bmatrix} 1 & 1 \\ 0 & 1 \end{bmatrix} J_p^T \begin{bmatrix} f_x \\ f_y \end{bmatrix} = \underbrace{\begin{bmatrix} 1 & 1 \\ 0 & n \end{bmatrix}}_{\text{Config. Matrix } G_{Pg}} \begin{bmatrix} \tau_{MHg} \\ \tau_{MKg} \end{bmatrix} \tag{3.16}$$

$$\begin{bmatrix} \tau_{j1} \\ \tau_{j2} \end{bmatrix} = \begin{bmatrix} 1 & 1 \\ 0 & n \end{bmatrix} \begin{bmatrix} \tau_{MHg} \\ \tau_{MKg} \end{bmatrix} \tag{3.17}$$

$$\begin{bmatrix} \dot{q}_{j1} \\ \dot{q}_{j2} \end{bmatrix} = \begin{bmatrix} 1 & 0 \\ 1/n & 1/n \end{bmatrix} \begin{bmatrix} \dot{q}_{MHg} \\ \dot{q}_{MKg} \end{bmatrix} \tag{3.18}$$

$$\begin{bmatrix} \tau_{MHg} \\ \tau_{MKg} \end{bmatrix} = \begin{bmatrix} 1 & 1 - \frac{1}{n} \\ 0 & \frac{1}{n} \end{bmatrix} J_p^T \begin{bmatrix} f_x \\ f_y \end{bmatrix} \tag{3.19}$$

The gearing matrices that differentiate between the three kinematic cases are denoted by G_s, G_P and G_{Pg}. These matrices depict the relationship between the actuator and the joint space. Hence, the jacobian for the parallel case with the gearbox at the knee can be written as:

$$J_{pg}^T = \begin{bmatrix} -L_2 sin(q_{Kp})(\frac{1}{n} - 1) - L_1 sin(q_{Hp}) & -L_1 cos(q_{Hp}) - L_2 cos(q_{Kp})(\frac{1}{n} - 1)) \\ -L_2 sin(q_{Kp})\frac{1}{n} & -L_2 cos(q_{Kp})\frac{1}{n} \end{bmatrix} \tag{3.20}$$

note that the jacobian J_{pg}^T is written in terms of the parallel configuration

actuator angles, not the actuator angles of the new configuration. However, a simple transformation between the two is as follows:

$$\begin{bmatrix} \dot{q}_{Hg} \\ \dot{q}_{Kg} \end{bmatrix} = \begin{bmatrix} 1 & 0 \\ 1-n & n \end{bmatrix} \begin{bmatrix} \dot{q}_{Hp} \\ \dot{q}_{Kp} \end{bmatrix} \tag{3.21}$$

3.2.2 Leg Dynamics

The new leg design relocates a considerable chunk of mass from the hip joint to the knee. Increasing the flung mass of the leg does have implications in the dynamic sense, therefore, it is important to model the dynamics of the new configuration and compare them to make sure that the advantages of the static case are not overtaken by the disadvantages introduced in the dynamic case. Using the same simulation data for the forces acting on the foot along with the angles a more comprehensive comparison can be achieved.

The dynamic equations for the two DoF manipulators in the joint space are

$$B_j = \begin{bmatrix} I_1 + I_2 + m_2 L_2^2 + 2m_2 a_2 L_2 cos(q_{j2}) & I_2 + m_2 L_1 a_2 cos(q_{j2}) \\ I_2 + m_2 L_1 a_2 cos(q_{j2}) & I_2 + m_2 a_2^2 \end{bmatrix} \tag{3.22}$$

$$V_j = \begin{bmatrix} -m_2 a_2 L_1 sin(\dot{q_2}^2 + 2\dot{q_1}\dot{q_2}) \\ m_2 a_2 L_1 sin(q_1)\dot{q_1}^2 \end{bmatrix} \tag{3.23}$$

$$G_j = \begin{bmatrix} g m_1 m_2 a_1 L_1 cos(q_1) + g m_2 a_2 cos(q_1 + q_2) \\ g m_2 a_2 cos(q_1 + q_2) \end{bmatrix} \tag{3.24}$$

The actuator torque equations follow from equations 3.22, 3.23 and 3.24.

The dynamic actuator torque for the serial case is written as.

$$\begin{bmatrix} \tau_{Hs} \\ \tau_{Ks} \end{bmatrix} = B_{js} \begin{bmatrix} \ddot{q_{Hs}} \\ \ddot{q_{Ks}} \end{bmatrix} + V_{js} + G_{js} + J_s^T \begin{bmatrix} f_x \\ f_y \end{bmatrix} \tag{3.25}$$

For parallel,

$$\begin{bmatrix} \tau_{Hp} \\ \tau_{Kp} \end{bmatrix} = B_{jp} \begin{bmatrix} \ddot{q_{Hp}} \\ \ddot{q_{Kp}} \end{bmatrix} + V_{jp} + G_{jp} + J_p^T \begin{bmatrix} f_x \\ f_y \end{bmatrix} \tag{3.26}$$

For knee GB,

$$\begin{bmatrix} \tau_{Hg} \\ \tau_{Kg} \end{bmatrix} = B_{jpg} \begin{bmatrix} \ddot{q_{Hg}} \\ \ddot{q_{Kg}} \end{bmatrix} + V_{jpg} + G_{jpg} + J_{pg}^T \begin{bmatrix} f_x \\ f_y \end{bmatrix} \tag{3.27}$$

The mass, coriolis, and gravitational matrices in Eq. 3.22, Eq. 3.23 and Eq. 3.24 take different values depending on the configurations and distribution of masses in the different links. To compare the three mechanisms fairly, all link lengths are selected to be the same. The major difference is where the mass center is located on the link. For the serial case, the knee actuator is placed on the axis of the hip actuator to give the best-case scenario for the torque needed as that reduces the flung mass of the femur, the knee actuator then acts through a belt to the knee joint. The parallel and the knee GB configurations follow the same hip design, however, the mass and moment of inertia of the femur are altered to relocate the mass of the gearbox to the knee joint in the second case.

3.3 Mechanical Antagonism

Mechanical antagonism is a major factor in the design of this leg. To study the mechanical antagonism in the derived models the problem is reformulated to reflect a more general approach. Earlier, the configuration matrix G was introduced, which relates the torques and angles of the actuators to the torque and angles in the joint space. To give a more comprehensive view of this study and to allow for future development of this concept the previous equations are rewritten in terms of the angles and torques of the pre-geared motors for all cases. That will give the researcher a better idea of how to optimize the gear distribution throughout mechanisms. In the following analysis, the pre-geared torque will be referred to as the BLDC torque as that is the kind of electric motor used in BEAR actuators.

The problem will be reformulated to match that shown in Eq. 3.28 which relates the joint space to the actuator space of the pre-geared motors.

$$\begin{bmatrix} \tau_{j1} \\ \tau_{j2} \end{bmatrix} = \underbrace{\begin{bmatrix} c_{11} & c_{12} \\ c_{21} & c_{22} \end{bmatrix}}_{\text{Config. Matrix } C} \begin{bmatrix} \bar{\tau}_H \\ \bar{\tau}_K \end{bmatrix} \tag{3.28}$$

The matrix C reflects not just the kinematics of the mechanism but also the gear distribution throughout the mechanism. for instance, the variable c_{12} reflects the projection of the torque of the knee motor on the hip joint and vice versa for c_{21}.

The pre-gear torques of the BLDC motors are labeled as follows $\bar{\tau}_{Hs}$, $\bar{\tau}_{Ks}$, $\bar{\tau}_{Hp}$, $\bar{\tau}_{Kp}$, $\bar{\tau}_{Hg}$ and $\bar{\tau}_{Kg}$ for the hip and knee BLDC motor torques for the serial, parallel and knee GB cases respectively. Similarly, $\bar{\dot{q}}_{Hs}$, $\bar{\dot{q}}_{Ks}$, $\bar{\dot{q}}_{Hp}$, $\bar{\dot{q}}_{Kp}$, $\bar{\dot{q}}_{Hg}$ and $\bar{\dot{q}}_{Kg}$ are the respective velocities of the BLDC motors.

The relationship between the joint and the actuator space for torque can be

rewritten as follows for the three cases studied.

Serial:

$$\begin{bmatrix} \tau_{j1} \\ \tau_{j2} \end{bmatrix} = \underbrace{\begin{bmatrix} n & 0 \\ 0 & n \end{bmatrix}}_{\text{Config. Matrix } C_S} \begin{bmatrix} \bar{\tau}_{Hs} \\ \bar{\tau}_{Ks} \end{bmatrix} \tag{3.29}$$

Parallel:

$$\begin{bmatrix} \tau_{j1} \\ \tau_{j2} \end{bmatrix} = \underbrace{\begin{bmatrix} n & n \\ 0 & n \end{bmatrix}}_{\text{Config. Matrix } C_P} \begin{bmatrix} \bar{\tau}_{Hs} \\ \bar{\tau}_{Ks} \end{bmatrix} \tag{3.30}$$

Parallel with a knee gearbox

$$\begin{bmatrix} \tau_{j1} \\ \tau_{j2} \end{bmatrix} = \underbrace{\begin{bmatrix} n & 1 \\ 0 & n \end{bmatrix}}_{\text{Config. Matrix } C_g} \begin{bmatrix} \bar{\tau}_{Hs} \\ \bar{\tau}_{Ks} \end{bmatrix} \tag{3.31}$$

The relationships relating the angles of the BLDC motors to the joint space angles can be written similarly.

Serial:

$$\begin{bmatrix} \dot{q}_{j1} \\ \dot{q}_{j2} \end{bmatrix} = \underbrace{\begin{bmatrix} \frac{1}{n} & 0 \\ 0 & \frac{1}{n} \end{bmatrix}}_{\text{Config. Matrix } C_S^{-T}} \begin{bmatrix} \bar{\dot{q}}_{Hs} \\ \bar{\dot{q}}_{Ks} \end{bmatrix} \tag{3.32}$$

Parallel:

$$\begin{bmatrix} \dot{q}_{j1} \\ \dot{q}_{j2} \end{bmatrix} = \underbrace{\begin{bmatrix} \frac{1}{n} & 0 \\ -\frac{1}{n} & \frac{1}{n} \end{bmatrix}}_{\text{Config. Matrix } C_P^{-T}} \begin{bmatrix} \bar{\dot{q}}_{Hp} \\ \bar{\dot{q}}_{Kp} \end{bmatrix} \tag{3.33}$$

Parallel with a knee gear-box

$$\begin{bmatrix} \dot{q}_{j1} \\ \dot{q}_{j2} \end{bmatrix} = \underbrace{\begin{bmatrix} \frac{1}{n} & 0 \\ -\frac{1}{n^2} & \frac{1}{n} \end{bmatrix}}_{\text{Config. Matrix } C_g^{-T}} \begin{bmatrix} \bar{\dot{q}}_{Hg} \\ \bar{\dot{q}}_{Kg} \end{bmatrix} \tag{3.34}$$

In all of these relationships, it is assumed that the gearbox connected to both the hip motor as well as the knee motor have the same reduction ratio n. However, this can be changed depending on the requirements of each joint as will be discussed in Ch. 6. To simplify the analysis, the same gearing ratio will be used for both actuators.

The geometric work in the case of a moving leg, depends on the trajectory of the leg. In the case that the trajectory follows that of a SLIP model, one actuator is responsible for supporting the robot and another is responsible for the angle the model makes with the ground. Even though the dynamics of SORELL's leg do not mimic the SLIP model exactly, the SLIP model is still valid for comparison of mechanisms that approximately follow these dynamics.

To evaluate the geometric work as was introduced in Ch. 1 the motor torques need to be rewritten to reflect the SLIP model angle, ϕ, and leg length l_m Fig. 3.2

If the angle of the knee is as shown in Fig. 3.2 and assuming both the femur

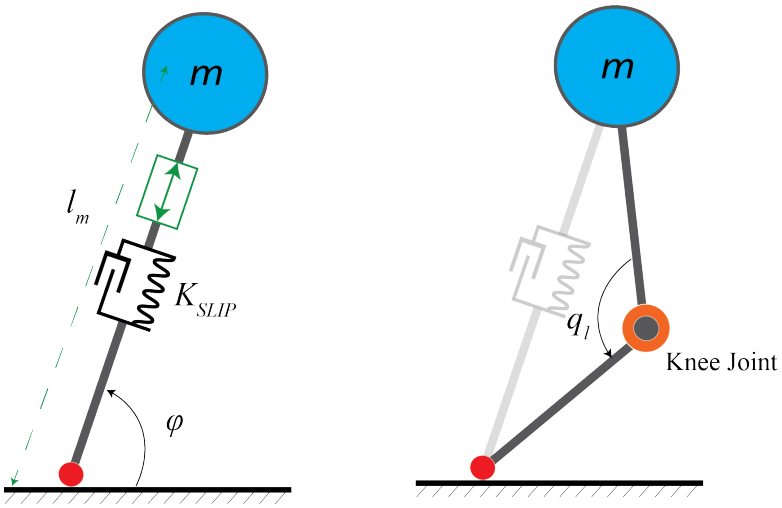


Figure 3.2: Two-DoF leg represented as a SLIP

and the tibia have the same length l. Then the length of the leg l_m can be written as a function of the knee angle.

$$l_m = 2lsin(\frac{q_l}{2}) \tag{3.35}$$

Then the jacobian that relates the generalized force of the SLIP model to the actuator space of each case studied earlier can be written as follows.

Serial:

$$\begin{bmatrix} \bar{q}_{Hs} \\ \bar{q}_{Ks} \end{bmatrix} = \underbrace{\begin{bmatrix} \frac{n}{lcos(\frac{q_l}{2})} & 0 \\ -\frac{n}{2lcos(\frac{q_l}{2})} & n \end{bmatrix}}_{A_s} \begin{bmatrix} \dot{l}_m \\ \dot{\phi} \end{bmatrix} \tag{3.36}$$

Parallel:

$$\begin{bmatrix} \bar{\dot{q}}_{Hp} \\ \bar{\dot{q}}_{Kp} \end{bmatrix} = \underbrace{\begin{bmatrix} \frac{n}{lcos(\frac{q_l}{2})} & n \\ -\frac{n}{2lcos(\frac{q_l}{2})} & n \end{bmatrix}}_{A_p} \begin{bmatrix} \dot{l}_m \\ \dot{\phi} \end{bmatrix} \tag{3.37}$$

Parallel with knee GB:

$$\begin{bmatrix} \bar{\dot{q}}_{Hs} \\ \bar{\dot{q}}_{Ks} \end{bmatrix} = \underbrace{\begin{bmatrix} \frac{2n-1}{lcos(\frac{q_l}{2})} & 1 \\ -\frac{n}{2lcos(\frac{q_l}{2})} & n \end{bmatrix}}_{A_g} \begin{bmatrix} \dot{l}_m \\ \dot{\phi} \end{bmatrix} \tag{3.38}$$

The antagonistic power in a leg model that follows the dynamics of a SLIP model can be written as follows. Where the values a_{11}, a_{12}, a_{21} and a_{22} take their values from the kinematic specific jacobians A_s, A_p and A_g in Eqs. 3.36, 3.37 and 3.38 respectively.

$$P_1 = \frac{a_{12}a_{22}}{a_{11}a_{22} - a_{21}a_{21}} Q_l \dot{\phi} \tag{3.39}$$

$$P_2 = \frac{-a_{12}a_{22}}{a_{11}a_{22} - a_{21}a_{21}} Q_l \dot{\phi} \tag{3.40}$$

The geometric power can then be written as.

$$P_s = 0; \tag{3.41}$$

$$P_p = lcos(\frac{q_l}{2})Q_l\dot{\phi}_l \tag{3.42}$$

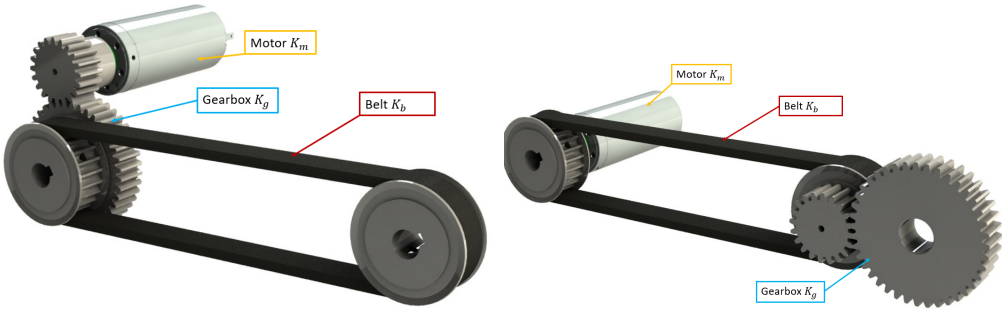
$$P_g = \frac{l}{n}cos(\frac{q_l}{2})Q_l\dot{\phi}_l \tag{3.43}$$

It is important to note that for the serial case, the geometric work is zero since there is only one actuator, in this case, the knee motor, acting in the leg length direction. Hence when the leg is following the dynamics of the SLIP model, the leg length can be held constant with no need for the knee motor to rotate. In the parallel case, the knee motor will have to be back-driven by an amount equal to the change in the angle ϕ, this can be seen in Eq. 3.33. In this relation, a change in hip motor angle, while keeping the knee motor fixed, will result in the knee joint moving with the same amount but in the opposite direction. Hence, to keep the leg length the same the knee gear-box will have to be back-driven by that same amount which will result in a non-zero geometric work. In the case of the knee GB, as seen from relation 3.34, to keep the leg length the same, the knee BLDC will have to be back-driven the same amount as the hip joint moves.

The crucial difference between the knee GB and the parallel case is in the amount of projected torque one actuator has on the other. Assume that the hip motor rotates by an angle α and the torque needed to support the length of the leg is τ. Then due to the coupling between the joints, the knee joint will rotate with an angle $-\alpha$ so to keep the length the same, the knee actuator will have to be back-driven at an angle equal to α resulting in a geometric work of $\tau\alpha$. But in the case of the knee GB, when the hip rotates with an angle α, the knee joint rotates with an angle $-\alpha/n$ which means that the knee BLDC and not the gearbox will

have to be back driven by an angle of α. Now since the BLDC torque is τ/n, to satisfy a knee joint torque of τ then the geometric work will be $\tau\alpha/n$. This is reflected in the geometric power analysis shown in Eqs. 3.42 and 3.43

3.4 Gear Train Stiffness



(a) Motor-gear-belt (b) Motor-belt-gear

Figure 3.3: The two gear-trains configurations considered for this study

Another advantage of switching the order of the gear train is to increase the perceived stiffness of the gear train. Fig. 3.3 shows the two gear-train configurations considered for this study. The first, motor-gear-belt, has a motor connected to a gear reduction with a ratio of n and then a belt with a reduction of 1. In the second case, only the order of the belt and the gears is changed.

For the motor-gear-belt configuration the stiffness, K_{mgb}, can be written as:

$$K_{mgb} = \frac{n^2 K_m K_g K_b}{(K_m + K_b)K_g + n^2 K_m K_b} \tag{3.44}$$

while the motor-belt-gear configuration stiffness, K_{mbg}, can be written as,

$$K_{mbg} = \frac{n^2 K_m K_g K_b}{(K_m + K_g)K_b + n^2 K_m K_g} \tag{3.45}$$

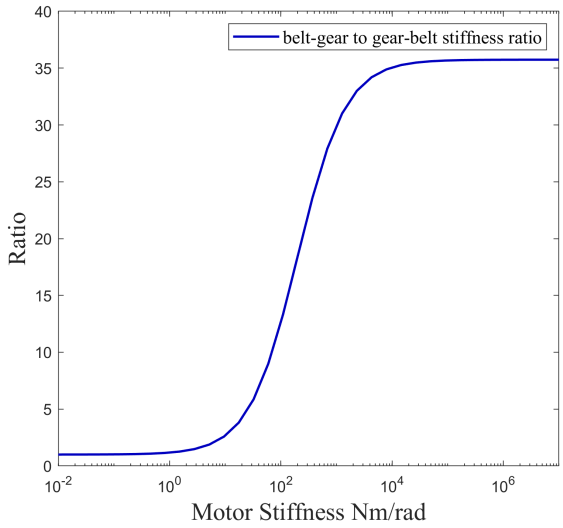


Figure 3.4: stiffness ratio between the motor-belt-gear and motor-gear-belt configurations

where the K_m, K_b, and K_g are the stiffness-es of the motor, belt, and gearbox respectively while $n = 6$ is the gearing ratio. The estimated stiffness of the gearbox is $10^7 Nm/rad$ and the average experimental stiffness of the belt used is about $200 Nm/rad$ depending on the tension in the belt. Fig. 3.4 compares the ratio between K_{mbg} and K_{mgb} as the stiffness of the motor increases. The stiffness ratio is how much the new configuration of motor-belt-gear stiffness is higher than the motor-gear-belt stiffness. It can be seen that as the stiffness of the motor increases the ratio approaches 36 asymptotically which is the square of the gearing ratio $n = 6$. If the motor stiffness is at zero, then the ratio is 1 and there is no advantage of the motor-belt-gear configuration over the motor-belt-gear configuration. The stiffness of the BLDC motor K_m depends on multiple factors including the mode of operation, control method, and physical attributes of the BLDC. Depending on the stiffness of the motor, which changes through the operation cycle, the new gearing configuration increases the stiffness of the mechanism by a factor of anywhere between 1-36 times.

3.5 Results

In this section, the new leg design is simulated in both static and dynamic cases for the stance phase of a walking gait. Experimental results are also presented that confirm the modeling of the leg and its implications.

3.5.1 Simulation Results

Static Simulation In the case where the robot is simply standing, then the torques at the actuators are only those needed to support the weight of the robot. The mass and moments of inertia of the linkages are ignored as the only factors contributing to the torques of the actuators are the external force acting on the foot in the x and y directions as well as the leg geometry. The first case considers applying a constant vertical force of 23N at the foot contact, this roughly equals the force required to support the weight in the vertical direction. The contact is assumed to occur at a frictionless surface which implies that $f_x = 0$. The kinematic equations and the jacobians in 3.20, 3.11 and 3.10 are used to evaluate the torque at the hip and knee actuators required to support the vertical force.

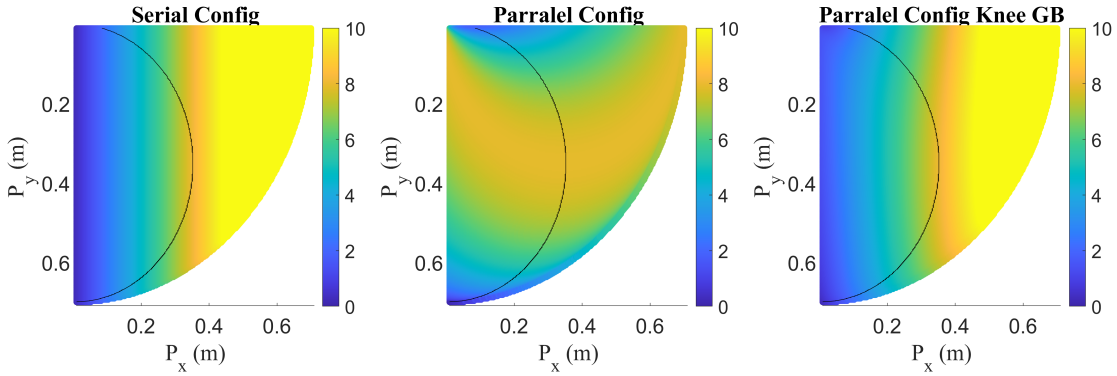


Figure 3.5: Static hip motor torque comparison

Figs. 3.5 and 3.6 show the torque power spectrum distribution of the actuators when acting on the hip and the knee joints. The torques vary with the placement of the foot away from the body which is placed at the origin. The plots show that

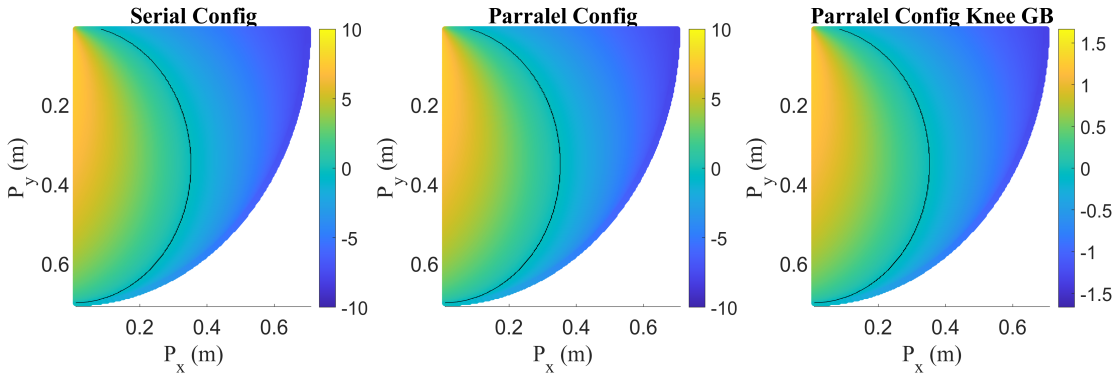


Figure 3.6: static knee motor torque comparison

different kinematic configurations carry significant implications on the amount of torque each actuator provides.

Fig. 3.6 shows the torque distribution of the knee actuators. The spectrum of the torque for all cases is the same as the kinematics do not change the torque provided by the knee actuator. However, the only notable change is the torque provided by the knee actuator for the knee GB configuration. Even though the distribution is the same as the two other configurations, the knee actuator torque for the case with the gearbox at the knee is scaled down by a factor of the knee joint gearing ratio $n = 6$. That is because the plot shows the pre-gearing torque rather than the post-gearing torque. The black line shown in the plots reflects where the knee joint torque is equal to zero. Despite tracking a semi-circle on the plot, this corresponds to the configurations where the tibia makes a perpendicular angle with the ground making the knee motor toque needed to support the knee joint zero.

For the hip motor torque, shown in 3.5 the torque distribution is significantly different in each case. The torque for the serial case shows the dependence of the actuator torque on the lateral placement of the foot. The further away the foot placement in the $x-$ direction, the higher the torque needed. If the foot is placed right under the hip joint then the hip motor torque will be zero. As for the parallel configuration, the actuators tend to fight each other in certain regions increasing

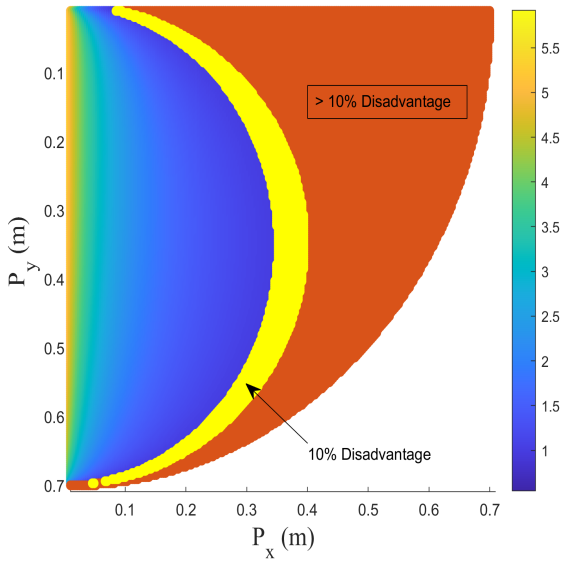


Figure 3.7: Advantage of relocating the knee motor to the knee joint

the hip motor torque needed to satisfy the hip joint torque. If the foot placement is to the left of the black line, denoting the zero knee torque, then the torque of the knee and the hip will be opposing increasing the hip motor torque required to satisfy the joint torque. If the the placement is to the right of the line, then the knee and hip will cooperate reducing the hip actuator torque needed.

As for the case of placing the gearbox at the knee, the distribution is a little bit more complicated, the actuators do fight and cooperate in the same regions as the parallel configuration; however, the amount of fighting/ cooperating torque needed is reduced by a factor of n. This pushes the mechanism into a distribution that is more similar to the serial case. These results are confirmed in the following section.

Fig. 3.7 shows a torque comparison for the hip motor needed to hold the hip joint for the parallel and the knee GB cases. When the foot placement is closer to the body the parallel configuration shows about six times higher torque than that of the knee GB configuration. The yellow boundary shows where the knee GB mechanism crosses from being advantageous to disadvantageous.

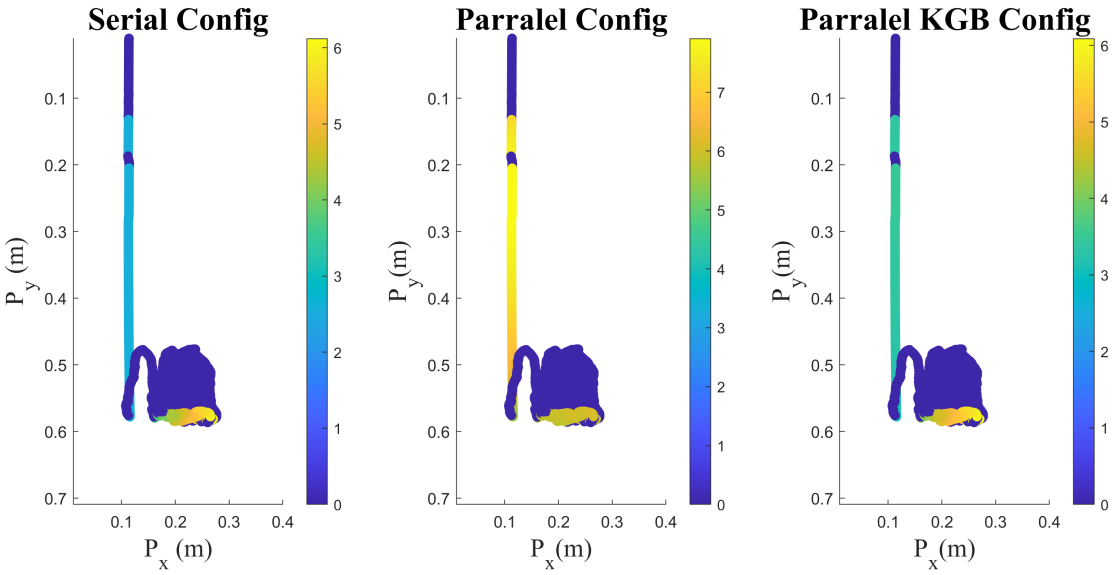
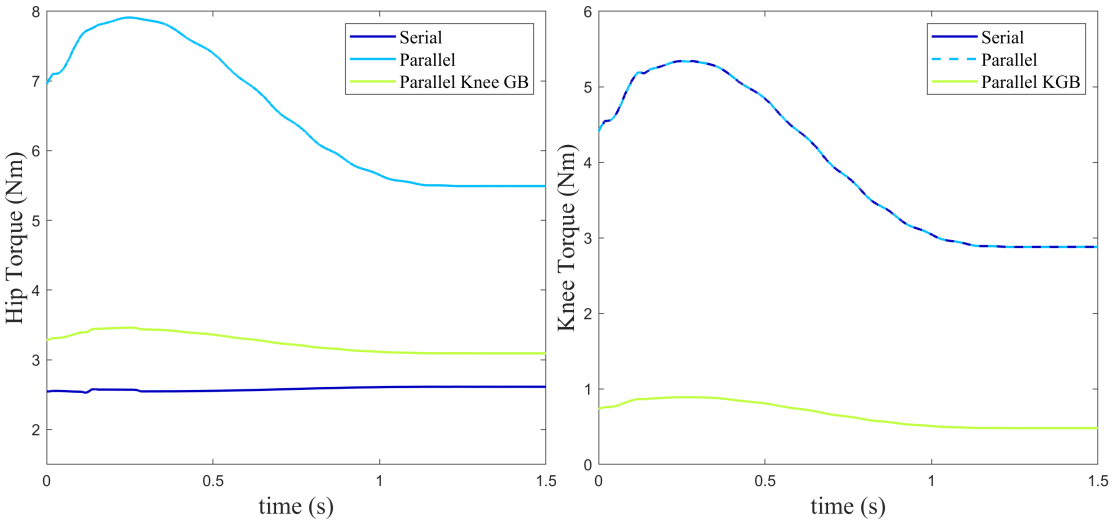


Figure 3.8: Foot location and associated hip torque for each case

The advantages of the new mechanism are also evaluated under the simulated gait of SORELL. Simulation values are obtained for a walking gait of SORELL for the angles of the leg joints and the contact forces at the foot. These values are then used to evaluate the torques needed by the actuators using the modeling presented earlier. The first simulated results are shown in Fig. 3.8. The values of P_x and P_y are obtained through forward kinematics from angle values obtained from simulation.

Fig. 3.8 shows that for most of the gait, the location of the foot contact lies in the region with an advantage to the new mechanism. It can be seen that throughout the gait, the parallel configuration has a higher hip motor torque as it resides in the regions where the parallel mechanism is at a disadvantage. The torques of the hip motor are especially high when the robot is standing up which crosses directly in the high antagonism region. To elaborate on this, if the actuators are in a region where their torques are opposing, then in a configuration where the knee joint requirement is high, the hip actuator will have to provide more torque to support the hip joint as well as counteract the torque due to the knee actuator.



(a) Hip Motor Torque (b) Knee Motor Torque

Figure 3.9: Static Hip and Knee motors torque for three cases needed to support robot weight

Fig. 3.9 shows the torques needed at each motor to stand up plotted against time. The torque needed at the hip actuator is shown in 3.9b. The torques for the knee joints are all identical, however, the one plotted for the knee GB case reflects a scaled-down torque by $n = 6$. In Fig. 3.9a, the torque needed at the hip actuator in the parallel case, is increased compared to the other two configurations as the hip motor has to counteract a much larger component of the knee joint torque to satisfy the hip joint requirement.

Dynamics simulation In the dynamic case, the effect of the kinematics can affect the power consumption of the leg in a different manner. In the previous section in the static case, the torques evaluated to hold the robot weight reflect the motor losses. Hence, if the robot is simply standing a higher torque requirement means that the losses are larger. This is crucial when the robot is standing for prolonged times such as performing manipulation tasks. However, that is not the case when the robot is in dynamic motion as there are more components at play

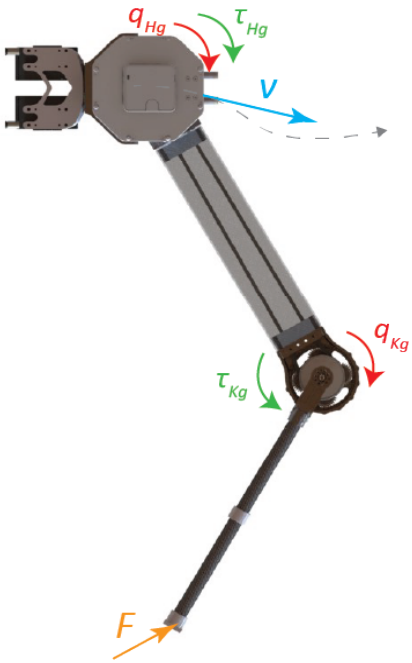


Figure 3.10: Actuator torque/ velocity direction in stance phase

here. This brings us back to the concept of geometric work.

In the case of walking or trotting, the geometric power of the robot can be written as in Eq.1.17, which denotes the differences between the total power delivered to the robot leg by the motors and the net power required by the task. In certain cases throughout the stance phase, one of the actuators might have to be back-driven, in that case, the geometric work will be non-zero. Fig. 3.10, shows that depending on the direction of travel one of the actuators will be back driven, in this case, the knee actuator.

The SORELL robot was simulated over a walking gait and the contact forces and motor angles were imported into a MATLAB simulation. That data was used along with the dynamic model of the three leg configurations. The actuator torques were plotted over a stance phase of one of the forward steps which is shown in Fig. 3.11. It can be seen that during most of the gait when there's contact with the foot, the knee GB case has lower hip actuator torque than the parallel case. The serial configuration shows lower torques at the actuators however it is

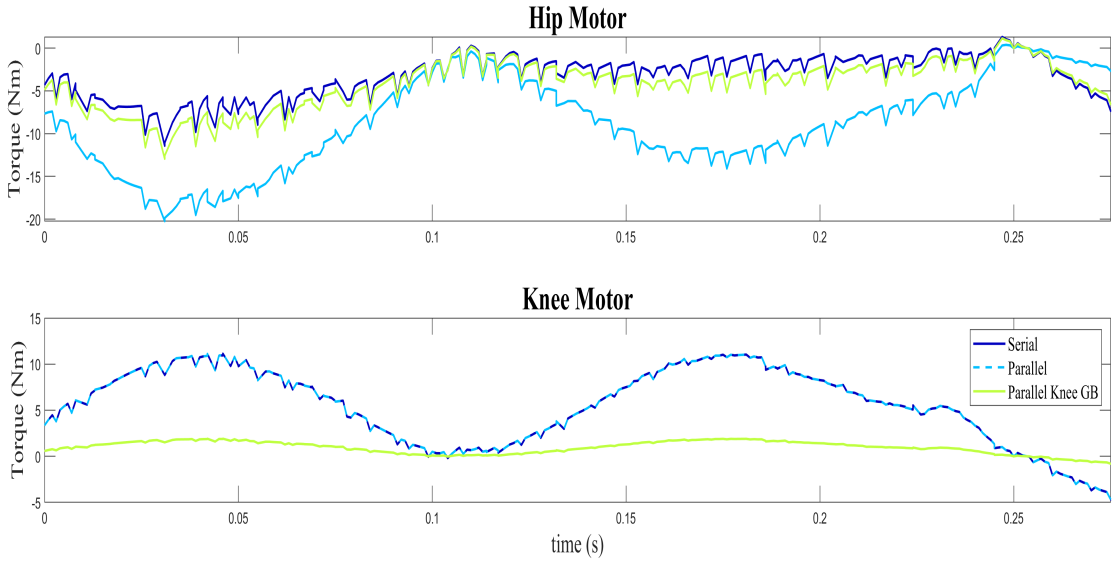


Figure 3.11: Dynamic Torques during walking gait

not as balanced as the Knee GB configuration.

It is important to note, that in the case that all actuators are working in the same direction. Then the power due to the geometric work will be zero. In that case, the net and total power will be equivalent. Fig. 3.11 shows the different torques on the hip and knee motors during the stance phase of a single step. Even though it is clear that the knee GB design has a lower torque compared to the parallel case, the power also depends on the velocities of the actuators.

To do that comparison, the powers are plotted in Fig. 3.12. In this figure, the net power is equal across all configurations which is consistent with our analysis; however, the total power shows an increased power for the parallel case as compared to the other two. This means that the new mechanism experiences lower antagonism throughout the stance phase.

3.5.2 Experimental Results

To confirm the results in this chapter, an experiment was performed to assess the torques for the knee GB configuration and to compare them to expected actuator

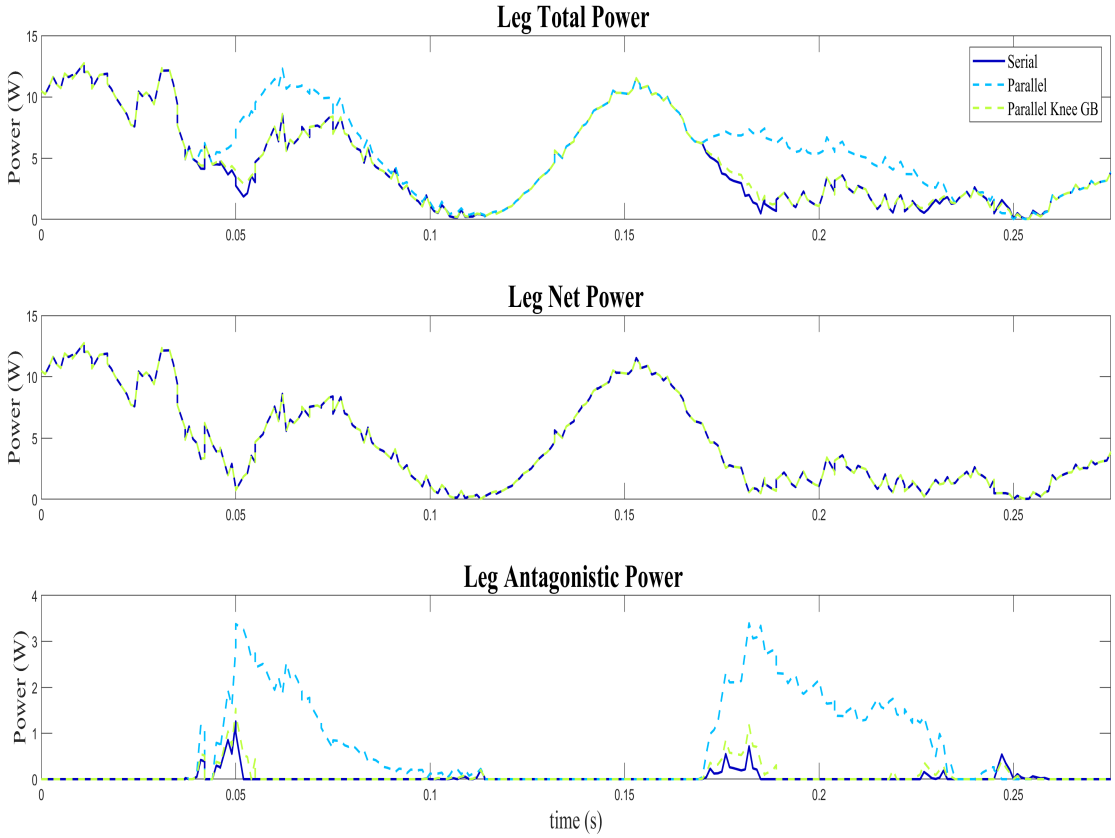


Figure 3.12: Leg powers Power in the three systems analyzed

torques for other configurations. The experimental setup is shown in 3.13.

For this experiment, the torques in the actuators are measured and estimated through motor winding currents. Due to the high transparency of proprioceptive actuators, that estimate is considered reasonable. The setup for the experiments starts with choosing the P_x and P_y for each data point. The data points span P_x = [0 10]cm and for each P_x data point the P_y spans P_y = [30 60] cm. For each data point, the torque needed to support the weight of the leg is measured. Then the leg is loaded in the Z direction and the torques due to the added load are recorded. The torques due to the added weight on top of the robot are then calculated by subtracting the two torque values. This is done to account for the varying mass distribution throughout the leg with each data point. In this experiment, the leg is made to freely slide in the $x-$ and $z-$ directions, to reduce the effect of the force

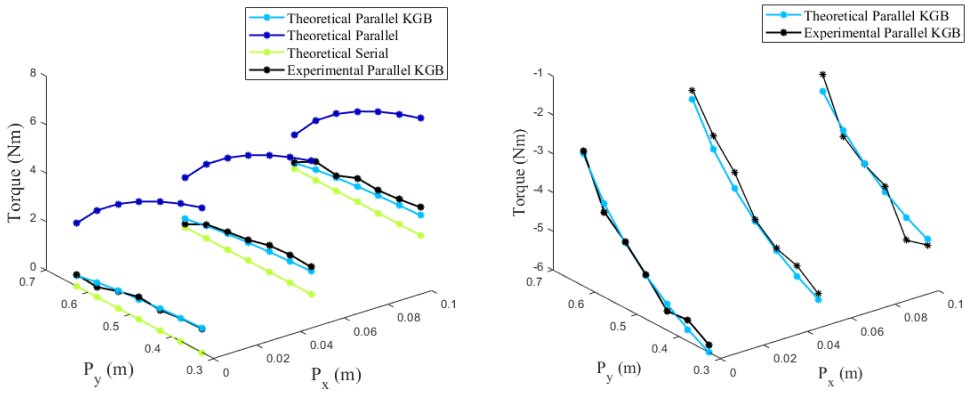


Figure 3.13: Experimental Setup for Knee GB experiment

at the foot in the $x-$ direction. Since the torques are measured at the motor side and not the gear side, the static friction had to be estimated and compensated for in each actuator.

Fig. 3.14b shows the experimental and theoretical torques at the knee joint of the knee GB configuration. In this case, the knee joint torque is reported rather than the knee motor since it is the same for all cases. For clarity, only the torque corresponding to the knee GB case is plotted, but they all coincide.

As for 3.14a, the torque reported is due to the hip actuator. The experimental results for the knee GB configuration match closely with the theoretical torque for the specified data points. It also lies well below the hip motor torque for the parallel case and slightly above the serial case.



(a) Hip motor torque

(b) Knee joint torque

Figure 3.14: Static hip and knee motors torque for three cases considered over gait

3.6 Discussion

Chapter 4 and 3 introduced a new quadruped robot SORELL that has a unique leg gearing configuration. Through modeling, simulation, and experimental results it was shown that moving the gearbox of the knee motor to the joint and changing the gearing order has multiple advantages. These include the reduced mechanical antagonism for the desired gait configurations as well as increasing the stiffness of the linkage. These outcomes are significant when utilizing proprioceptive actuators since they depend on input signals to perform force control. This improvement does not come without an engineering trade-off. Relocating the gearbox to the knee increases the flung mass which complicates the dynamics and increases the required torque needed to achieve a certain acceleration. This gearing configuration also has a more complicated assembly and manufacturing procedure compared to the ALPHRED-2 leg. SORELL's leg does not only require the customization of a new gearbox but also requires the standard parts to be altered including the actuator itself. Moreover, the assembly is complicated and requires more parts to achieve the design.

CHAPTER 4

Passive Spring Grippers

4.1 Introduction

In robotic manipulation tasks, the grippers are what directly interact with the environment. Objects and environment features can vary in their mechanical properties hence they require versatility in actuators at the gripper level [48] [45] [51]. Most commercially available grippers use stiff high-gear ratio actuators to achieve accurate position control. The position control allows for the accurate placement of the gasping mechanism with respect to the grasped object. Classically, research on mechanically compliant actuators has focused on their application to robotic joints rather than on the grippers. Recently, however, there has been growing interest in developing compliant grippers and researching their functional abilities. As summarized in Ch. 1, the property of compliance in an actuator has many benefits. Most notably, series elasticity, whose presence changes the force torque problem into a position control problem.This feature obviates the need for FT sensors while mitigating the effects of high-frequency impacts and allowing for energy storage and recycling.

To enable SORELL to perform its expected precise and safe manipulation tasks, a family SEAs and VSAs based on magnetic forces were developed to be used as grippers and end-effectors. These gripper actuators are studied separately based on their respective attributes. They are then characterized and compared. The actuators developed for SORELL manipulation are designed, built, and tested as standalone end-effectors. However, it can be shown from this research that these actuators can be combined to obtain complex and synergistic designs that achieve

more than one of the specified attributes of any single actuator. This chapter will present the designs of two magnetic SEAs, based on geometric manipulation of permanent magnets. In Ch. 5, additional actuators will be presented that expand on the ideas discussed here.

4.1.1 Gripper-Level Compliance

Similar to compliance in joints of a robotic manipulator, compliance at the end-effector also protects from unexpected impacts, stores and recycles energy, and provides a reliable way for force control. Besides these advantages, compliant gripper designs can be made to couple multiple fingers in the same end-effector reducing the number of actuators needed through under-actuated mechanisms. The coupling of fingers with compliant elements can also help the gripper take the shape of the grasped object without the need for secondary actuators. As some research has shown, having a SEA or a VSA at the end-effector, can provide some characteristics of a full SEA-based robotic manipulator even if traditional actuators are used for the rest of the manipulator [51]. This means that the versatility of the manipulator can be enhanced at a reduced cost and complexity of the system. Additionally, energy storage and explosive motion at the gripper level can be exploited to achieve fast contraction and relaxation of the fingers enabling fast grasp and release motions.

4.1.2 Non-linear Springs

The trade-off of features between soft and hard springs in SEAs discussed earlier has increased interest in progressive (stiffening) nonlinear springs. Nonlinear springs exhibit a wider force/torque range than linear springs. For instance, a nonlinear progressive spring behaves as a soft spring in small deflection regimes and as a stiff spring in higher deflection regimes. Nonlinear springs also have a higher

capacity for energy storage compared to linear springs. When compared to VSAs however, they sacrifice online tunability for a more compact design. Still, with careful design and modeling, a nonlinear spring can achieve the desired stiffnesses over the operational space. Therefore, they can be directly applied to grippers where the torque/ force is lower compared to other joints.

4.1.3 Grippers with Magnetic Compliance

Using magnets to create non-linear springs for gripper SEA and VSA applications has several intrinsic benefits. First, magnets come in a variety of sizes and strengths making them versatile and fitting to create customized configurations. Magnets also have minimal unmodeled non-linearities from friction due to their no-contact behavior, additionally making them less prone to wear and tear. Neodymium magnets, the most commonly used magnet in such applications, are also highly stable unless subjected to high temperatures. Flux losses in Nd-Fe-B magnets are minimal under low temperatures [66], and only lose about 1% of their magnetization over a ten-year period [67].

Magnetic repulsion has gained some popularity in literature as it resembles a simple positive stiffness spring. Conversely, magnetic attraction is an example of an unstable spring with negative stiffness. Although less utilized, such instability can generate a fast response on the robotic gripper or finger. Another major advantage of magnetic compliance is the availability of electromagnetic methods to change the compliance of a magnetic spring. Coils can be used to change the stiffness of the magnetic spring which, if required in the joint, adds another degree of freedom to control of a VSA. Such a way of changing stiffness has a very fast response time and does not need to fight against the primary actuator in the case the output was already deflected from equilibrium. The last added benefit that will be discussed in this work, is the use of copper tubes and surfaces to induce eddy current braking which can be modeled and incorporated into designs for

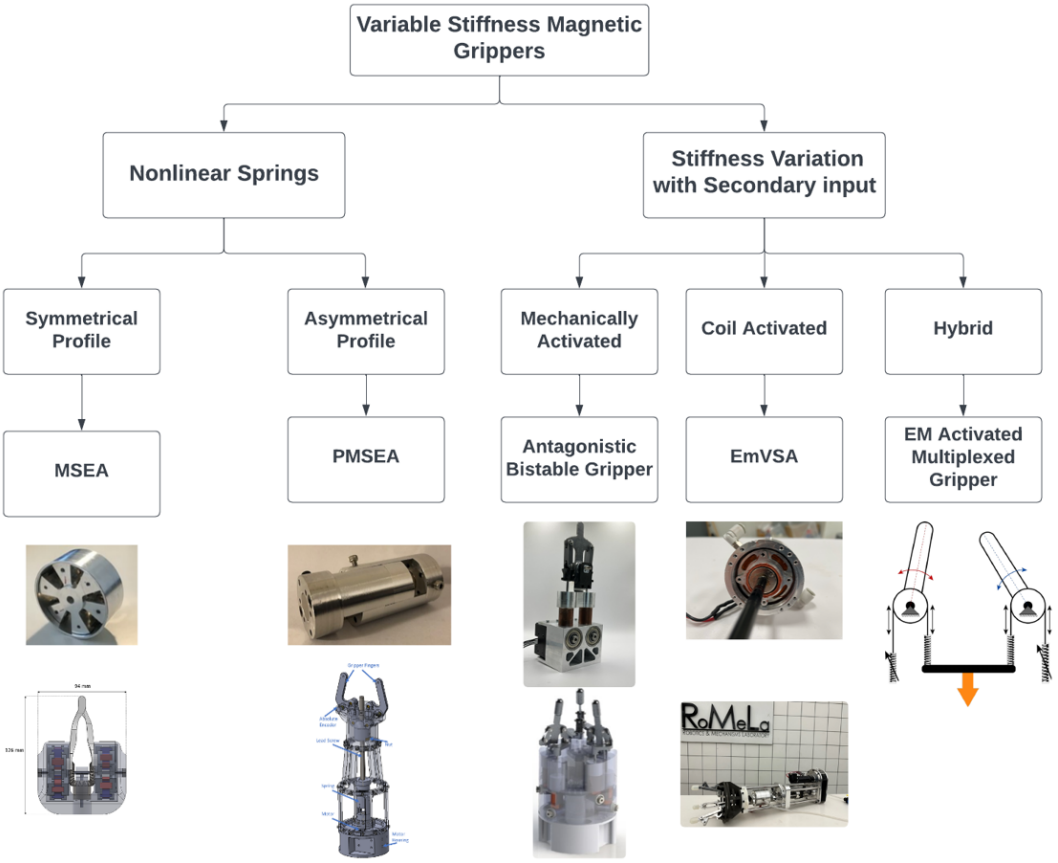


Figure 4.1: Gripper family tree

shock absorption and impact mitigation.

4.2 Passive Magnetic SEAs

The first two actuators that will be discussed, MSEA and PMSEA, use a passive variable stiffness curve that depends on permanent magnet arrangement. The first, MSEA, is a torsional spring with a symmetrical force profile while PMSEA is a linear spring with an asymmetrical profile. The other two grippers, presented in Chapter 5 use different methods to vary the physical stiffness of the system.

4.2.1 Stiffness through Magnet Arrangement

The designs presented in this section take advantage of smart designs to achieve a unique stiffness profile. As different grasping tasks might require different stiffness throughout the task, careful design of the placement of magnets in a spring can be leveraged to achieve the desired stiffness curve. Two series of elastic actuators with magnetic springs are introduced in this chapter. Both actuators use springs that are nonlinear and rely on magnet arrangement to achieve this varying stiffness feature. In the first spring presented, MSEA, the design utilizes angularly separating magnets to maximize the force profile and minimize the space requirement. The second spring, PMSEA, uses a geometric asymmetry to impart anisotropy to the stiffness profile that could be favorable in tasks requiring different profiles when compressing and extending the spring.

4.3 MSEA

The Magnetic Series Elastic Actuator (MSEA) is a rotary series elastic actuator with a magnetic spring proposed to be used with simple grippers where a secondary actuator to adjust stiffness is considered a luxury. This magnetic spring can be used in underactuated robotic grippers and fingers that do not require the control of each finger separately.

4.3.1 MSEA Design

MSEA is designed and built using two arrays of magnets that are in repulsion. The arrangements (shown in Fig. 4.2) are contained in two three-spoke structures that rotate with respect to one another. One of the structures is connected to the motor, denoted as the input structure, and the second is connected to the load side denoted as the output structure. Each structure holds six square N40 magnets that when put together each pair of magnets is in constant repulsion.

Each repelling pair of magnets represents a virtual spring, and the combined stiffness of the whole spring is denoted as $K_s(\theta_s)$, where θ_s is the deflection angle formed between the input and output array spokes. The overall effect is a rotary magnetic spring with a unique configuration that has a pre-loaded stiffness that depends on the placement angle, θ, between the two magnets. Table 4.1 summarizes the attributes of the whole magnetic spring assembly while 4.2 includes the parameters of the magnets used in this spring.

Table 4.1: Assembly magnetic spring characteristics © 2021 IEEE

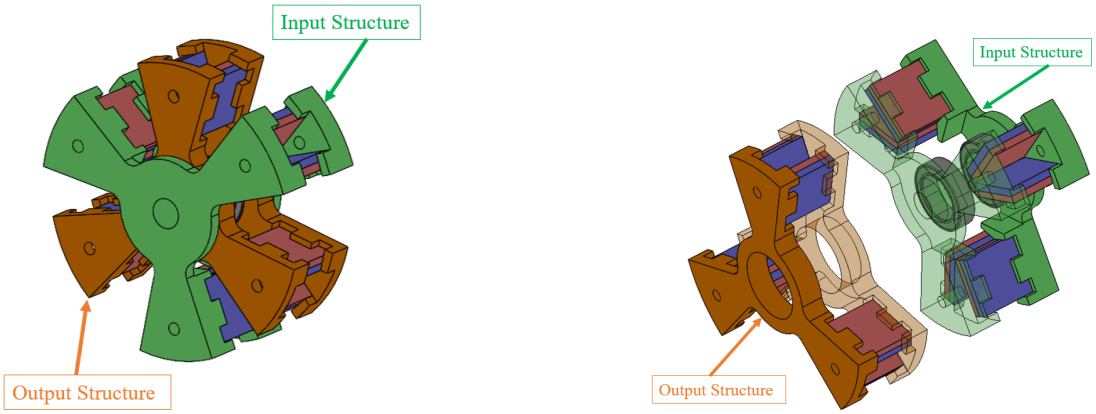
Spring parameter	Value
$Weight$	$160g$
$Radius$	$31.75mm(1.25in)$
$Number\ of\ Magnets$	12

Table 4.2: Single magnet parameters © 2021 IEEE

Magnet parameter	Value
$Magnet\ size$	$12.7mm \times 12.7mm \times 3.175mm$
$Magnet\ Grade$	$N40$

The magnets in the output and input structures follow a progressive angle configuration. This means that considering two magnets in repulsion, the magnets move in an angular fashion. This angular separation increases the stiffness range as opposed to linear separation. The three-spoke structure is designed and manufactured such that the magnets are separated at an angle, however, when the spring saturates, the magnets become perfectly parallel. The closest the magnets get to each other is shown in Fig. 4.4 as $2d = 0.1in$. Compared to parallel separation, angled separation gives a larger force range for a more compact space.

In FEM simulation, the force is plotted against the distance between the lower edge between the magnet pair, which are S_{Par} and S_{Ang} as shown in Fig. 4.4.



(a) MSEA spring assembly CAD

(b) MSEA assembly CAD exploded view

Figure 4.2: MSEA nonlinear rotary magnetic spring design © 2021 IEEE

In Fig. 4.5, it can be seen that the force starts at the same maximum value for both configurations, however, the angled configuration decays faster and yields a wider force range as a result. This difference occurs because when the angle between a pair of magnets widens, the tilt in the magnetization vector further reduces the force between the pair of magnets faster than that of the parallel configuration, which in turn yields a larger difference in force compared to the parallel configuration. This configuration exploits magnet arrangement to increase the nonlinearity of the stiffness profile while keeping the spring compact for use on robotic grippers [45] © 2021 IEEE.

4.3.2 MSEA Modeling

To analytically model the spring a dipole model was used, which treats all magnets as small magnetic dipoles. The magnetization vectors of these dipoles are in the direction perpendicular to the original magnets' surfaces. Since the magnets move at an angle an approximation model was employed that captures the change in angle of the magnetization vector as shown in [68].

In this model, a single pair of repelling magnets in MSEA is replaced with

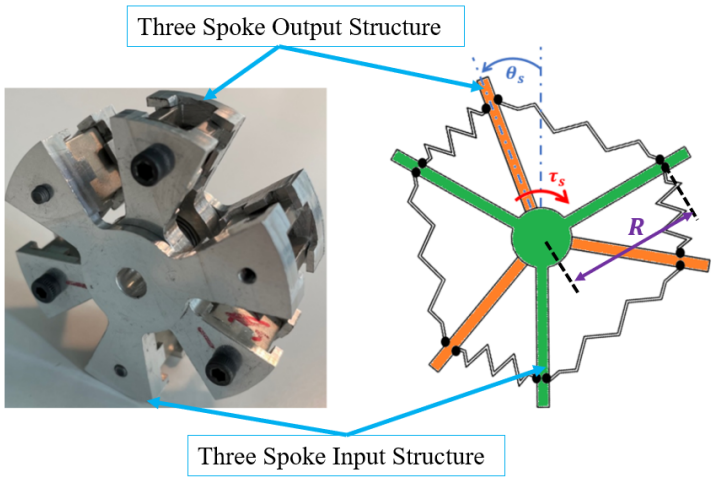


Figure 4.3: Virtual springs formed by input and output arrays of magnets © 2021 IEEE

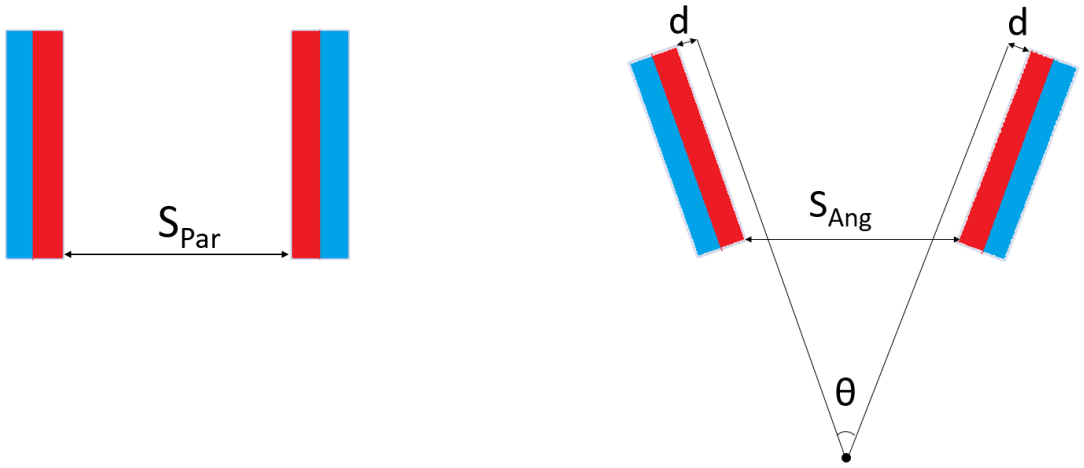
magnetic dipoles as shown in Fig. 4.6b, then the force on the first magnet by the second magnet can be written as Eq. 4.1, where $\vec{m}_1$ and $\vec{m}_2$ are the magnetization vectors of each magnet, $\vec{r}$ is the relative position vector connecting both dipoles, $\hat{r}$ is the unit vector in direction of $\vec{r}$ and μ_0 is the permeability of free space that has a value of $4\pi \times 10^{-6}\ H/m$.

$$\begin{aligned}\vec{F}_{12} = \frac{3\mu_0}{4\pi r^4}(\vec{m}_2(\vec{m}_1 \cdot \hat{r}) + \vec{m}_1(\vec{m}_2 \cdot \hat{r}) \\ +\hat{r}(\vec{m}_2 \cdot \hat{m}_1) - 5\hat{r}(\vec{m}_1 \cdot \hat{r})(\vec{m}_2 \cdot \hat{r}))\end{aligned} \tag{4.1}$$

$$\begin{aligned}F_{12}(r, \alpha, \beta) = \frac{-3\mu_0 m_1 m_2}{\pi r^4}[5cos(\alpha)cos^2(\beta) \\ -2cos(\beta)cos(\beta - \alpha) - cos(\alpha)]\end{aligned} \tag{4.2}$$

α, β and r are as shown in Fig. 4.6b.

Then the resultant force perpendicular to one of the magnets can be rewritten as shown in Eq. 4.2. Note that the force parallel to the surface of the magnet as



(a) Parallel configuration (b) Angled configuration

Figure 4.4: Parallel Vs. angled configuration

well as the torque are ignored since the magnets are constrained in those directions.

The magnitude of the force on magnet 1 by magnet 2 can then be written as in Eq. 4.4. Where F_{12} is a function of the separation angle between the magnets, θ, and the magnitude of their separation distance, r.

$$\alpha = \frac{\theta}{2}, \quad \beta = 180° - \frac{\theta}{2} \tag{4.3}$$

$$F_{12}(r,\theta) = \frac{-3\mu_0 m_1 m_2}{8\pi r^4} cos(\frac{\theta}{2})[3 + cos(\theta)] \tag{4.4}$$

Now considering the whole magnetic spring configuration, consisting of size repelling pairs, with θ_s as the angle of deflection with a range of [-26°,26°], the total torque due to the deflection of the spring is given by

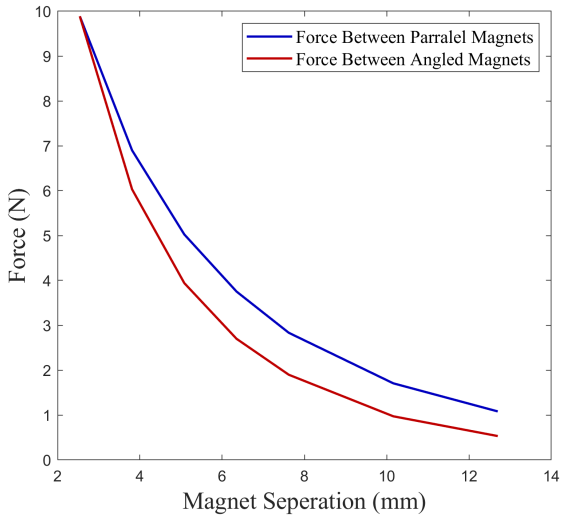
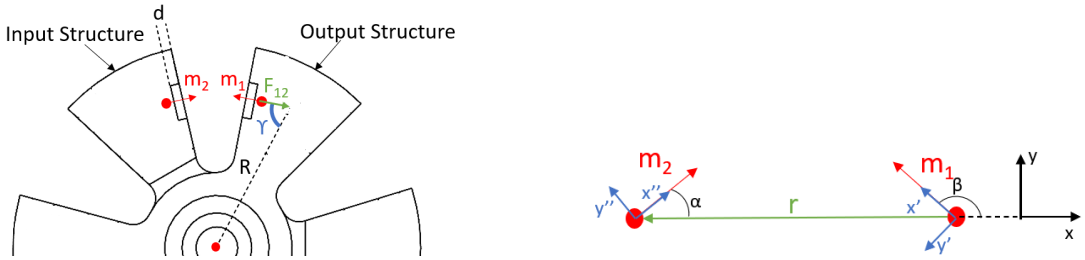


Figure 4.5: Parallel vs. angled configuration force simulation © 2021 IEEE



(a) Dipole magnet representation.

(b) Spring simplified representation

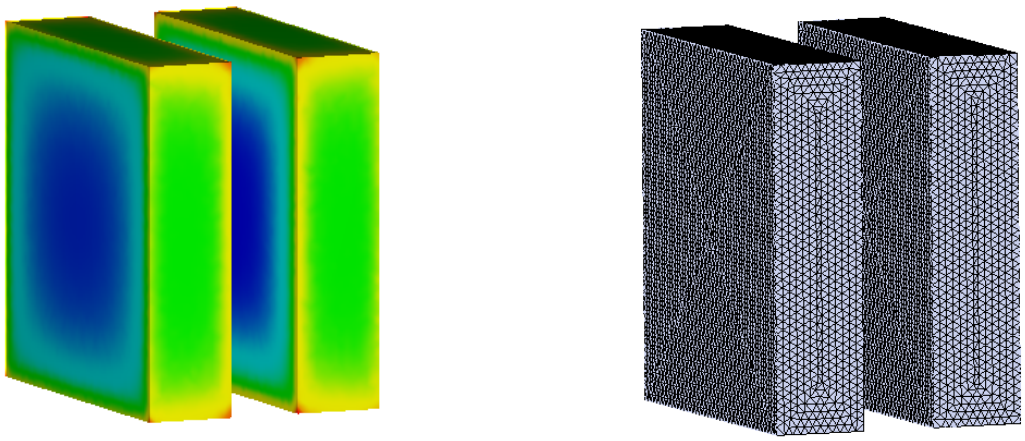
Figure 4.6: MSEA magnetic spring design © 2021 IEEE

$$\tau_S' = 3Rsin(\gamma)[F_{12}(26^\circ - \theta_s) - F_{12}(26^\circ + \theta_s)] \tag{4.5}$$

where τ_S' denotes the theoretical torque in the magnetic spring and γ is the angle between the vector parallel to the magnetization vector and R is the effective arm length shown in Fig. 4.6a. For simplicity, this model considers each pair of magnets facing each other as an isolated spring and ignores any cross effects between the pairs.

To get a more accurate model of the spring, an FEM simulation is created

using EMWorks' EMS [69] software package for electromagnetic simulation. Fig. 4.7 shows a sample simulation result as well as a meshing for two magnets of MSEA that are at their minimum separation of 0.1in. The meshing elements for the magnets are set to 0.29mm. In this simulation, the force perpendicular to the magnets' surfaces is retrieved as a function of separation to create the spring's stiffness profile model.



(a) Magnetic field intensity in EMS

(b) Mesh model of two agents at saturation

Figure 4.7: A single pair of MSEA magnets in EMS

Finally, a third model was derived experimentally using a high impedance set-up shown in Fig. 4.11. For this test, an FT sensor is mounted between the ground and the output of the magnetic spring. Then the force is measured for varying deflections in the spring.

The three models obtained are plotted over the range of the spring in Fig. 4.8. It is clear that the dipole model shown here is inaccurate compared to the experimental and simulated force curves. This difference is due to the fact that the dipole model does not take into account the surface area and the thickness of the magnets. The simulated model, however, shows a better model for the spring when compared to the experimental data. This makes such models helpful for the

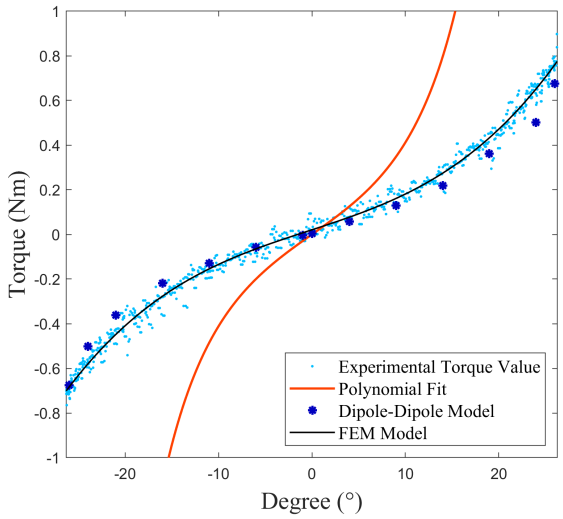


Figure 4.8: MSEA theoretical vs. simulated vs. experimental torque profile © 2021 IEEE

future development of controllers for such actuators. It is important to note that a more accurate model using EMS can be achieved through a finer discretization of the mesh.

Using the experimental data obtained, shown in blue data points in Fig. 4.8, a 3rd order polynomial using Matlab curve fitting toolbox was obtained. This model will later be used for controller purposes as it is the most accurate representation of the physical spring's model [45] © 2021 IEEE.

$$\tau_s = p_1\theta_s^3 + p_2\theta_s^2 + p_3\theta_s + p_4 \tag{4.6}$$

$$K_s = 3p_1\theta_s^2 + 2p_2\theta_s + p_3 \tag{4.7}$$

Eq. 4.6 shows the polynomial fit of the spring force-displacement curve. Where τ_s is the experimental torque value in the spring. It is worth noting that P_4, which is the scalar in the fitted force curve, is non-zero despite the fact that the spring was designed to be symmetrical and at equilibrium under zero deflection. This can be

attributed to magnet imperfections as well as machining and measurement errors. The direct derivative of the force is also shown in Eq. 4.7 which represents the stiffness-displacment curve of the spring and plotted in Fig. 4.9. The coefficients of the polynomial, representing the force and stiffness profiles, are listed in Table 4.3.

Table 4.3: MSEA polynomial coefficients © 2021 IEEE

Coefficient	Value
p_1	2.085×10^{-5}
p_2	2.576×10^{-5}
p_3	0.01367
p_4	0.02068

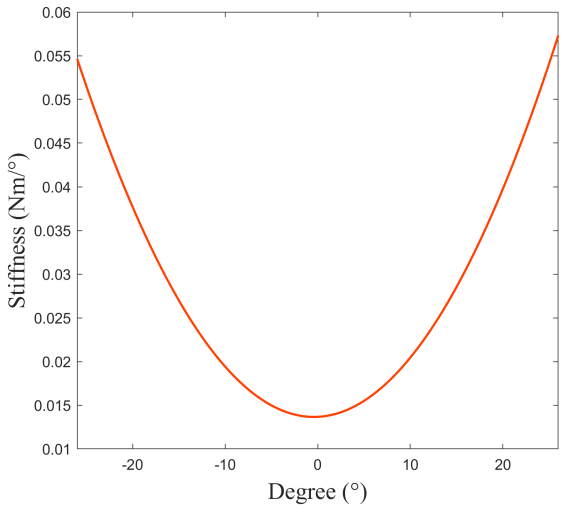


Figure 4.9: MSEA stiffness profile as a function of angular separation © 2021 IEEE

4.3.3 Controller

The controller used for MSEA is a simple gain schedule controller proposed in [70] [38], where both the inertia and damping forces are ignored. The actuator is also assumed an ideal velocity source. The controller assumes a gain schedule that

uses a function of the estimated instantaneous stiffness of the spring as shown in [70]. A block diagram of the controller used is shown in 4.10. This controller uses the model of the spring from the previous section as well as position control to achieve an accurate force controller [45] © 2021 IEEE.

The error between the estimated torque and the desired torque can be written as:

$$e(t) = \tau_d - \tau_l \tag{4.8}$$

This can be transformed in terms of the position values of the load and the motor side angles θ_l and θ_m respectively, and the instantaneous stiffness of the spring K_s.

$$e = K_s d\theta_s = K_s d(\theta_m - \theta_l) \tag{4.9}$$

The motor input can then be written as follows in terms of the current gains and the error.

$$u = K_p e(t) + K_i \int_0^t e(t)dt + K_d \frac{\mathrm{d}e(t)}{\mathrm{d}t} \tag{4.10}$$

Where the gains in Eq. 4.10 are written as in Eq. 4.11 which are the instantaneous gains that are varied based on the instantaneous stiffness of the spring that is estimated through the measured deflection of the spring.

$$K_p(\theta_s) = \frac{K_{po}}{K_\theta}, \quad K_i(\theta_s) = \frac{K_{io}}{K_\theta}, \quad K_d(\theta_s) = \frac{K_{do}}{K_\theta} \tag{4.11}$$

Gain scheduling is considered a practical and powerful method for the control of nonlinear systems since it exploits linear control design methods that are theoretically mature and computationally efficient [71]. Further, since the controller gains are adjusted to reflect the plant operating conditions, the gain-scheduling method has the potential of responding rapidly to varying operating conditions and is proven sound by successful applications throughout industry [71]. One downside of the gain-scheduling approach is that it can guarantee closed-loop stability and performance only in a local sense since it is a simple extension of linear design methods. Thus, stability and performance properties of the gain-scheduled designs must be inferred from extensive simulation studies and heuristic methods [71] [72] [73]. It is worth mentioning that any discontinuities in gain values can cause chatter in the response and excite unmodeled dynamics which can degrade performance and possibly destabilize the response [74] [75]. Hence, using a continuously varying gain scheduling method can get around some of these shortcomings [45] © 2021 IEEE.

4.3.4 Results

4.3.4.1 Force tracking

To assess the ability of the actuator to track a constant and variable torque, a high impedance test set-up is used as shown in Fig. 4.11. The actuator used for this test is a quasi-direct drive (QDD) actuator (Koala Bear, Westwood Robotics) [65]. The Koala BEAR is a BLDC motor with a $K_v = 380$ (K_v represents the speed at which the motor rotates for every volt applied) and a gear reduction ratio of

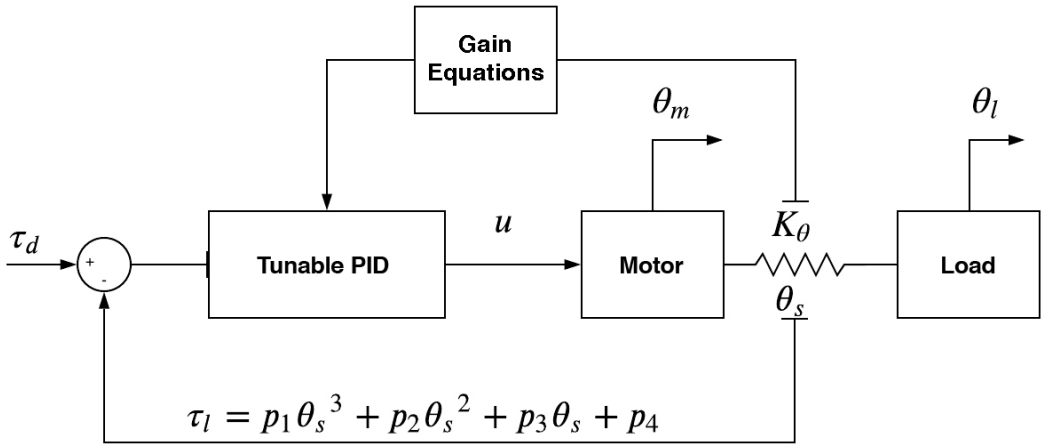


Figure 4.10: Gain-scheduled force controller © 2021 IEEE

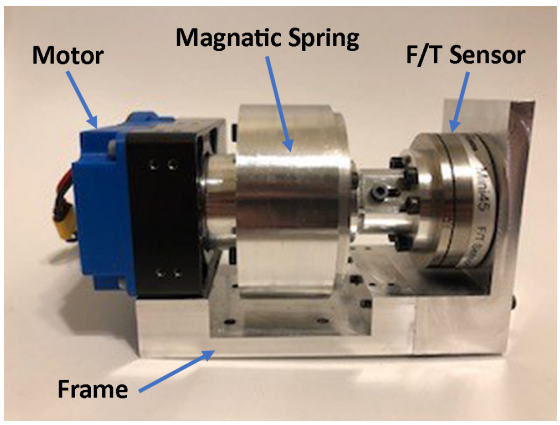


Figure 4.11: MSEA high impedance test setting © 2021 IEEE

24:1 with a 14-bit angular magnetic encoder on its output shaft. An FT sensor is used to measure and validate the ability of the actuator to track torque step and variable torque references.

Fig. 4.12 shows the torque tracking experiments performed on MSEA. The force value shown in green is the direct measurement of the force used to verify the ability of the MSEA to track both step and variable force responses. Fig. 4.12 can estimate the force in the spring based on the fit polynomial shown in Equation 4.6 [45] © 2021 IEEE.

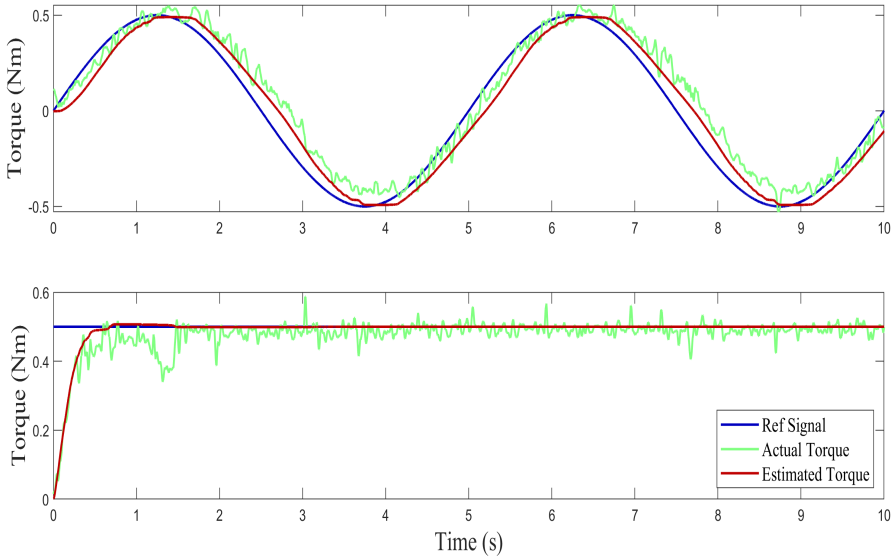


Figure 4.12: MSEA sinusoidal (top) and step response (bottom) force tracking

4.3.4.2 Bandwidth

Dynamic tests were also performed to evaluate the bandwidth of the actuator as well as the stability of the system under bounded input. The high impedance setting, or locked output is shown in Fig. 4.11. A sine sweep was performed over a set of desired torque references with both high and low amplitudes. The closed-loop torque bandwidth of the actuator was determined to be 8.0Hz and 1.6Hz for low and high amplitude references respectively.

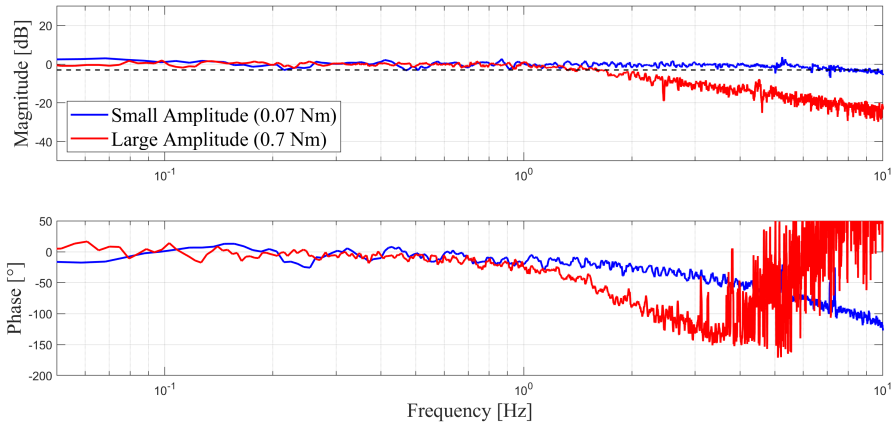


Figure 4.13: Bandwidth of MSEA

4.3.4.3 Shock absorption and impact mitigation

An important aspect of an SEA design is its ability to dissipate and store energy. To evaluate the capacity of the MSEA to absorb shocks, the impedance test setup was modified to include an arm.

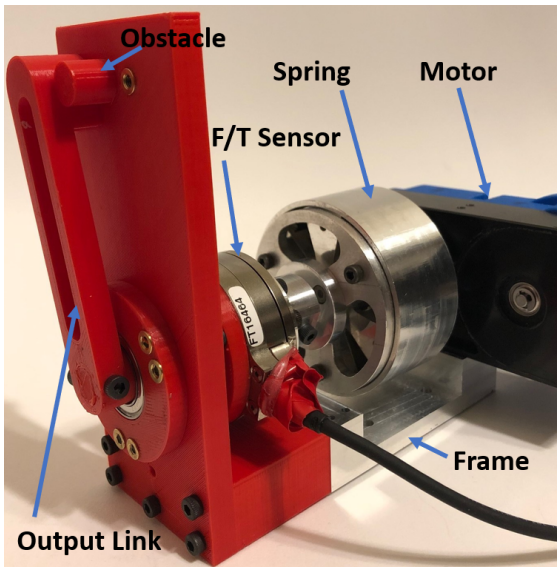


Figure 4.14: MSEA impact test set-up © 2021 IEEE

Fig. 4.14 shows the MSEA with the FT sensor connected in series to an FT sensor and then an output link. The output link was 3D printed to represent a robotic finger. The first test performed was a free response test where the motor was held at a fixed position and the output link was deflected to spring saturation and then released, the force in the FT sensor was measured and recorded. Fig. 4.15 (Top) the link can return to equilibrium in about 0.2s and shows little to no overshoot. For the second test, an impact was simulated with an obstacle, where a current value was commanded on the actuators. The actuator would then drive the output link and hit the obstacle until the commanded current is reached. The sensor reading is shown in 4.15 (bottom), the impact results in less than 20% overshoot and decays rapidly after that. Due to the nonlinearity of the spring, the torque in the spring quickly decayed. That is because a nonlinear spring has

a higher capacity to store energy.

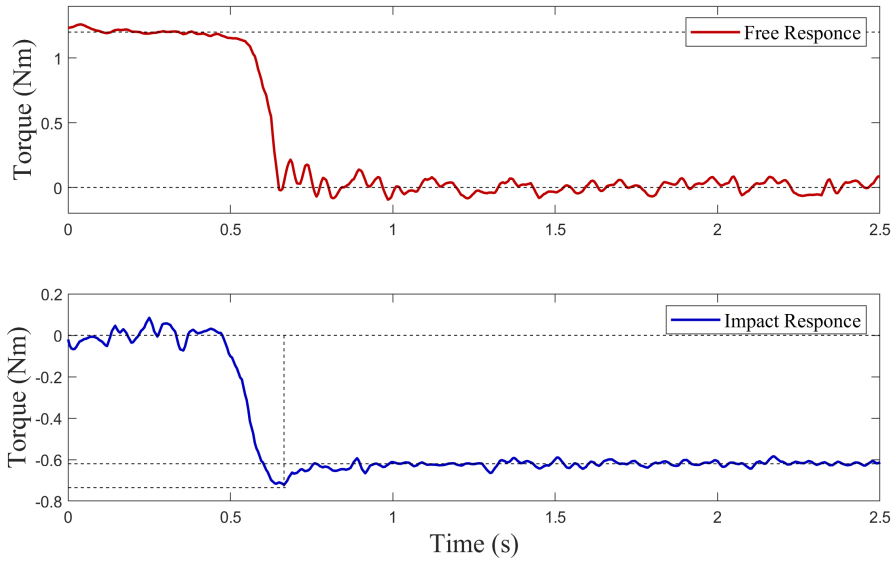


Figure 4.15: MSEA free response and impact response tests

4.3.5 Applications

This magnetic series elastic actuator was designed for simple and under-actuated grippers. A simple CAD model of such a gripper is shown in 4.16. This gripper uses one input to a single bevel gear, torque is then transmitted to the fingers through a differential mechanism. The under-actuated mechanism along with the nonlinear springs at each finger give this gripper the ability to grasp objects and adapt to their shapes. The gripper itself along with the spring can be 3D printed to satisfy weight requirements. This is seen to be simpler than other end-effectors that employ active variable stiffness mechanisms. The torque range of the spring can be increased depending on the application requirements scene and discussed in [76]. MSEA-based grippers are very desirable on a robot such as SORELL if the intended tasks are simple. Even though the MSEA gripper was shown with only two fingers, adding multiple DoFs is possible at the expense of the mechanism's complexity.

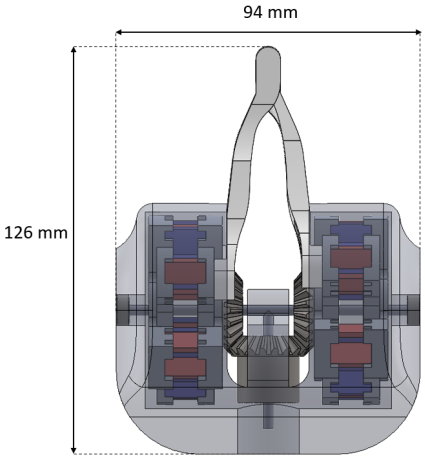


Figure 4.16: Prototype of MSEA underactuated gripper © 2021 IEEE

4.4 PMSEA

The Prismatic Magnetic Series Elastic actuator, PMSEA, is another actuator developed through the smart arrangement of magnets. As discussed earlier, nonlinear springs can be very desirable. However, in certain cases such as with human muscles, stiffness can vary with the degree of deflection as well as the direction. certain joints might require different stiffness profiles depending on the direction of deflection. It has been shown that the torque-angle relationship of a human knee during gait cycles is notably composed of a combination of both linear and nonlinear profiles [77] [78] [79]. Throughout the phases of the human gait cycle, the initial swing states are shown to have a distinctive nonlinear profile while others are predominantly linear.

However, the development of the robotic hardware that allows researchers to program the asymmetric and multi-stable nature of the skeletal muscles, despite the numerous benefits present, seems to be a remote possibility in real-world applications, considering the current state-of-the-art of robotic technologies [80]. PMSEA is an actuator that embeds various torque profiles on robotic hardware and structures. In other words, it combines the nonlinear profile of a magnetic

spring with a 3-dimensional nonlinear manifold generated by the gripper structure to warp the original stiffness profile. This process is tunable by changing the parameters of the mechanism which depends on the task at hand.

4.4.1 PMSEA Design

The design of an asymmetric nonlinear profile is composed of two phases. In the first phase, the asymmetric magnetic spring with a nonlinear torque profile that can be implanted in prismatic actuators was designed. In the second phase, a simple robotic gripper that is aimed to alter the non-linearity was designed and combined with the magnetic spring.

The magnetic spring in PMSEA, shown in Fig. 4.17, has four magnets where each pair of adjacent magnets is in repulsion. Two of the magnets the, first and third from the top, are connected in one structure and the second and fourth magnets are as well. Both structures can slide freely with respect to each other. This geometry is such that when the spring is compressed two pairs of magnets get engaged, but when extended only one pair is engaged. This creates an asymmetrical force profile that is tilted towards one direction. Fig. 4.18 shows the manufactured magnetic spring discussed in this section. Note that the spring in rotation acts as a rigid body and can only be deflected in the axial direction.

4.4.2 PMSEA Spring Modeling

As with the previous section on MSEA, PMSEA is also modeled in the same three methods. First, the dipole model is applied by assuming the magnets are point dipoles. Second, the Spring was simulated in EMWorks' EMS software and finally through experiments. The three models are plotted in Fig. 4.19, which shows that the dipole model is a very extreme misrepresentation of the model. In this case, the magnets are thicker than the ones used in the MSEA and hence such a

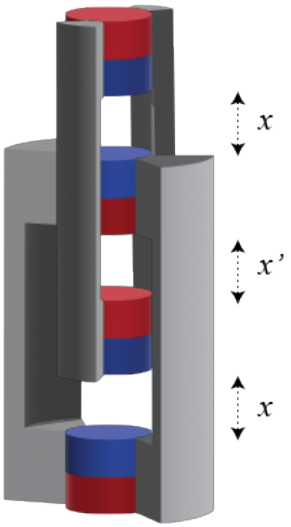


Figure 4.17: PMSEA magnetic spring diagram



Figure 4.18: PMSEA magnetic spring

method is not appropriate for modeling. On the other hand, the simulation result is a better approximation of the spring model when compared to the experimental data. In all cases, the asymmetry in the force profile is evident, and the spring has a larger range in the compression direction (negative deflection) than in the extension direction (positive deflection).

The force-displacement relationship used in the later section for PMSEA is based on the experimental model and is approximated with a 6^{th} order polynomial shown in Eq. 4.12. The stiffness profile equation is also derived through direct differentiation of Eq. 4.12 and shown in Eq. 4.13. The stiffness profile is plotted

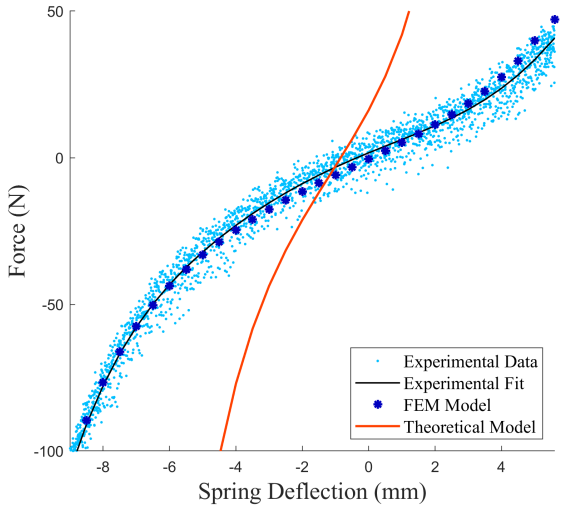


Figure 4.19: PMSEA: theoretical vs. simulated vs. experimental torque profile

for the range of the spring in Fig. 4.20.

$$F_s = p_1x^6 + p_2x^5 + p_3x^4 + p_4x^3 + p_5x^2 + p_6x + p_7 \tag{4.12}$$

$$K_s = 6p_1x^5 + 5p_2x^4 + 4p_3x^3 + 3p_4x^2 + 2p_5x + p_6 \tag{4.13}$$

The coefficients in Eqs. 4.124.13 take the values shown in table 4.4.

4.4.3 PMSEA Gripper Modeling

A two-finger gripper was designed to utilize the unique features of the magnetic spring shown in 4.21b. The annotated parameters of the mechanism take the values shown in table 4.5. The whole hand mechanism of PMSEA consists of a motor that rotates the magnetic spring chassis which has a lead screw attached to its output end. The lead screw drives an ACME nut that pushes on a linkage

Table 4.4: PMSEA polynomial coefficients

Coefficient	Value
p_1	-7.870×10^{13}
p_2	4.417×10^{12}
p_3	-9.5×10^{10}
p_4	1.062×10^{9}
p_5	-7.154×10^{6}
p_6	3.535×10^{4}
p_7	-106.9

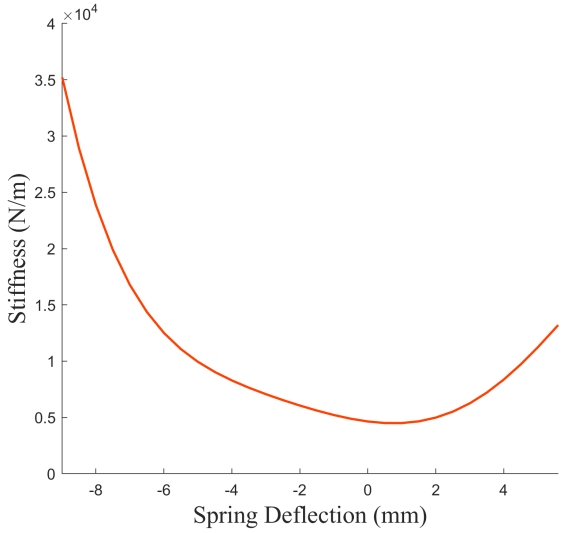
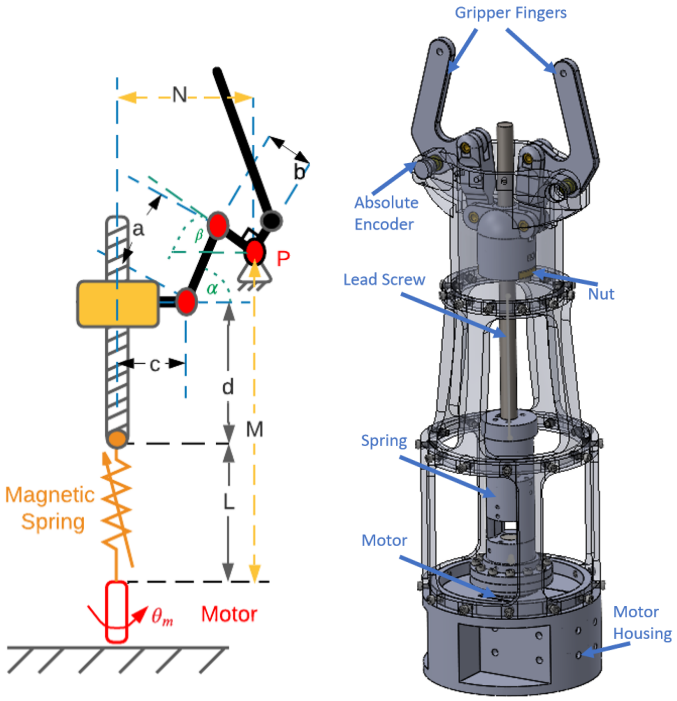


Figure 4.20: Stiffness profile of PMSEA

system consisting of two linkages. When the motor is held at a constant position, the whole lead screw assembly can be back-driven from the fingers. That's due to the lead screw's non-back drivability which allows little torque to be reflected to the motor in case of a force on the fingers.

The stiffness of the fingers about the pivot point P in Fig. 4.21b will not match that of the spring profile. Besides it being a revolute joint, the design of this mechanism allows for a nonlinear deflection of the spring. This nonlinearity in the deflection of the spring creates a manifold that is dependent on the position of the nut at equilibrium d as well as the deflection of the finger itself β. Hence,



(a) PMSEA Diagram (b) PMSEA CAD

Figure 4.21: PMSEA gripper prototype design

at each unique position of the finger, the finger will have a unique force curve.

To derive the torque at the finger, the concept of virtual work was applied. The torque at the gripper pivot point P, τ, can be expressed as in Eq.4.14, where F_s is the experimentally determined magnetic spring force Eq. 4.12, L is the length of the magnetic spring, and β is the angle the finger makes around the pivot P.

$$\tau = F_s \frac{\partial L}{\partial \beta} \tag{4.14}$$

The length of the spring can be written as,

Table 4.5: PMSEA gripper parameters

Parameter	Value (mm)
a	45
b	30
c	18
M	183
N	48
L_0	75

$$L(x) = L_0 + x \tag{4.15}$$

Where L_0 is the length of the spring at maximum compression which is constant. Then based on Eq. 4.15, ∂L and ∂x are equal as in Eq. 4.16.

$$\partial L = \partial x \tag{4.16}$$

In addition, the following relationships can be derived directly from Fig. 4.21a.

$$M = L + d + asin(\alpha) - bsin(\beta) \tag{4.17}$$

$$N = c + acos(\alpha) + bcos(\beta) \tag{4.18}$$

Lastly, the distance between the ACME nut and the top of the spring can be expressed as a function of the pitch on the lead screw, l, which equals 2 mm, and the motor angle, θ_m, as in (4.19).

$$d = \theta_m l \tag{4.19}$$

By differentiating Eqs. 4.17 and 4.18 with respect to the angles α and β, the following can be written:

$$\partial x + acos(\alpha)\partial\alpha + bcos(\beta)\partial\beta = 0 \tag{4.20}$$

$$-asin(\alpha)\partial\alpha - bsin(\beta)\partial\beta = 0 \tag{4.21}$$

By combining Eqs. 4.20 and 4.21 the partial derivative ∂x can be written as:

$$\partial x = b[\frac{sin(\beta)}{tan(\alpha)} + cos(\beta)]\partial\beta \tag{4.22}$$

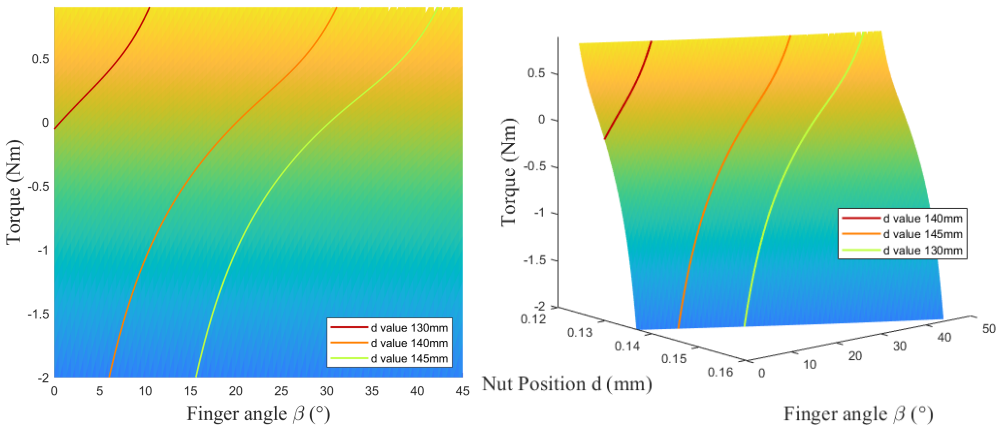
Further, by merging Eqs. 4.14 and 4.22, the torque as a function of linkage parameters and the force profile of the magnetic spring is shown as:

$$\tau = F_s(x)[\frac{sin(\beta)}{tan(\alpha)} + cos(\beta)]b \tag{4.23}$$

Note that α and x in (4.23) can also be expressed in terms of β using Eqs. 4.15, 4.17 and 4.18. The torsional stiffness value at the finger can then be calculated as a function of β.

$$K_f(\beta) = \frac{\partial \tau_f(\beta)}{\partial \beta} \tag{4.24}$$

Eq. 4.23 shows that the mechanism itself compresses and extends the spring in a nonlinear fashion. That depends on the parameters of the mechanism as well as the current position of the finger. Fig 4.22 shows the mechanism 3D manifold with the stiffness profile of the magnetic spring projected on it for three unique equilibrium positions of the finger. The manifold of the mechanism warps the stiffness profile and has the effect of making one side of the spring stiffer and the other side softer.



(a) Projected view of torque profiles (b) 3D view of torque profiles

Figure 4.22: Mechanism manifold with projected stiffness profiles for different finger equilibrium positions

The projection of nonlinear profiles on a 3D manifold generated through a linkage increases the range of achievable stiffness profiles. Warping stiffness profile asymmetrically could be useful in instances where a different profile is desired for extension vs. compression.

4.5 Discussion

Compliance with gripper-level actuators promotes a safer robot-environment interaction as well as a practical way to perform force control. The use of permanent magnets as progressive springs was shown to be a feasible design to generate nonlinear progressive stiffness profiles. Such progressive stiffness has a large energy storage capacity as well as the attributes of both stiff and soft springs. This chapter discussed the generation of progressive stiffness profiles through smart magnet arrangement. Both MSEA and PMSEA have unique profiles for rotary and prismatic SEA applications respectively. MSEA, which has a rotary symmetric stiffness profile is capable of accurate force as well as impact mitigation and absorption. PMSEA, on the other hand, showed the feasibility of using a 3D manifold generated through linkage mechanisms to warp the stiffness profile. Such an effect can generate unique stiffness profiles that can be customized based on the required task.

Magnetic-based SEAs can be utilized in simple gripper modules that do not require precise positioning of the individual finger for simple grasping tasks. These tasks ,which need to be performed on the SORELL platform, include pick-and-place tasks where the gripper can use compliance to adapt to the shape of the grasped object. However, as discussed earlier, choosing the stiffness for a compliant actuator involves a lot of optimization and engineering trade-off. Generating a nonlinear stiffness profile using magnet arrangement provides a middle ground between linear SEAs which need to be optimized and VSA which require secondary input and hence a higher power requirement. It also gives the gripper a longer life cycle due to reduced wear and friction.

CHAPTER 5

Active Spring Grippers

5.1 Introduction

Chapter 4 introduced the use of permanent magnets in nonlinear spring designs through smart magnet arrangement. However, the springs discussed earlier have a fixed stiffness profile that cannot be changed online. Introducing a secondary input to a magnetic spring can have such an effect and give the spring a larger stiffness and force range. Adding a mechanism to change the stiffness also enables the spring design to take advantage of other electromagnetic phenomena that could be useful in grasping and manipulation tasks. These advantages come at the expense of more inputs complicating the system's design, control, and power requirements.

In this chapter, two variable stiffness actuators are introduced that use two different techniques to change the stiffness profile of the magnetic spring. The first, EMVSA, uses electromagnetic coils, which provide a fast method to change the stiffness. The second, AMVSA, uses mechanical inputs to change the polarity of magnets altering their interaction between repulsion and attraction. This chapter also explores the use of eddy current damping in robotic actuators to absorb impacts as well as water cooling for coil-based variable stiffness actuators.

5.2 Coil Induced Variable Stiffness

Variable stiffness joints could be in some cases more desirable than linear or nonlinear SEAs. Besides the benefits of compliant elements elaborated on earlier,

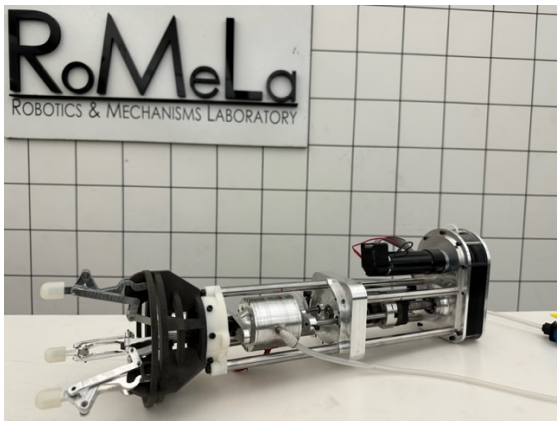


Figure 5.1: EMVSA with Gripper Hand

VSAs are more versatile as they can intrinsically change their stiffness. Such benefits include a wider bandwidth range, a better ability to absorb impact, and storing and recycle energy [37] [37] [61]. These benefits come at the expense of an extra actuator or a secondary input. Magnetic coils are a very good candidate for such actuators where changing the current through the coil causes a change in the stiffness. The biggest advantage of coils in VSA is that they have a very high response speed unlike mechanical VSA's where a motor has to drive a mechanism to achieve the stiffness change. The most popular way to achieve electromagnetic stiffness is through a magnet inside a coil. This method has been employed in vibration isolators and active springs for vibration control [81] [82] [83] [84] [85].

Not many researchers have investigated the use of an electromagnetic spring for robotic actuators owing to the complications that are associated with such mechanisms. [86] [59] both propose a magnet inside a coil for a variable stiffness spring; however, the spring presented in [86] does not consider bidirectionality and does not have a wide stiffness range. [59] proposes a magnet in coil for lower limb actuators, but, such an actuator would collapse with no current and does not make use of the available negative current range as an unstable equilibrium is very risky for actuators that operate in proximity to humans. Also, the maximum force achievable falls short of lower body requirements. Neither of these works considers

cooling techniques and relies on evaluating their data points in a discontinuous fashion indicating the actuator cannot stay powered for prolonged periods due to heating.

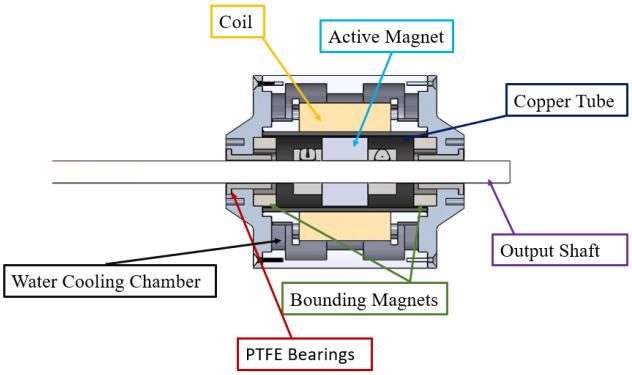
5.2.1 EMVSA

The Electro-Magnetic Variable stiffness Actuator, EMVSA, is a new variable stiffness actuator that is based on coil-induced stiffness variation. EMVSA has a very wide stiffness range compared to predecessor designs, bounding magnets to establish a baseline stiffness curve, eddy current-based damping for shock absorption, and is cooled through immersion water cooling. EMVSA is designed for robotic grippers and hands that are at constant risk of impact.

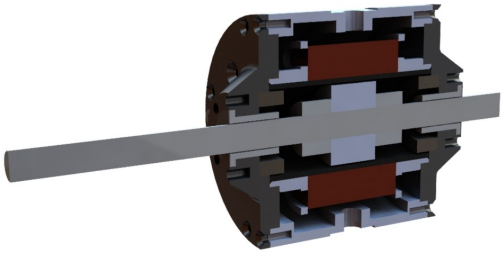
5.2.2 EMVSA Design

EMVSA consists of an electromagnetic spring as well as a gripper module as shown in Fig. 5.1. Fig. 5.2a shows the design and components of EMVSA magnetic spring, which incorporates an active N52 PM bonded to a nonmagnetic output shaft. The active magnet and shaft are free to slide and are the spring's output. The active magnet is bounded by two PMs at each end of the spring. The active magnet is in repulsion with both bounding magnets giving EMVSA an intrinsic nonlinear stiffness profile. The baseline stiffness of EMVSA is important as it gives the spring stiffness without the need for any input, reducing the need for constant current in the coil. It also enables the spring to vary the stiffness with both positive and negative currents while maintaining the stable point in the center. The ability to use both directions of current doubles the range of stiffness and force that the spring can achieve. The active PM is free to move in an air chamber in the middle of the spring that is surrounded by a copper tube with the coil wound on the tube. A casing then encapsulates the coil to create the cooling

chamber of the spring. The copper tube shields the permanent magnets from the cooling chamber and is connected to custom-made flanges that work to conduct heat away from the core of the spring toward the cooling fluid reducing trapped heat. Figs. 5.3b and 5.3a show the manufactured spring EMVSA and cooling chamber.



(a)

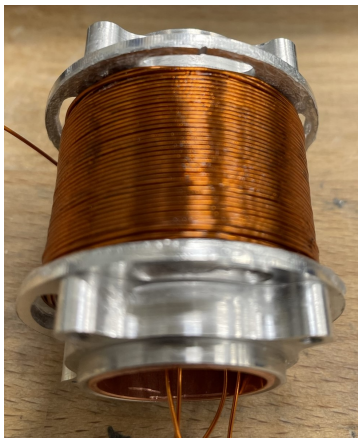


(b)

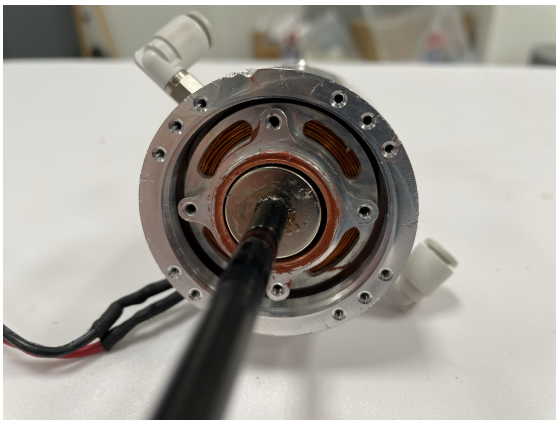
Figure 5.2: Cross-section CAD model of EMVSA spring

5.2.3 Spring Modeling

In this section, the EMVSA spring stiffness was modeled through semi-analytical, FEM, and experimental methods. These models will be compared and assessed.



(a) Custom EMVSA coil with cooling flanges



(b) Manufactured EMVSA with one end open

Figure 5.3: EMVSA coil and cooling chamber

As for the damping effect of the copper tube, an experimental method is used to determine the damping coefficient.

5.2.3.1 Analytical

Three electromagnetic forces are acting on PM_A that need to be dissected and modeled. The first two, the force due to the stationary magnets and the coil, are position-dependent. The third is the eddy current braking force which is velocity-dependent. These forces are shown in Eq. 5.1 where F_K is the restorative force due to magnets and coil and F_D is the force due to eddy current damping. This section is concerned with modeling the restorative force, F_K based on the Coulombian model. The Coulombian model treats magnets as electrically charged surfaces as detailed in [87] [88] [68] [89] [59]

The total force on PM_A is shown as,

$$F_T(x, \dot{x}) = F_K(x, I) + F_D(\dot{x}) \tag{5.1}$$

Table 5.1: Magnetic spring parameters

Variable	Symbol	Value (in)
Coil Outer Radius	R_{co}	0.4375
Coil Inner Radius	R_{ci}	0.75
Coil Length	L_c	1.0
Coil Turns	N	650
Copper Tube Outer Radius	R_{to}	0.4375
Copper Tube Inner Radius	R_{ti}	0.3925
Copper Tube Inner Length	L_t	1.8
PM_S *Outer Radius*	R_{so}	0.375
PM_S *Inner Radius*	R_{si}	0.25
PM_S *Height*	H	0.25
PM_A *Outer Radius*	R_{ao}	0.375
PM_A *Inner Radius*	R_{ai}	0.125
PM_A *Height*	B	0.5

The modeling of F_K is split in two, the force due to bounding permanent magnets and the force due to the coil. Eq. 5.2 shows that F_K is composed of two force components due to the bounding magnets,F_{S1} and F_{S2}, and one force component due to the coil F_C. Note that the force F_{S1} and F_{S2} are position-dependent while the F_C is dependent on the position as well as the current. This analytical problem is divided into three parts In this model, the force on PM_A from both bounding PM_A is deduced. Then the model of the force on PM_A due to the coil is developed and the results are combined to provide a semi-analytical model for the whole spring. According to Fig. 5.4, the force acting on the output of the spring is a function of both the displacement and the velocity of the active magnet as well as the current in the coil. On the other hand, the damping part of the force,F_D is due to the active magnet moving through the copper tube.

$$F_K(x, I) = F_C(x, I) + F_{S1}(x) + F_{S2}(x) \tag{5.2}$$

Coil Force The force due to the coil can be analytically written through the Coulombian model. In this case, the field intensity inside the coil due to an inducing current is assumed uniform in the axial direction. In this model, the force due to the field generated by the coil on the two charged surfaces of PM_A is seen in Fig. 5.4. The parameters used in this model are shown in 5.1 where $h = H/2$, $l = L/2$, and $b = B/2$ are used to simplify the model.

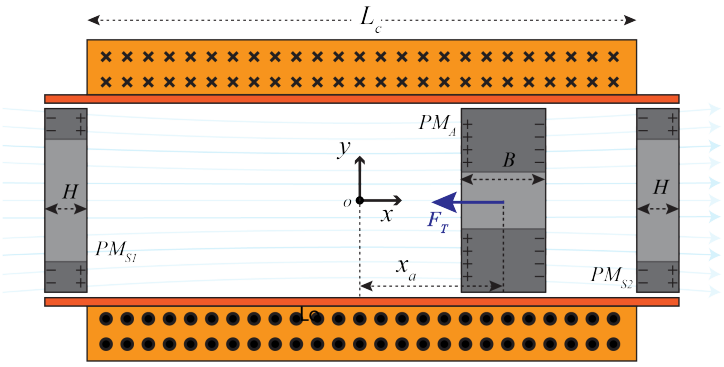


Figure 5.4: EMVSA coil and permanent magnet Arrangement

The field induced by the coil on one of the surfaces of the PM_a is:

$$B_K = \int_{R_{ci}}^{R_{co}} C \left(\frac{x+l}{\sqrt{r^2+(x+l)^2}} - \frac{x-l}{\sqrt{r^2+(x-l)^2}} \right) dr \tag{5.3}$$

Where C can be written as follows:

$$C = \frac{\mu_0 N I}{2L(R_{c0} - R_{ci})} \tag{5.4}$$

In Eqs. 5.3 and 5.4, I is the current through the coil and $\mu_0 = 4\pi \times 10^{-7}$ is the permeability of free space. The force of the coil on PM_A is then the sum of the forces acting on each charged surface of PM_A separately. The force on a single

face is the surface integral of the magnetic field intensity over the area of PM_A for the two sides of the magnet as shown below.

$$F_C(x, I) = \frac{B_{ra}}{\mu_0} \int_S (B_K(x - b) - B_K(x + b))\, dS \tag{5.5}$$

Where B_{ra} is the residual magnetic flux of the permanent magnet PM_A.

Analytically solving the integral in Eq. 5.5 yields the following.

$$\begin{aligned} F_C(x, I) = D\,[&(x - b + l)\Psi(x - b + l) \\ &-(x - b - l)\Psi(x - b - l) \\ &-(x + b + l)\Psi(x + b + l) \\ &+(x + b - l)\Psi(x + b - l)] \end{aligned} \tag{5.6}$$

Where D is:

$$D = \frac{B_{ra} NIS}{2L(R_{co} - R_{co})} \tag{5.7}$$

and the function $\Psi(x)$ can be written as:

$$\Psi(x) = \ln \frac{R_{co} + \sqrt{R_{co}^2 + x^2}}{R_{ci} + \sqrt{R_{ci}^2 + x^2}} \tag{5.8}$$

Stationary magnet force The force on PM_A due to one of the stationary permanent magnets can also be modeled through the Coulombian model. The model will first be derived for one stationary magnet and then generalized for the

two stationary magnets as seen in Fig. 5.5.

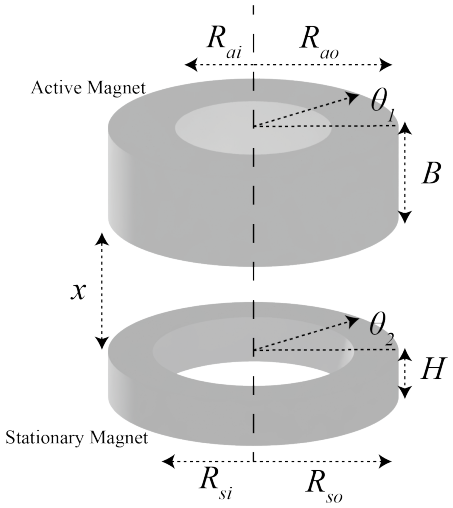


Figure 5.5: Active magnet and stationary magnet Pair

The force from the stationary magnets PM_{S1} on the active magnet can be analytically written as the sum of the forces between all the charged surfaces between two magnets. For a pair of cylindrical magnets one PM_{S1} and PM_A as in Fig. 5.5. The force of stationary magnet PM_S1 on the active magnet PM_A, F_{S1}, can be written as the surface integral of the magnetic field of PM_{S1} acting on the two charged surfaces of PM_A.

$$F_{S1}(x) = \frac{B_{ra}}{\mu_0} \int\int_S [B_{S1}(l - x - h) - B_{S1}(l - x + h)]\, dS \tag{5.9}$$

Where B_{S1} is the field generated by PM_{S1} at both the charged surfaces of PM_A. Hence, the force due to one surface of one magnet on the other is the surface integral over the two surfaces. The total force is then the sum of the surface integral for the four pairs of opposing surfaces. Eq. 5.10 shows the force as the surface integral for the four pairs of surfaces between PM_A and PM_{S1}.

$$
\begin{aligned}
F_{S1}(x) = \int_0^{2\pi} \int_0^{2\pi} \int_{R_{si}}^{R_{so}} \int_{R_{ai}}^{R_{so}} \\
&[(l-x-h)\alpha(l-x-h) \\
&-(l+b-H-x)\alpha(l+b-H-x) \\
&-(l+b-x)\alpha(l+b-x) \\
&+(l-b-H-x)\alpha(l-b-H-x)] \\
&dr_1 dr_2 d\theta_1 d\theta_2
\end{aligned}
\tag{5.10}
$$

Where the function $\alpha(x)$ is written as:

$$
\alpha(x) = \frac{B_{ra}B_{rs}}{4\pi\mu_0} \frac{r_1 r_2}{(r_1^2 + r_2^2 - 2r_1 r_2 cos(\theta_1) + x^2)^{\frac{3}{2}}} \tag{5.11}
$$

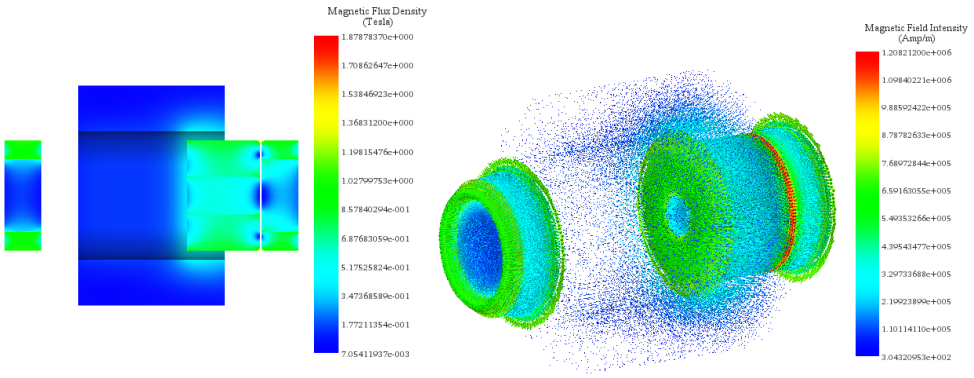
Since the active magnet is positioned in the middle between the two stationary magnets, the force due to the second stationary magnet on the active magnet can be written as,

$$
F_{S2}(x) = -F_{S1}(l+x) \tag{5.12}
$$

5.2.3.2 Simulation

The EMVSA spring has been statically simulated using EMS simulation software. The simulation was performed over the three permanent magnets as well as the coil and ignored other components for simplicity. A sample simulation results in EMS are shown in Fig. 5.6 for the magnetic field intensity and density in the case PM_A is at a maximum deflection. The simulation was performed over the

range of the spring which is [-0.5in 0.5in] and for a current range of [-8A 8A]. The resultant surface which denotes the force due to the current and the position of PM_A is shown in Fig. 5.9.



(a) Magnetic field density (b) Magnetic field intensity

Figure 5.6: Simulation sample results for EMVSA spring in EMS for maximum PM_A deflection

5.2.3.3 Experimental Model

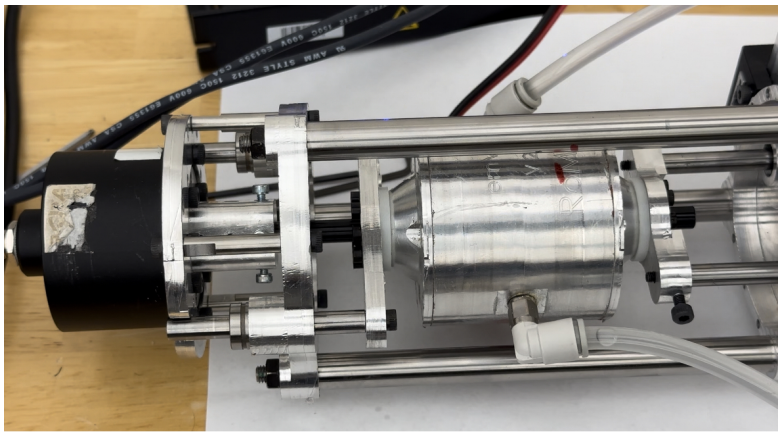
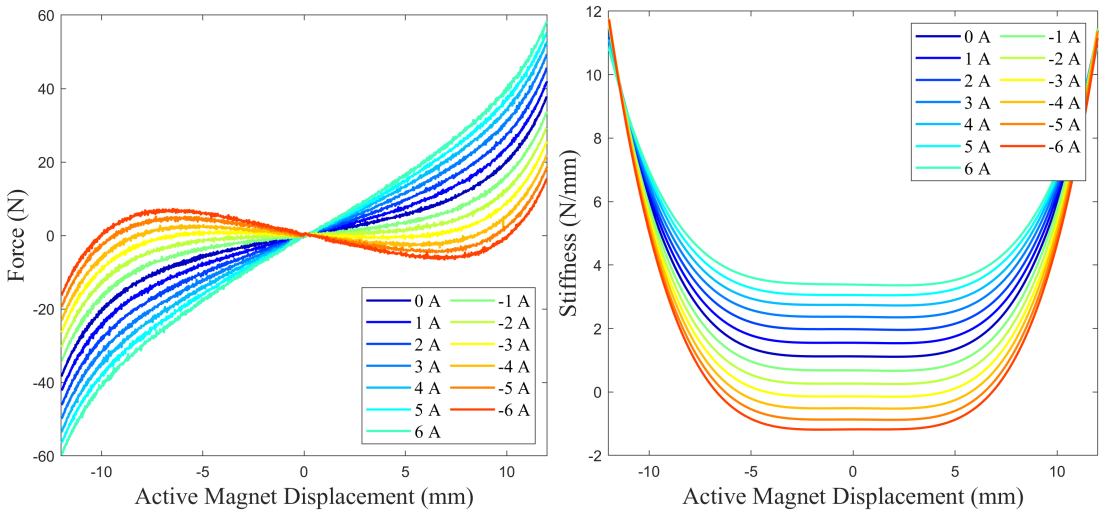


Figure 5.7: EMVSA high impedance test setup

The experimental model of the spring was obtained through a high-impedance test setup shown in Fig. 5.7. In this test set-up the spring is driven through a ball-screw mechanism with the output shaft of the spring fixed to an FT sensor

while the spring chassis is driven to extend the spring. The FT sensor used is a Bota Rokubi. Note that the variation in the spring deflection is done in a very slow fashion to avoid capturing the eddy current friction component. This experiment is repeated by holding the current through the coil constant and varying the deflection. The current is varied in the range of [-6A 6A] with a step current of 1A. Fig. 5.8a shows the force profiles obtained from the high-impedance experiment. Fig. 5.9 shows the stiffness curves that are derived through MATLAB curve-fitting tools from the force profiles.

The force profiles of EMVSA show that at a current of 0A, the spring has an intrinsic nonlinear profile. As the current is increased, the profile is stiffened and softened when decreased. In the case that the current in the spring drops below -3A, there will exist a region of negative stiffness. This region will make the equilibrium point of PM_A at an unstable equilibrium that can hinge towards a certain direction due to any perturbations. This effect was intentionally introduced to the spring as its proposed use will be discussed in later sections.



(a) EMVSA force profiles

(b) EMVSA stiffness profiles

Figure 5.8: EMVSA Experimental Model Results

Fig. 5.9 shows the 3D surfaces of the force profiles for all models performed.

As expected the simulation and experimental results are closer to each other when compared to the analytical model. However, the analytical model can be seen as more accurate than the dipole model that was used in Chapter 4. That is because the Coulombian model does not reduce the whole magnet into a point dipole but rather considers the surface as a whole. The shortcomings of the Coulombian model are that it does not consider the volume of the magnet but just the flat surfaces. Moreover, some parts of the analytical model had to be numerically calculated due to the complexity of the expression.

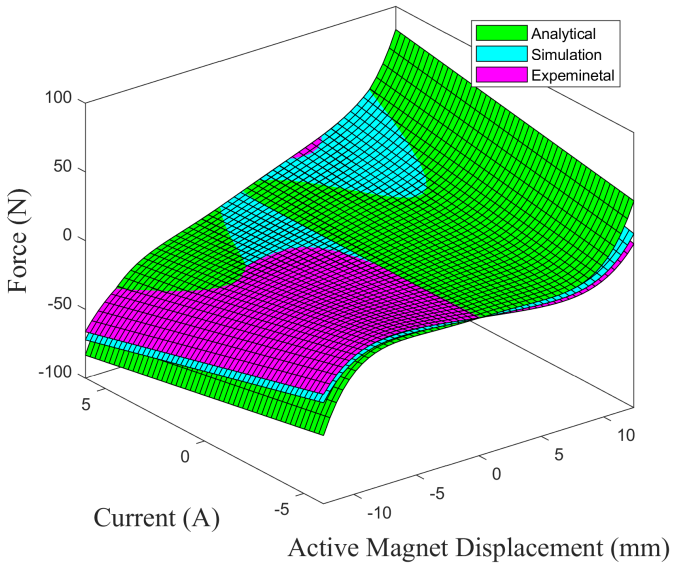


Figure 5.9: 3D surface for curve fit of the force-displacement-current

5.2.3.4 Controller

The EMVSA hand controls the position and stiffness of the spring through two independent PID controllers. The current is controlled through a PID controller with a feedforward term while the position controller is based on the concept of gain scheduling. The gain scheduling variable is the estimated spring stiffness of the spring based on the measured current and position values. These controllers were used to assess the ability of the gripper to track force based on position

control as well as the stiffness of the spring. In a later section, a more complex controller is developed based on a linear varying parameter LQR method. Fig. 5.11 shows the clock diagram for the EMVSA system which includes how the EMVSA is controlled.

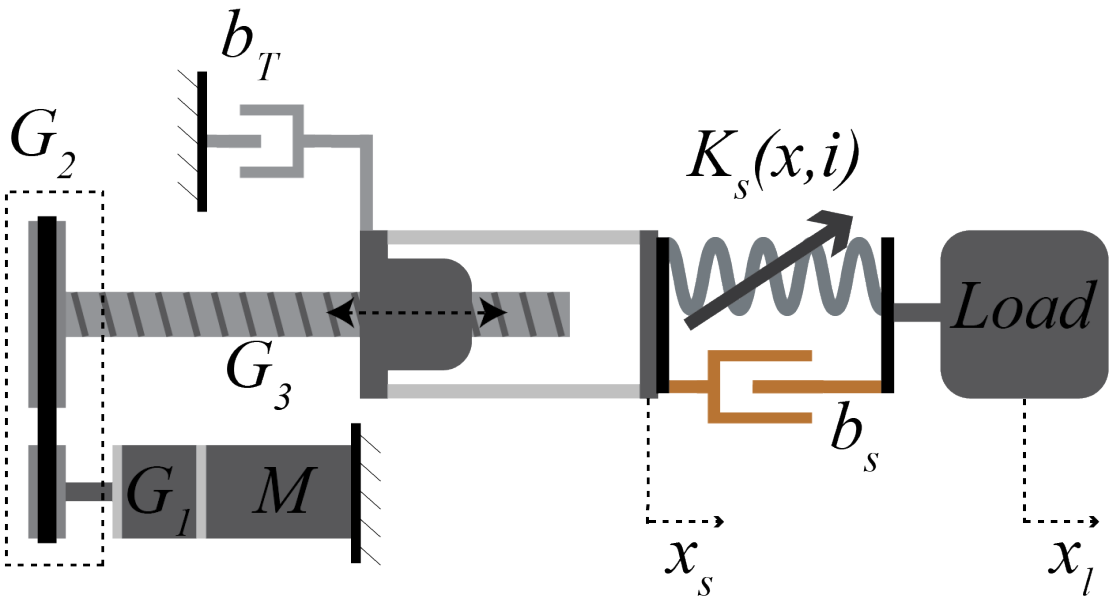


Figure 5.10: EMVSA Diagram

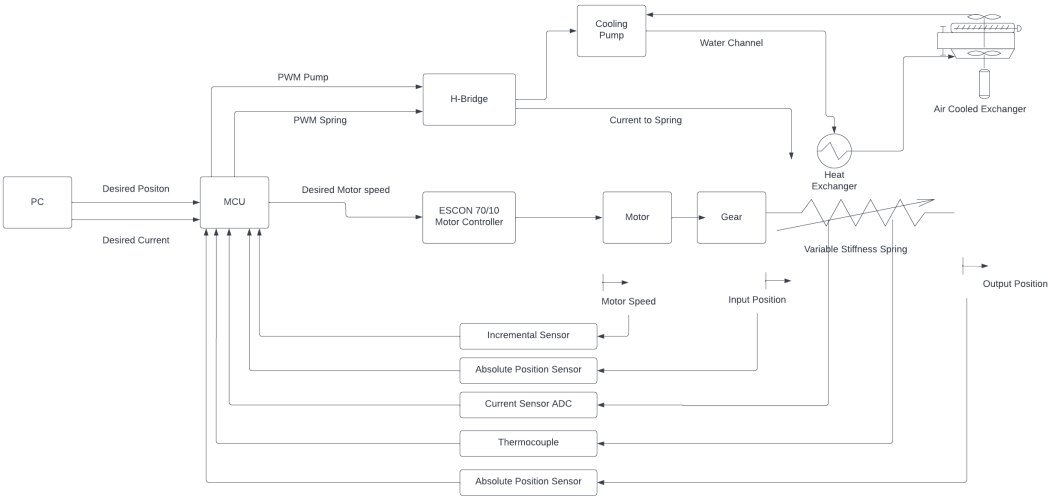


Figure 5.11: EMVSA Block Diagram

5.2.4 Results

5.2.4.1 Water Cooling

A thermal electromagnetic simulation was performed using EMS to evaluate the heat efficiency of EMVSA. Since varying the stiffness in EMVSA depends on the current running through the coil, cooling is an essential component. Multiple previous works have not expanded their use of such actuators due to heating issues. Effective cooling does not extend the maximum field a coil can generate but it increases the time at which such current can flow through it. there are multiple ways a core can be cooled down including through ambient or forced air flow. One of the most effective is through immersion cooling where the whole coil is surrounded by a coolant fluid. Immersive cooling allows EMVSA to run for prolonged times and to reduce power losses due to temperature increase 5.20.

The temperature of the coil was modeled through EMS for different currents and using water as the cooling medium. Fig. 5.12 shows the simulated temperature of the core with immersion water cooling. Simulation results show that the actuator has good heat management up to the simulated current value of 10Amps. It is also seen that for such a high current, the temperature does not cross the threshold of $80C^{\circ}$, which is the temperature the permanent magnets start losing their magnetization. It is important to note that the design of the core itself utilizes flanges and the copper tube to conduct as much heat away from the center of the coil which is the least exposed to the cooling fluid as seen in Fig. 5.3a.

5.2.4.2 Force Control: Spring Positioning

Under a high-impedance setting shown in 5.7, step and sine wave tracking experiments were performed. The force values are measured through an FT sensor to confirm the force in the spring. The force-tacking experiments use the position feedback and the experimental model of the spring to achieve the force feedback.

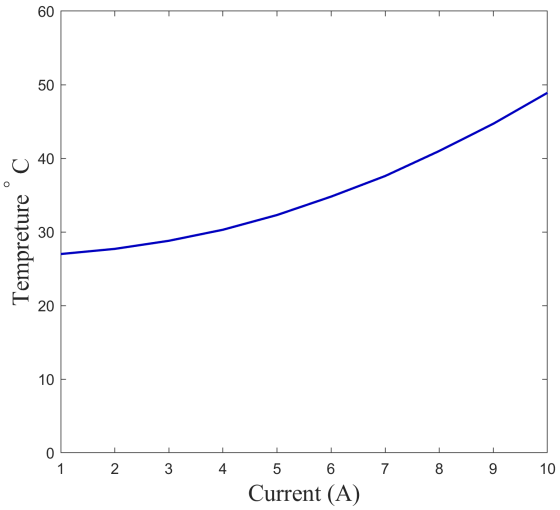
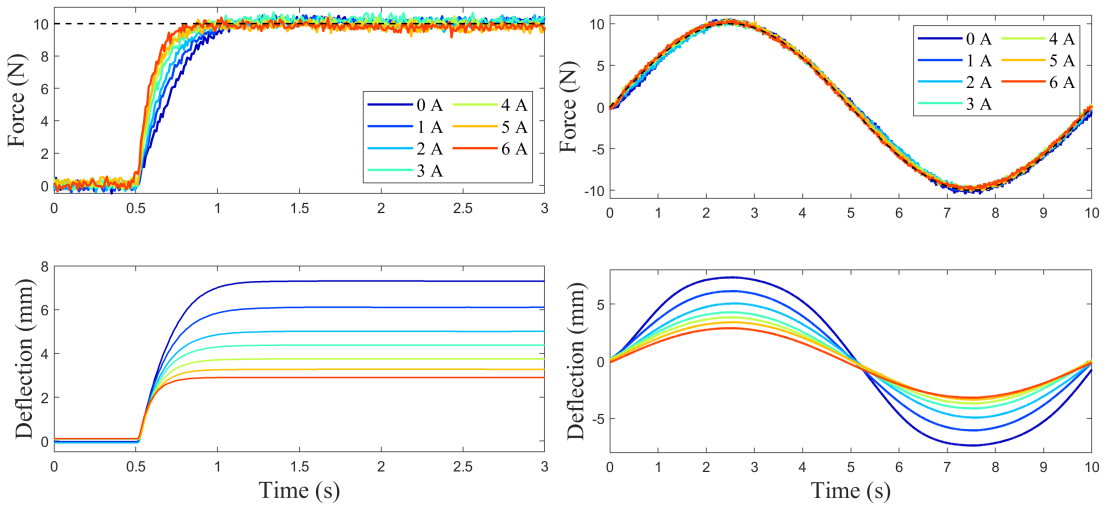


Figure 5.12: EMS simulation of EMVSA core tempreture

In the step response experiments, the current is held constant at discrete values, then a desired force value is commanded. Fig. 5.13a (top) shows a desired force value of 10N for the current values in the range [0 6A] with a current step of 1A. As can be seen, the force rise time decreases with higher stiffness in the spring. This can be explained through Fig. 5.13a (Bottom) which shows the spring-measured deflection for each case. As the current is increased and hence the stiffness, the deflection needed from the spring to achieve the same force is reduced. As for the variable force response, the same methods were used but a sine wave of 10N at 0.1Hz comprises the desired force. The same applies to the variable force tracking, using higher stiffness requires lower displacement. This can be confirmed in Fig. 5.13b. For both of these experiments, it is evident that the actuator can perform accurate and stable force tracking. EMVSA can hold the force constant for the step response as well as accurately track sine functions. For the sine tracking response experiments, the current data was also collected and shown in Fig. 5.14. This current data is collected through a current sensor and shows the ability of the controller to hold the current constant as the force-tracking experiments are performed.



(a) Step response (b) Sine response

Figure 5.13: Step and sine response of EMVSA force tracking for a 10N amplitude by spring positioning

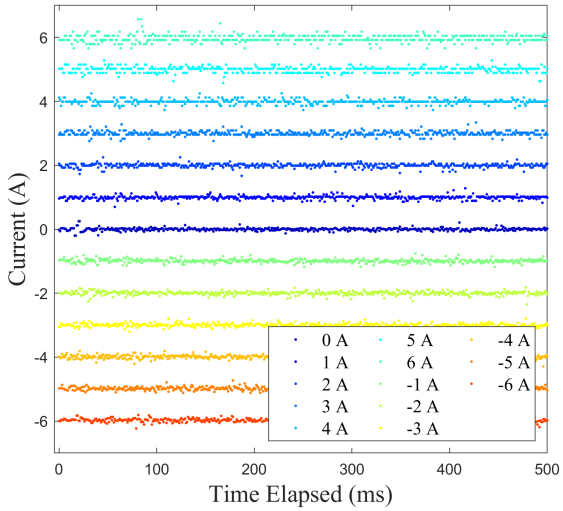
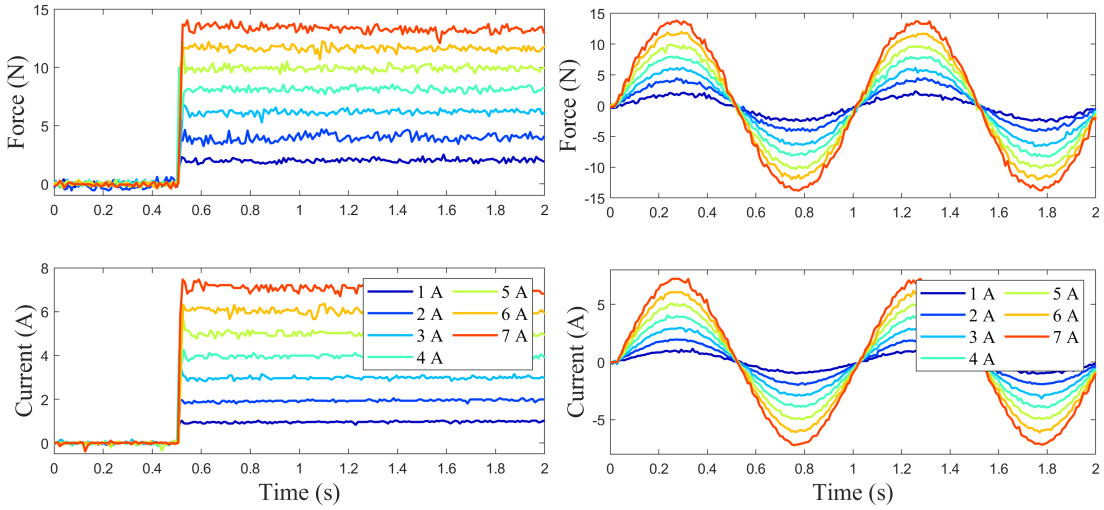


Figure 5.14: Sample current values through the coil for sine tracking experiment

5.2.4.3 Force Control: Current Variation

A second way to achieve accurate and fast force control is to vary the current at a given position. Using the same model, a force controller can be developed based on the current feedback. In these sets of experiments, the spring is deflected

to 5mm and held at that position. Then at that position, a current step and sine inputs are commanded. As the current is varied, the force in the FT sensor is measured. Note that the FT sensor is zeroed at the 5mm position. Two experiments were performed with this setup. The step current response is shown in Fig. 5.15b (Bottom), while Fig. 5.15b (Top) shows the corresponding force. The current was also varied through a sine function with a 1Hz frequency shown in Fig. 5.15b.These experiments show the ability of EMVSA to accurately track current values, as well as using the stiffness variation to control the force in the spring. In both cases, the response time is very low which shows the viability of using electromagnetic means to achieve fast and reliable stiffness variation.



(a) Step response (b) Sine response

Figure 5.15: Step and sine response of EMVSA current tracking

5.2.4.4 Bandwidth

The bandwidth of the system was also assessed for both high and low-deflection amplitudes. A sine sweep was commanded on the force controller for 0.5N and 10N amplitudes. These experiments are both performed with zero current flowing through the spring. The bandwidth of the actuator with the sine sweep ampli-

tudes of 0.5N and 10N, measured at the -3dB mark 12Hz, are 3.8Hz and 12Hz respectively.

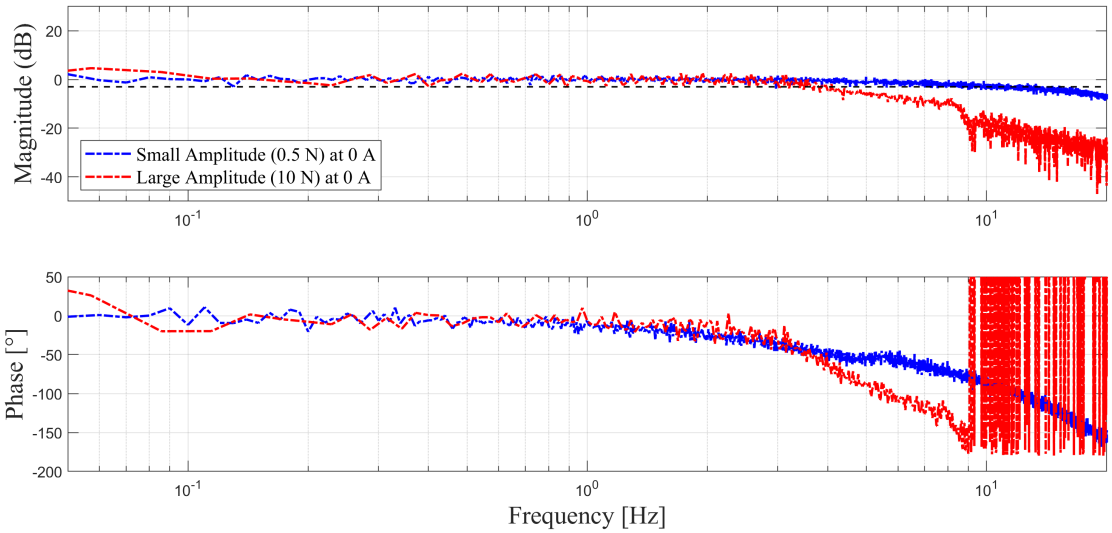
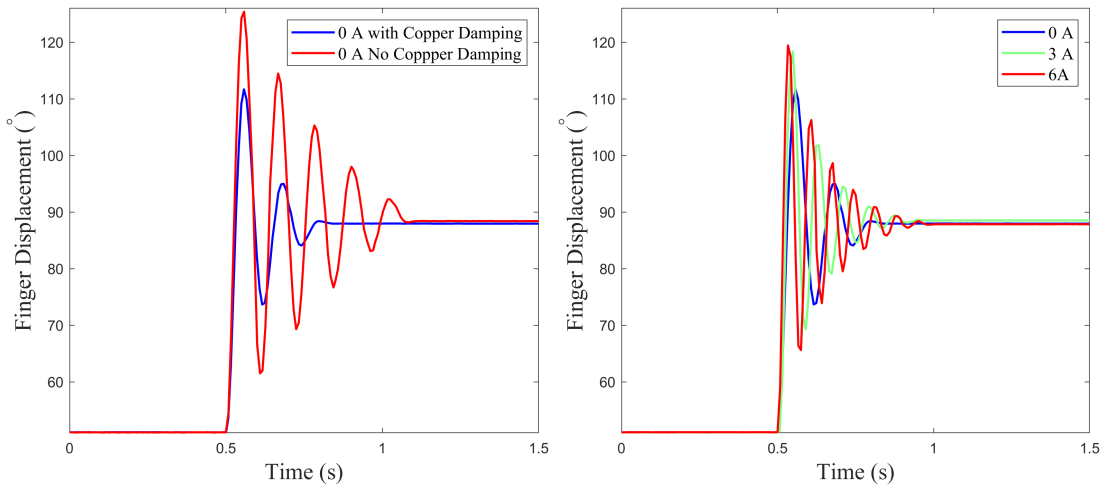


Figure 5.16: EMVSA force tracking bandwidth for zero current

5.2.4.5 Free Response

To test the effects of the copper tube in inducing eddy current breaking a second spring was built that does not include a tube. Both springs were subjected to the same deflection of the spring fingers as in Fig. 5.20 and then released. Fig. 5.17a shows the free response in both of these cases. It's clear that the spring that includes the copper tube, the gripper finger has a lower overshoot as well as a shorter time to reach equilibrium. This feature is very useful in case of impact on the gripper fingers as the damping effect can reduce the effect of the high-frequency impact. The copper tube also helps in stabilizing the response of the spring. This effect was also simulated in EMS and shown in Fig. 5.18. The same experiment was also perfromed for different current values in the spring which is shown in Fig. 5.17b.



(a) Effects of copper eddy-current Damping (b) effect of increased stiffness

Figure 5.17: EMVSA free response plots

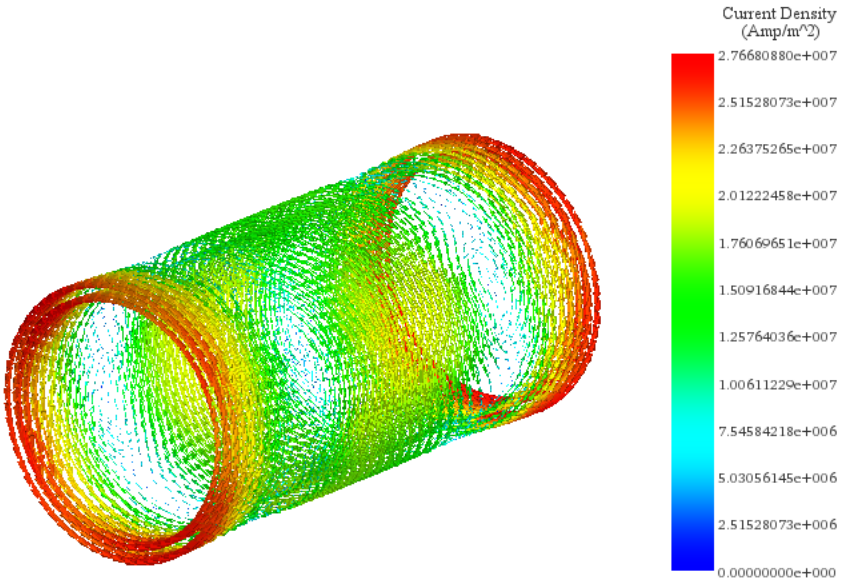


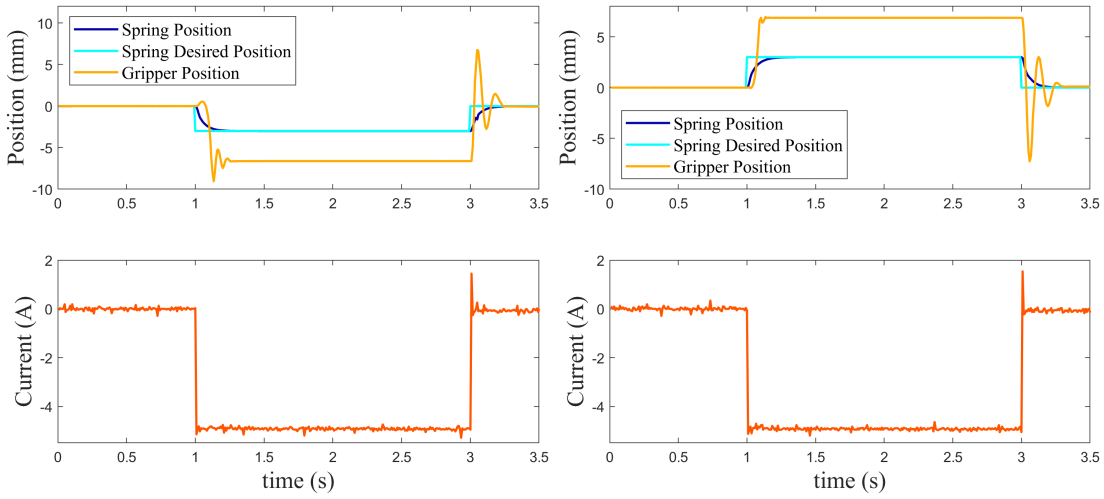
Figure 5.18: EMVSA eddy current simulation in EMS.

5.2.4.6 Instability Grasping

For a gripper to grasp an object the motor will have to drive the fingers to the desired position. The speed of the system is then covered by the mechanical

dynamic properties of the system. However, negative stiffness can be used to achieve explosive motion on the gripper for quick grasping and releasing. This is done by exploiting the unstable equilibrium point in the middle of the EMVSA when the current is at or below -3Amps. In these currents, the gripper becomes a bistable one where the stable points are towards the ends of the spring. To make use of such instability, a perturbation in the direction of the spring chassis, will cause the spring to tilt towards one stable point over the other.

This effect is shown in Fig. 5.19, where it is applied for grasping 5.19a and releasing 5.19b. For grasping tasks, the spring current is set for -5Amps while the position is commanded to -3mm at the same time. This will perturb the spring enough to henge the gripper towards closing. The opposite is done in the case of releasing the gripper from a grasping position. This effect could be very useful for grasping tasks that require fast response and will give a chance for the mechanical assembly to catch up to the grasping position.



(a) Grasping (b) Releasing

Figure 5.19: Exploiting instability region for fast explosive motion

5.2.5 Application

A multipurpose gripper, shown in Fig. 5.20, shows a manufactured gripper designed to be used with EMVSA for testing and general applications. The gripper has 3-fingers each consisting of a 4-bar mechanism. The 3 fingers are connected to a coupling platform that links them to the spring's output. This actuator can be used as the main compliant element of multiple gripper designs. The gripper proposed can be used as a multipurpose gripper that has a large risk of collision and requires large forces. This actuator can be used as a peripheral attachment to SORELL's leg when operating in tripod mode. The fact that SORELL uses water-cooled actuators makes it easy to incorporate into SORELL's water-cooling network.

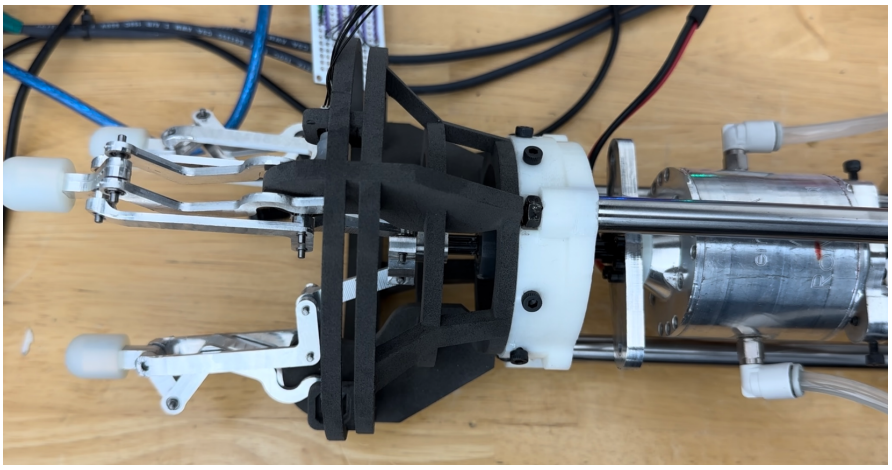


Figure 5.20: EMVSA Gripper

5.3 Mechanically Induced Variable Stiffness

Previous sections have demonstrated the use of magnetic repulsion in magnetic springs for robotic grippers, however, magnetic attraction can also be utilized in certain cases where an explosive motion is needed. [46] and [90] have shown that an explosive release of energy can be used to create very fast motions of

required and [91] has shown a parallel magnetic spring that works through catch and release, where at some instances it stores energy then releases in a cyclic motion. The magnetic attraction has not been traditionally applied to SEAs or VSA. However, some authors have shown how magnetic attraction can be used in grippers. Both [92] and [93] have shown how an electromagnet(EM) or permanent magnet (PM) can be used to align a gripper or even grasp ferrous objects. Some grippers use magnetic attraction to achieve bistability where an EM would drive a stage between two stable configurations of a gripper. The antagonistic bi-stable magnetic gripper proposed in this section uses an antagonistic configuration of two switchable magnetic springs that can change between negative and positive stiffness through a driven motor.

5.3.1 AMVSA

The Antagonistic Magnetic VSA is a variable stiffness actuator that uses a magnetic agonist-antagonist pair shown in Fig.5.21. In the antagonistic configuration, the position of the finger can be controlled by controlling the positions of the driving motors. The stiffness of the spring can be controlled by adjusting the pretension on the springs; however, that is only possible when using nonlinear springs. If the springs used are variable stiffness springs, then the pretension can be adjusted online, which means that the position of the finger can be controlled by changing the pretension of one of the springs.

The unique design of AMVSA enables the antagonistic spring pairs to flip between attraction and repulsion. AMVSA can control the positioning of a finger through stiffness variation, as well as use the instability of negative stiffness to produce fast explosive motion.

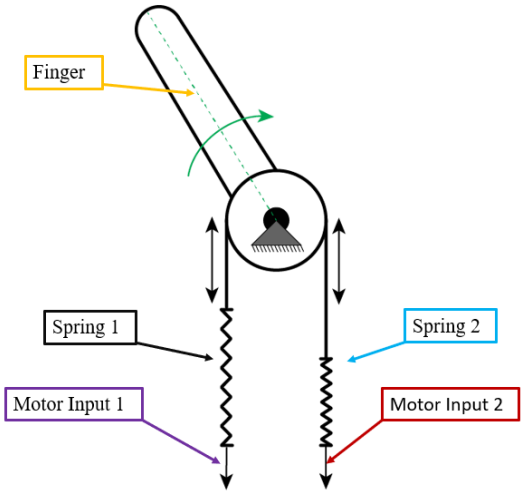


Figure 5.21: Antagonistic configuration on a single finger gripper

5.3.2 Mechanical Design

Fig. 5.23 shows the proposed configuration of the gripper. The design is composed of two magnetic springs that can alternate between attraction and repulsion. The pair of magnets on the left labeled (driving magnet 1 and driven magnet 1) will be referred to as the proximal spring while, the one labeled (driving magnet 2 and driven magnet 2) will be referred to as the distal spring.

When the proximal spring is in attraction mode (opposite poles facing each other) then the finger will collapse inwards. The opposite will happen when the distal spring is in attraction mode which will cause the fingers to open. When both the distal and the proximal springs are in repulsion mode (same poles facing each other) then the finger will be hanging between the two repelling sides. The stiffness and the position can be changed, albeit not independently. The stiffness can be changed by increasing or decreasing the angle of the driving magnet.

A single finger was also manufactured and is shown in Fig. 5.24. This prototype consists of two antagonistic pairs of springs that tug on a single finger. The driven magnet in this prototype slides inside a copper tube to make use of

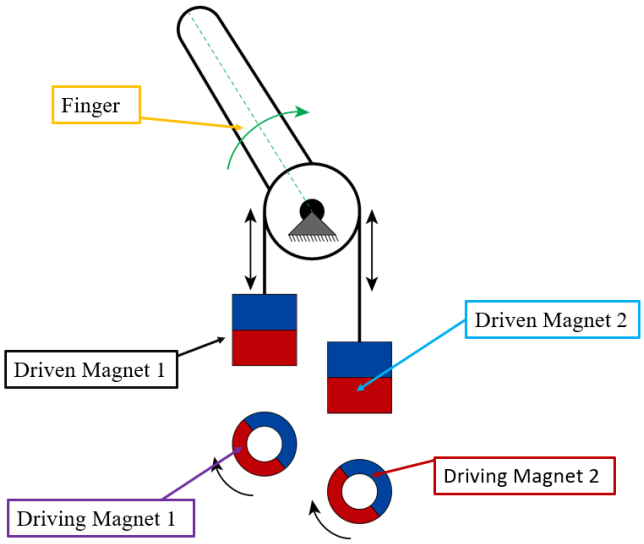


Figure 5.22: Schematic of proposed antagonistic magnetic VSA

eddy current-breaking for shock absorption. Each driving magnet is connected to a Dynamixel XM-430 servo motor to control the positioning of the driving motor. The finger itself consists of three links, with a magnetic absolute encoder used to measure the position of the finger.

5.3.3 Simulation

To assess the feasibility of the proposed design a simulation study was performed using EMWorks EMS software [69]. Fig. 5.25 shows the vertical force between a pair of one diametrically magnetized spring and one axially as shown in 5.23. For each simulation curve, the angle is fixed while the separation is varied between [0 0.55in]. It can be shown that when the angle is between [0° 90°] the stiffness will be positive and vice versa if the angle is between [-90° 0°]. It is worth noting that when then the angle is at exactly 90° the stiffness will be zero.

Such stiffness profiles of each single pair of magnets, enable the finger to operate in multiple modes. Referring to Fig. 5.23, the finger has three main operation modes. The magnet pairs, driving magnet 1 and driven magnet 1, will be referred

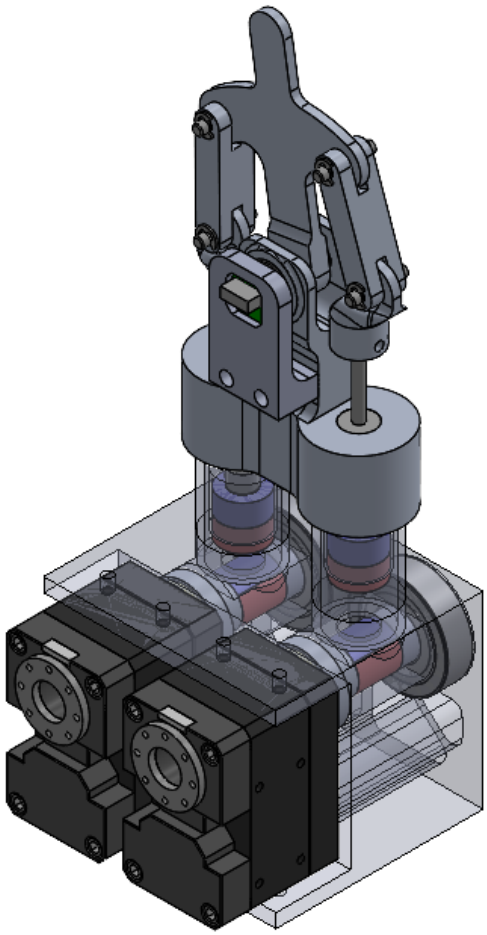


Figure 5.23: AMVSA CAD model

to as spring 1, and similarly for the driving magnet 2 and driven magnet 2 pair.

- Unstable equilibrium: in the case that both springs 1 and 2 are in attraction mode: opposite pairs are facing each other (negative stiffness). Then the finger will be at an unstable equilibrium. This can be exploited by perturbing the finger in one direction and generating a fast explosive motion. once one of the springs reaches saturation, the attractive force will be at its maximum and the finger will be locked in that position. Such locking force is crucial for achieving a tight grip on a grasped object.

- Stable equilibrium: in the case that both springs 1 and 2 are in repulsion,

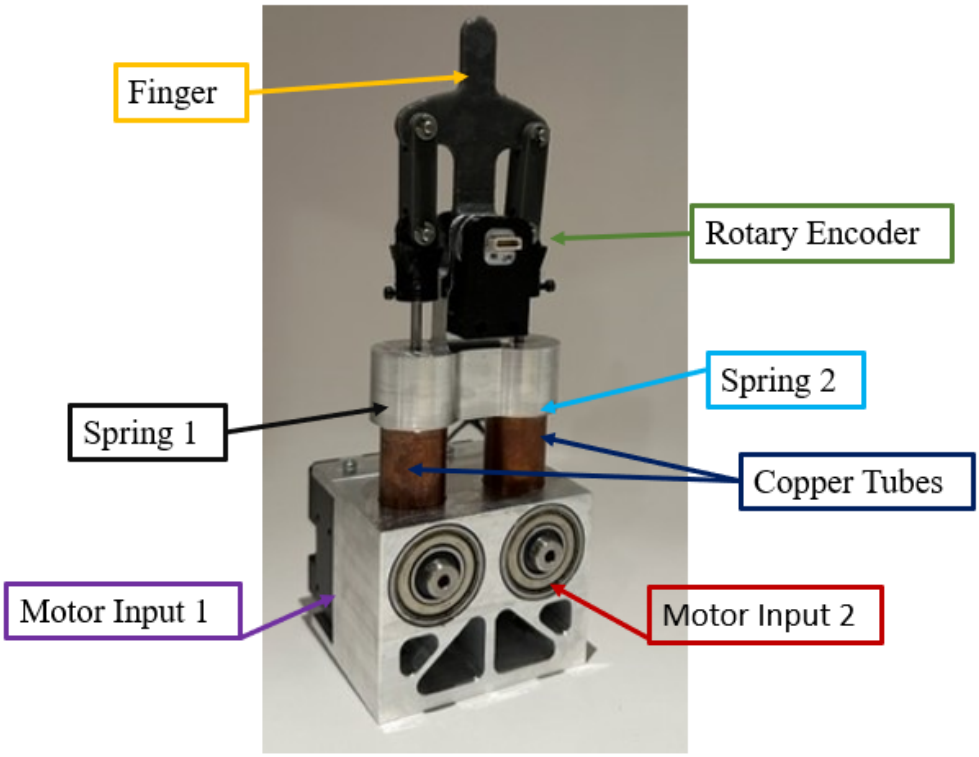


Figure 5.24: AMVSA assembled prototype

then the finger will be in a stable equilibrium. At this point, the position of the spring can be controlled by changing the stiffness of one of the springs. For instance, adjusting the angle of driving magnet 1, such that it increases the stiffness of spring 2 will push the finger to rotate in the counterclockwise direction, and vice versa for spring 2. Such a design is similar to the antagonistic configuration where the position of the linkage is done through stiffening one spring.

- Zero stiffness: in the case that both springs 1 and 2 are in zero stiffness mode i.e. the magnetization vector of the driving magnets is perpendicular to that of the driven magnets. Then the stiffness throughout the travel of the finger will be near zero. This can be used in cases where the finger needs

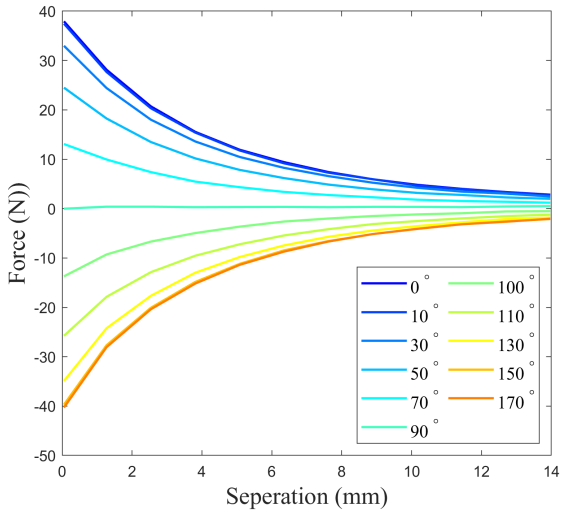


Figure 5.25: Single spring force-displacement curves

to be back-drivable and just dissipate energy. Note that due to the copper tube that the driven magnets move in, there is a damping component that is due to eddy current. this provides the finger with the ability to dampen vibrations and dissipate energy from shocks and impacts.

5.3.4 Application

The AMVSA prototype shown in Fig. 5.24 is a proof of concept for a single finger using two magnetic springs and two motors. However, to make this design more practical, a whole hand has been designed to show the potential use of such an actuator. The hand shown in Fig. 5.26 is a 3-finger gripper, with each finger having the same design as the single-finger design in Fig. 5.24. This design is under-actuated, where one motor drives the proximal driving magnets for all three fingers while a second motor drives the distal ones. The coupling assembly is shown in Fig. 5.27, where a single servomotor drives a bevel-gear transmission that controls the position of three driving magnets.

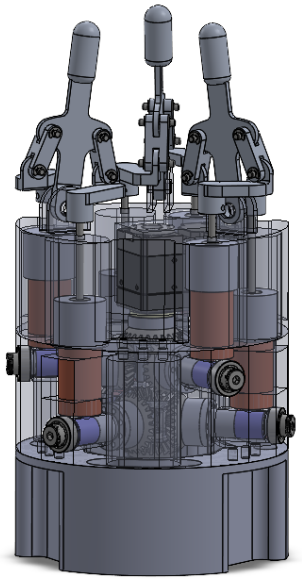
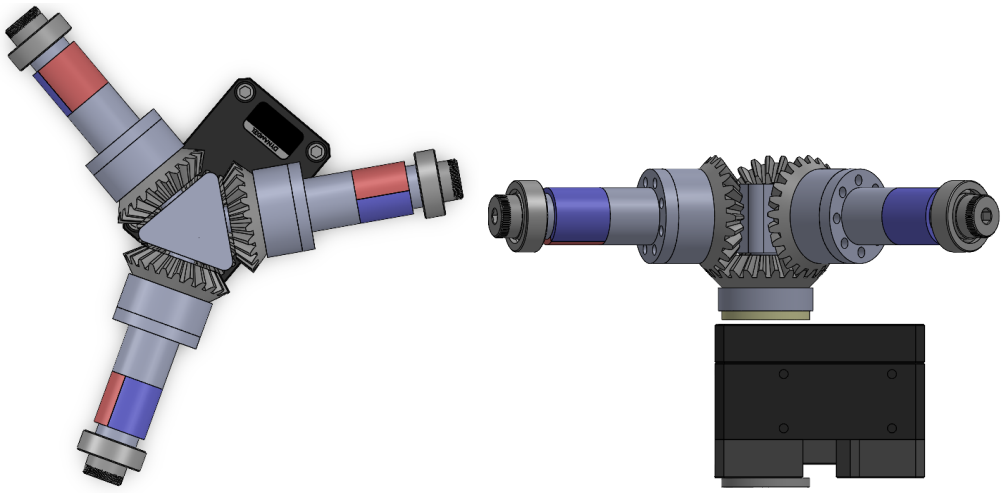


Figure 5.26: AMVSA three-finger under-actuated hand

5.4 Discussion

Nonlinear magnetic springs were shown to be a reliable middle ground between stiff and soft springs. However, certain tasks could require a more active method to control the stiffness independent of the spring deflection. This chapter, introduced two methods to change the nonlinear stiffness curves through both electromagnetic and mechanical methods. Despite the increased complexity and power requirements of the mechanisms presented in this chapter, they were shown to be effective at changing the stiffness profile of a spring.

EMVSA, utilized a coil to rapidly change the stiffness of a magnetic spring through current modulation. Through this design, multiple other effects were studied including the effectiveness of water cooling as well as shock absorption through eddy-current breaking. Both of these added features enable the spring to run for prolonged times and be a safer mechanism to operate near humans. On the other hand, AMVSA, presented a unique antagonistic configuration of magnetic spring to change the position and the stiffness of a robotic finger by mechani-



(a) Top view (b) Side view

Figure 5.27: A single motor connected to three driving magnets through bevel gears

cally varying the magnetization direction of magnets. AMVSA's design exploits the negative stiffness of magnetic attraction to render fast explosive motions for grasping tasks.

CHAPTER 6

Conslusions and Future Work

As legged robot locomotion and manipulation advances the need for more capable mechanisms and actuators increases. This work has presented a review of robotic leg mechanisms for quadruped robots and introduced a new quadruped robot for shipboard operations. It also proposed a design methodology that decouples the design of the motor and gearbox. It also showed a new kinematic configuration that relocates the knee motor gearbox in a parallel configuration from the hip to the knee joint. This design was tested and evaluated and was shown to reduce the antagonism as well as motor losses during the stance phase of the robot. Relocating the gearbox has also been shown to increase the stiffness of the belt-gearbox gear-train which is very desirable when using proprioceptive actuators.

This research also presented a family of compliant actuators based on nonlinear magnetic compliance. The nonlinear compliance was extensively studied and was shown to be a reasonable middle ground between stiff and soft series elastic actuators. Through the designs and tests performed, the actuators were shown to improve the shock absorption capability of robotic grippers as well as enable accurate force tracking. Other effects were also studied such as varying the stiffness of an actuator through coils. Moreover, the effects of negative stiffness and eddy current damping were also employed to create fast explosive motions and effective damping effects respectively.

6.1 SORELL Platform

The presented design of SORELL's leg and the modeling of the actuator and gearboxes as separate entities opens the door for future optimization studies. For this study, the choice was made to move the whole gearbox to the knee; however, future work can include studies to optimize the distribution of the gearing (i.e. keep a gearing of 1:2 at the actuator and move a smaller gearbox to the knee).

Another interesting effect of the new configuration is that when back-driving the knee motor it happens pre-gearing. Back-driving the motor this way passes the nonlinearities of the gearbox and results in less wasted torque. This effect can be studied and quantified in future work.

As for the belt design, it is possible to study using a crossed belt instead of a straight parallel one. Even though, the design will be harder to assemble and manufacture, such a design will flip the output torque at the knee. This will flip the effect of the coupling in the parallel configuration and push into the cooperative region instead of antagonistic.

6.2 Magnetic SEA and VSA

The SEAs and VSAs presented in this study have proven to be reliable as stand-alone grippers. However, these mechanisms can be combined to create more configurations and designs. Each of the presented actuators had a primary feature of electromagnetism studied for use in compliant actuators. These effects include permanent magnet arrangement, electromagnetism, negative stiffness, and eddy current damping. Moving forward, the characterization of these actuators and their underlying benefits and disadvantages. Figs. 6.1 and 6.2 show the overall characteristics of each of the actuators their limiting factors as well as their proposed uses.

In the near future, these actuators will be adopted by legged robots at the RoMeLa lab to perform manipulation tasks. Further done the road, the research will focus on optimizing these actuators and developing a methodology to choose and combine them to satisfy robotic joint design requirements. It is possible to also miniaturize these actuators in order to increase their efficiency and create more coherent muscle arrays made of magnetic SEAs and VSAs.

Gripper	Type	Force Curve	Position Control	Stiffness Control	Energy Requirement	Weight	Used at
MSEA	Rotary	Fixed-symmetrical	Yes	No	+	+	Finger
PMSEA	Prismatic	Fixed-asymmetrical	Yes	No	+	++	Forearm
EMVSA	Prismatic	Varying	Yes	Yes	+++	+++	Forearm
AMVSA	Prismatic	Varying	Yes	Yes-or Coupled	+	++	Finger
Multiplexer	Prismatic	Varying	Yes	Coupled	++	+	Finger

Figure 6.1

Gripper	Cooling?	Force Range	Deflection Range	SORELL Application
MSEA	No	[-0.8Nm 0.8Nm]	[-26° 26°]	For small gripper modules, for limited space and lightweight. Pick and place and some intricate tasks.
PMSEA	No	[-100N 40N]	[-9mm 4mm]	For leg attached end-effectors, med impact tasks, cyclic motion (Hammering and Drilling).
EMVSA	Yes	[-80N 80N]	[-12.7mm 12.7mm]	Multipurpose gripper, high impacts, force and stiffness control. For multipurpose SORELL Leg attached gripper.
AMVSA	No	[-40N 40N]	[-14mm 14mm]	Fast grasp and release, locking mechanism to hold heavy objects. Can be used as separate module.
Multiplexer	Yes	-	-	For small gripper modules attachments, different shapes of objects. Fast shape adaptive and precision grasping.

Figure 6.2

References

[1] J. Hooks, M. S. Ahn, J. Yu, X. Zhang, T. Zhu, H. Chae, and D. Hong, "ALPHRED: A Multi-Modal Operations Quadruped Robot for Package Delivery Applications", *IEEE Robotics and Automation Letters*, vol. 5, no. 4, pp. 5409–5416, Oct. 2020.

[2] "Spot", https://www.bostondynamics.com/spot, 2022.

[3] G. Bledt, M. J. Powell, B. Katz, J. Di Carlo, P. M. Wensing, and S. Kim, "MIT Cheetah 3: Design and Control of a Robust, Dynamic Quadruped Robot", in *2018 IEEE/RSJ International Conference on Intelligent Robots and Systems (IROS)*, Madrid, Oct. 2018, pp. 2245–2252, IEEE.

[4] A. Fukuhara, M. Gunji, and Y. Masuda, "Comparative anatomy of quadruped robots and animals: a review", *Advanced Robotics*, vol. 36, no. 13, pp. 612–630, July 2022.

[5] "ANYbotics", www.anybotics.com/anymal-legged-robot/, 2023.

[6] P. M. Wensing, A. Wang, S. Seok, D. Otten, J. Lang, and S. Kim, "Proprioceptive Actuator Design in the MIT Cheetah: Impact Mitigation and High-Bandwidth Physical Interaction for Dynamic Legged Robots", *IEEE Transactions on Robotics*, vol. 33, no. 3, pp. 509–522, June 2017.

[7] J. Hooks and D. Hong, "Implementation of a Versatile 3D ZMP Trajectory Optimization Algorithm on a Multi-Modal Legged Robotic Platform", in *2018 IEEE/RSJ International Conference on Intelligent Robots and Systems (IROS)*, Madrid, Oct. 2018, pp. 3777–3782, IEEE.

[8] M. Raibert, K. Blankespoor, G. Nelson, and R. Playter, "BigDog, the rough-terrain quadruped robot", vol. 41, no. 2, pp. 10822–10825.

[9] C. Semini, V. Barasuol, J. Goldsmith, M. Frigerio, M. Focchi, Y. Gao, and D. G. Caldwell, "Design of the Hydraulically Actuated, Torque-Controlled Quadruped Robot HyQ2Max", *IEEE/ASME Transactions on Mechatronics*, vol. 22, no. 2, pp. 635–646, Apr. 2017.

[10] C. Lee and S. Oh, "Development, Analysis, and Control of Series Elastic Actuator-Driven Robot Leg", *Frontiers in Neurorobotics*, vol. 13, pp. 17, May 2019.

[11] M. Shinohara, A. Umemura, T. Haneyoshi, and Y. Saito, "Coordination control of bi-articular robotic arm by motor drive with planetary gear", in *The 2010 International Power Electronics Conference - ECCE ASIA -*, Sapporo, Japan, June 2010, pp. 2551–2556, IEEE.

[12] X. Zeng, S. Zhang, H. Zhang, X. Li, H. Zhou, and Y. Fu, "Leg trajectory planning for quadruped robots with high-speed trot gait", vol. 9, no. 7, pp. 1508.

[13] T. Zhu, *Design of a Highly Dynamic Humanoid Robot*, PhD thesis.

[14] H. Choi, S. Oh, and K. Kong, "Control of a robotic manipulator in the polar coordinate system using a biarticular actuation mechanism", *International Journal of Control, Automation and Systems*, vol. 14, no. 4, pp. 1095–1105, Aug. 2016.

[15] K. Koutsoukis and E. Papadopoulos, "On the effect of robotic leg design on energy efficiency", in *2021 IEEE International Conference on Robotics and Automation (ICRA)*. pp. 9905–9911, IEEE.

[16] S. Rezazadeh, A. Abate, R. L. Hatton, and J. W. Hurst, "Robot leg design: A constructive framework", vol. 6, pp. 54369–54387.

[17] A. Abate, J. W. Hurst, and R. L. Hatton, "Mechanical antagonism in legged robots", in *Robotics: Science and Systems XII*. Robotics: Science and Systems Foundation.

[18] D. Williams and O. Khatib, "The virtual linkage: a model for internal forces in multi-grasp manipulation", in *[1993] Proceedings IEEE International Conference on Robotics and Automation*. pp. 1025–1030, IEEE Comput. Soc. Press.

[19] J. Grieco, M. Prieto, M. Armada, and P. Gonzalez De Santos, "A six-legged climbing robot for high payloads", in *Proceedings of the 1998 IEEE International Conference on Control Applications (Cat. No.98CH36104)*. vol. 1, pp. 446–450, IEEE.

[20] L.-S. Chou and S.-M. Song, "Geometric work of manipulators and path planning based on minimum energy consumption", vol. 114, no. 3, pp. 414–421.

[21] R. Blickhan, "The spring-mass model for running and hopping", vol. 22, no. 11, pp. 1217–1227.

[22] O. Arslan, U. Saranli, and O. Morgul, "An approximate stance map of the spring mass hopper with gravity correction for nonsymmetric locomotions", in *2009 IEEE International Conference on Robotics and Automation*. pp. 2388–2393, IEEE.

[23] S. Rezazadeh, C. Hubicki, M. Jones, A. Peekema, J. Van Why, A. Abate, and J. Hurst, "Spring-mass walking with ATRIAS in 3d: Robust gait control spanning zero to 4.3 KPH on a heavily underactuated bipedal robot",

in *Volume 1: Adaptive and Intelligent Systems Control; Advances in Control Design Methods; Advances in Non-Linear and Optimal Control; Advances in Robotics; Advances in Wind Energy Systems; Aerospace Applications; Aerospace Power Optimization; Assistive Robotics; Automotive 2: Hybrid Electric Vehicles; Automotive 3: Internal Combustion Engines; Automotive Engine Control; Battery Management; Bio Engineering Applications; Biomed and Neural Systems; Connected Vehicles; Control of Robotic Systems*. p. V001T04A003, American Society of Mechanical Engineers.

[24] M. Hutter, C. D. Remy, M. A. Hopflinger, and R. Siegwart, "SLIP running with an articulated robotic leg", in *2010 IEEE/RSJ International Conference on Intelligent Robots and Systems*. pp. 4934–4939, IEEE.

[25] P. A. Bhounsule, J. Cortell, and A. Ruina, *DESIGN AND CONTROL OF RANGER: AN ENERGY-EFFICIENT, DYNAMIC WALKING ROBOT*, pp. 441–448, WORLD SCIENTIFIC.

[26] S. Seok, A. Wang, M. Y. Chuah, D. J. Hyun, J. Lee, D. M. Otten, J. H. Lang, and S. Kim, "Design principles for energy-efficient legged locomotion and implementation on the MIT cheetah robot", vol. 20, no. 3, pp. 1117–1129.

[27] P. Hebert, M. Bajracharya, J. Ma, N. Hudson, A. Aydemir, J. Reid, C. Bergh, J. Borders, M. Frost, M. Hagman, J. Leichty, P. Backes, B. Kennedy, P. Karplus, B. Satzinger, K. Byl, K. Shankar, and J. Burdick, "Mobile Manipulation and Mobility as Manipulation-Design and Algorithms of RoboSimian: Mobile Manipulation and Mobility as Manipulation-Design and Algorithms of RoboSimian", *Journal of Field Robotics*, vol. 32, no. 2, pp. 255–274, Mar. 2015.

[28] J. S. Mehling, P. Strawser, L. Bridgwater, W. K. Verdeyen, and R. Rovekamp, "Centaur: NASA's Mobile Humanoid Designed for Field Work", in *Proceedings 2007 IEEE International Conference on Robotics and Automation*, Rome, Italy, Apr. 2007, pp. 2928–2933, IEEE, ISSN: 1050-4729.

[29] M. Schwarz, T. Rodehutskors, D. Droeschel, M. Beul, M. Schreiber, N. Araslanov, I. Ivanov, C. Lenz, J. Razlaw, S. Schüller, D. Schwarz, A. Topalidou-Kyniazopoulou, and S. Behnke, "NimbRo Rescue: Solving Disaster-Response Tasks through Mobile Manipulation Robot Momaro", *Journal of Field Robotics*, vol. 34, no. 2, pp. 400–425, Mar. 2017, arXiv:1810.01345 [cs].

[30] T. Klamt, D. Rodriguez, M. Schwarz, C. Lenz, D. Pavlichenko, D. Droeschel, and S. Behnke, "Supervised Autonomous Locomotion and Manipulation for Disaster Response with a Centaur-Like Robot", in *2018 IEEE/RSJ International Conference on Intelligent Robots and Systems (IROS)*, Madrid, Oct. 2018, pp. 1–8, IEEE.

[31] I. Ha, Y. Tamura, H. Asama, J. Han, and D. W. Hong, "Development of open humanoid platform darwin-op", in *SICE Annual Conference 2011*, 2011, pp. 2178–2181.

[32] T. Zhu, J. Hooks, and D. Hong, "Design, Modeling, and Analysis of a Liquid Cooled Proprioceptive Actuator for Legged Robots", July 2019, pp. 36–43.

[33] X. Zhang, *Application of Proprioception Quasi-Direct Drive Actuators on Dynamic Robotic Systems*, PhD thesis, 2019.

[34] X. Zhang, T. Zhu, I. Yamayoshi, and D. Hong, "A force controlled under actuated robotic hand with mechanical intelligence and proprioceptive compliant actuation", in *2018 IEEE-RAS 18th International Conference on Humanoid Robots (Humanoids)*, 2018, pp. 1–8.

[35] R. V. Ham, T. G. Sugar, B. Vanderborght, K. W. Hollander, and D. Lefeber, "Compliant actuator designs", *IEEE Robotics Automation Magazine*, vol. 16, no. 3, pp. 81–94, 2009.

[36] G. A. Pratt and M. M. Williamson, "Series elastic actuators", in *Proceedings 1995 IEEE/RSJ International Conference on Intelligent Robots and Systems. Human Robot Interaction and Cooperative Robots*, 1995, vol. 1, pp. 399–406 vol.1.

[37] S. Wolf, G. Grioli, O. Eiberger, W. Friedl, M. Grebenstein, H. Höppner, E. Burdet, D. G. Caldwell, R. Carloni, M. G. Catalano, D. Lefeber, S. Stramigioli, N. Tsagarakis, M. Van Damme, R. Van Ham, B. Vanderborght, L. C. Visser, A. Bicchi, and A. Albu-Schäffer, "Variable stiffness actuators: Review on design and components", *IEEE/ASME Transactions on Mechatronics*, vol. 21, no. 5, pp. 2418–2430, 2016.

[38] D. W. Robinson, *Design and Analysis of Series Elasticity in Closed-loop Actuator Force Control*, PhD thesis, Dept. Mech. Eng., Massachusetts Institute of Technology, Cambridge, MA, USA, 2000.

[39] W. Roozing, J. Malzahn, N. Kashiri, D. G. Caldwell, and N. G. Tsagarakis, "On the stiffness selection for torque-controlled series-elastic actuators", *IEEE Robotics and Automation Letters*, vol. 2, no. 4, pp. 2255–2262, 2017.

[40] J. H. Yoon, D. Sun, V. Sanandan, and D. Hong, "Experimental Validation of Unlumped Model and its Design Implications for Rotary Series Elastic Actuators", in *International Design Engineering Technical Conferences and Computers and Information in Engineering Conference*, 08 2017, vol. 5A: 41st Mechanisms and Robotics Conference.

[41] V. Orekhov, *Series Elasticity in Linearly Actuated Humanoids*, PhD thesis, Virginia Polytechnic Institute and State University, Blacksburg, VA, Dec 2014.

[42] A. Schepelmann, K. Geberth, and H. Geyer, "Compact nonlinear springs with user defined torque-deflection profiles for series elastic actuators", in *Proceedings of (ICRA) International Conference on Robotics and Automation*. May 2014, pp. 3411 – 3416, IEEE.

[43] I. Thorson and D. Caldwell, "A nonlinear series elastic actuator for highly dynamic motions", in *2011 IEEE/RSJ International Conference on Intelligent Robots and Systems*, 2011, pp. 390–394.

[44] Y. Sun, P. Tang, J. Zheng, D. Dong, X. Chen, L. Bai, and W. Ge, "Optimal design of a nonlinear series elastic actuator for the prosthetic knee joint based on the conjugate cylindrical cam", *IEEE Access*, vol. 7, pp. 140846–140859, 2019.

[45] F. A. Rafeedi, J. H. Yoon, and D. Hong, "Design and control of a novel compact nonlinear rotary magnetic sea (msea) for practical robotic gripper implementation", *IEEE Robotics and Automation Letters*, vol. 6, no. 4, pp. 7643–7650, 2021.

[46] A. Sudano, N. L. Tagliamonte, D. Accoto, and E. Guglielmelli, "A resonant parallel elastic actuator for biorobotic applications", in *2014 IEEE/RSJ International Conference on Intelligent Robots and Systems*, 2014, pp. 2815–2820.

[47] A. Schepelmann, K. A. Geberth, and H. Geyer, "Compact nonlinear springs with user defined torque-deflection profiles for series elastic actuators", in *2014 IEEE International Conference on Robotics and Automation (ICRA)*, 2014, pp. 3411–3416.

[48] Zhiwei Zhang, A. Rodriguez, and M. T. Mason, "A novel nonlinear compliant link on simple grippers", in *2015 IEEE/RSJ International Conference on Intelligent Robots and Systems (IROS)*, 2015, pp. 2923–2928.

[49] E. Ohashi and K. Ohnishi, "Variable compliance control based on soft-landing trajectory for hopping robot", in *30th Annual Conference of IEEE Industrial Electronics Society, 2004. IECON 2004*. vol. 1, pp. 117–122, IEEE.

[50] C. Mitsantisuk, K. Ohishi, and S. Katsura, "Variable mechanical stiffness control based on human stiffness estimation", in *2011 IEEE International Conference on Mechatronics*. pp. 731–736, IEEE.

[51] S. S. Jujjavarapu, A. H. Memar, M. A. Karami, and E. T. Esfahani, "Variable Stiffness Mechanism for Suppressing Unintended Forces in Physical Human–Robot Interaction", *Journal of Mechanisms and Robotics*, vol. 11, no. 2, 02 2019, 020915.

[52] Junho Choi, S. Park, Woosub Lee, and Sung-Chul Kang, "Design of a robot joint with variable stiffness", in *2008 IEEE International Conference on Robotics and Automation*, 2008, pp. 1760–1765.

[53] M. Howard and S. Vijayakumar, "Exploiting variable stiffness in explosive movement tasks".

[54] B. Vanderborght, A. Albu-Schaeffer, A. Bicchi, E. Burdet, D. G. Caldwell, R. Carloni, M. Catalano, O. Eiberger, W. Friedl, G. Ganesh, M. Garabini, M. Grebenstein, G. Grioli, S. Haddadin, H. Hoppner, A. Jafari, M. Laffranchi, D. Lefeber, F. Petit, S. Stramigioli, N. Tsagarakis, M. Van Damme, R. Van Ham, L. C. Visser, and S. Wolf, "Variable impedance actuators: A review", *Robot. Auton. Syst.*, vol. 61, no. 12, pp. 1601–1614, Dec. 2013.

[55] M. Itik, M. Sabetghadam, and G. Alici, "Force control of a tri-layer conducting polymer actuator using optimized fuzzy logic control", vol. 23, no. 12, pp. 125024.

[56] R. Wache, D. N. McCarthy, S. Risse, and G. Kofod, "Rotary motion achieved by new torsional dielectric elastomer actuators design", vol. 20, no. 2, pp. 975–977.

[57] R. Chen, L. Wu, Y. Sun, J.-Q. Chen, and J.-L. Guo, "Variable stiffness soft pneumatic grippers augmented with active vacuum adhesion", *Smart Materials and Structures*, vol. 29, no. 10, pp. 105028, sep 2020.

[58] P. Beyl, M. Van Damme, R. Van Ham, B. Vanderborght, and D. Lefeber, "Pleated pneumatic artificial muscle-based actuator system as a torque source for compliant lower limb exoskeletons", vol. 19, no. 3, pp. 1046–1056.

[59] Y. Zhao, J. Yu, H. Wang, G. Chen, and X. Lai, "Design of an electromagnetic prismatic joint with variable stiffness", *Industrial Robot: An International Journal*, vol. 44, no. 2, pp. 222–230, Mar. 2017.

[60] F. Petit, M. Chalon, W. Friedl, M. Grebenstein, A. Albu-Schaffer, and G. Hirzinger, "Bidirectional antagonistic variable stiffness actuation: Analysis, design & implementation", in *2010 IEEE International Conference on Robotics and Automation*. pp. 4189–4196, IEEE.

[61] A. H. Memar, N. Mastronarde, and E. T. Esfahani, "Design of a novel variable stiffness gripper using permanent magnets", in *2017 IEEE International Conference on Robotics and Automation (ICRA)*, 2017, pp. 2818–2823.

[62] N. Govindan, S. Ramesh, and A. Thondiyath, "Design of a variable stiffness joint module to quickly change the stiffness and to reduce the power consumption", *IEEE Access*, vol. 8, pp. 138318–138330, 2020.

[63] C. A. Nelson, L. Nouaille, and G. Poisson, "Variable Stiffness Mechanism for Robotic Rehabilitation", in *Advances in Mechanism and Machine Science*, T. Uhl, Ed., Cham, 2019, pp. 1761–1769, Springer International Publishing.

[64] Z. Liu, H. Jin, H. Zhang, Y. Liu, Y. Long, X. Liu, and J. Zhao, "A variable stiffness actuator based on second-order lever mechanism and its manipulator integration", in *2021 IEEE International Conference on Robotics and Automation (ICRA)*, 2021, pp. 6999–7005.

[65] "Westwood Robotics", www.westwoodrobotics.io/, 2022.

[66] M. Haavisto and M. Paju, "Temperature stability and flux losses over time in sintered nd–fe–b permanent magnets", vol. 45, no. 12, pp. 5277–5280.

[67] "KJmagnetics", www.kjmagnetics.com/, 2022.

[68] I. H. Grinberg, A. Mangu, C. W. Peterson, E. Wilken-Resman, J. T. Bernhard, and G. Bahl, "Magnetostatic spring softening and stiffening in magneto-mechanical resonator systems", *IEEE Transactions on Magnetics*, vol. 55, no. 8, pp. 1–5, 2019.

[69] "EMS", www.emworks.com//, 2022.

[70] L. Zhou, W. Chen, W. Chen, S. Bai, J. Wang, and J. Zhang, "Design of a compact rotary series elastic actuator with nonlinear stiffness for lower limb exoskeletons*", in *2019 IEEE/ASME International Conference on Advanced Intelligent Mechatronics (AIM)*, 2019, pp. 68–73.

[71] P. Zhang, "7-system routines in industrial control", in *Industrial Control Technology*, P. Zhang, Ed., pp. 775–851. William Andrew Publishing, Norwich, NY, 2008.

[72] J. Austin, A. Schepelmann, and H. Geyer, "Control and evaluation of series elastic actuators with nonlinear rubber springs", in *2015 IEEE/RSJ International Conference on Intelligent Robots and Systems (IROS)*, 2015, pp. 6563–6568.

[73] J. Shamma and M. Athans, "Gain scheduling: potential hazards and possible remedies", *IEEE Control Systems Magazine*, vol. 12, no. 3, pp. 101–107, 1992.

[74] C. J. Bett, "9 - gain-scheduled controllers", in *The Electrical Engineering Handbook*, W.-K. CHEN, Ed., pp. 1107–1114. Academic Press, Burlington, 2005.

[75] E. Tamayo, C. Zuluaga, and H. Alvarez, "A fuzzy-evaluated gain scheduling approach for the pid control of a pressure plant", in *2019 IEEE 4th Colombian Conference on Automatic Control (CCAC)*, 2019, pp. 1–6.

[76] B. Okken, S. Stramigioli, and W. Roozing, "Progressive Series-Elastic Actuation with Magnet-based Non-linear Elastic Elements", in *2022 IEEE International Symposium on Safety, Security, and Rescue Robotics (SSRR)*, Sevilla, Spain, Nov. 2022, pp. 166–173, IEEE.

[77] D. Winter, "Biomechanical motor patterns in normal walking.", *Journal of motor behavior*, vol. 15 4, pp. 302–30, 1983.

[78] E. C. Martinez-Villalpando, L. Mooney, G. Elliott, and H. Herr, "Antagonistic active knee prosthesis. a metabolic cost of walking comparison with a variable-damping prosthetic knee", in *2011 Annual International Conference of the IEEE Engineering in Medicine and Biology Society*, 2011, pp. 8519–8522.

[79] E. Rouse, L. Mooney, and H. Herr, "Clutchable series-elastic actuator: Implications for prosthetic knee design", *The International Journal of Robotics Research*, vol. 33, pp. 1611–1625, 11 2014.

[80] N. Kidambi, R. L. Harne, and K.-W. Wang, "Modular and programmable material systems drawing from the architecture of skeletal muscle", *Phys. Rev. E*, vol. 98, pp. 043001, Oct 2018.

[81] N.-B. Girtan and R. Olaru, "Improving the Performance of a Vibration Electromagnetic Actuator Based on Active Magnetic Springs", in *2018 International Conference and Exposition on Electrical And Power Engineering (EPE)*, Iasi, Oct. 2018, pp. 284–289, IEEE.

[82] R. Olaru, A. Arcire, C. Petrescu, M. M. Mihai, and B. Gîrtan, "A novel vibration actuator based on active magnetic spring", *Sensors and Actuators A: Physical*, vol. 264, pp. 11–17, Sept. 2017.

[83] H. Pu, S. Yuan, Y. Peng, K. Meng, J. Zhao, R. Xie, Y. Huang, Y. Sun, Y. Yang, S. Xie, J. Luo, and X. Chen, "Multi-layer electromagnetic spring with tunable negative stiffness for semi-active vibration isolation", *Mechanical Systems and Signal Processing*, vol. 121, pp. 942–960, Apr. 2019.

[84] Y. Sun, K. Meng, S. Yuan, J. Zhao, R. Xie, Y. Yang, J. Luo, Y. Peng, S. Xie, and H. Pu, "Modeling Electromagnetic Force and Axial-Stiffness for an Electromagnetic Negative-Stiffness Spring Toward Vibration Isolation", *IEEE Transactions on Magnetics*, vol. 55, no. 3, pp. 1–10, Mar. 2019.

[85] B. Yan, Y. Luo, and X. Zhang, "Structural multimode vibration absorbing with electromagnetic shunt damping", vol. 22, no. 6, pp. 1604–1617.

[86] R. Olaru, C. Petrescu, and A. Arcire, "DESIGN OF A MAGNETIC SPRING FOR VARIABLE STIFFNESS ACTUATORS", p. 8.

[87] R. Ravaud, G. Lemarquand, and V. Lemarquand, "Force and stiffness of passive magnetic bearings using permanent magnets. part 1: Axial magnetization", vol. 45, no. 7, pp. 2996–3002.

[88] R. Ravaud, G. Lemarquand, and V. Lemarquand, "Force and stiffness of passive magnetic bearings using permanent magnets. part 2: Radial magnetization", vol. 45, no. 9, pp. 3334–3342.

[89] E. Furlani, "A formula for the levitation force between magnetic disks", vol. 29, no. 6, pp. 4165–4169.

[90] V. D. Amara, J. Malzahn, W. Roozing, and N. Tsagarakis, "Blending of series-parallel compliant actuation with field weakening control for explosive motion generation", *IEEE Robotics and Automation Letters*, vol. PP, pp. 1–1, 02 2021.

[91] B. Mrak, B. Lenaerts, W. Driesen, and W. Desmet, "Optimal magnetic spring for compliant actuation – validated torque density benchmark", *Actuators*, vol. 8, no. 1, pp. 18, Feb 2019.

[92] S. Marullo, S. Bartoccini, G. Salvietti, M. Z. Iqbal, and D. Prattichizzo, "The Mag-Gripper: A Soft-Rigid Gripper Augmented With an Electromagnet to Precisely Handle Clothes", *IEEE Robotics and Automation Letters*, vol. 5, no. 4, pp. 6591–6598, Oct. 2020.

[93] V. Skfivan, O. Sodomka, and F. Mach, "Magnetically Guided Soft Robotic Grippers", in *2019 2nd IEEE International Conference on Soft Robotics (RoboSoft)*, Seoul, Korea (South), Apr. 2019, pp. 126–130, IEEE.